

University of Calgary

PRISM: University of Calgary's Digital Repository

Graduate Studies

The Vault: Electronic Theses and Dissertations

2018-08-10

Navigation of UAV in Denied GNSS Environments Using Multi-Sensor Systems

Mostafa, Mostafa Mohamed Ahmed

Mostafa, M. M. A. (2018). Navigation of UAV in Denied GNSS Environments Using Multi-Sensor Systems (Unpublished doctoral thesis). University of Calgary, Calgary AB.

doi:10.11575/PRISM/32809

<http://hdl.handle.net/1880/107628>

doctoral thesis

University of Calgary graduate students retain copyright ownership and moral rights for their thesis. You may use this material in any way that is permitted by the Copyright Act or through licensing that has been assigned to the document. For uses that are not allowable under copyright legislation or licensing, you are required to seek permission.

Downloaded from PRISM: <https://prism.ucalgary.ca>

UNIVERSITY OF CALGARY

Navigation of UAV in Denied GNSS Environments Using Multi-Sensor Systems

by

Mostafa Mohamed Ahmed Mostafa

A THESIS

SUBMITTED TO THE FACULTY OF GRADUATE STUDIES

IN PARTIAL FULFILMENT OF THE REQUIREMENTS FOR THE

DEGREE OF DOCTOR OF PHILOSOPHY

GRADUATE PROGRAM IN GEOMATICS ENGINEERING

and

GRADUATE PROGRAM IN ELECTRICAL AND COMPUTER ENGINEERING

CALGARY, ALBERTA

AUGUST, 2018

© Mostafa Mohamed Ahmed Mostafa 2018

Abstract

There have been extensive market demands over the past 10 years for deploying small autonomous Unmanned Aerial Vehicles (UAVs) in enormous civil and military applications such as search and rescue, disaster management, firefighting, reconnaissance and border mentoring. While UAVs are performing their missions, they are typically relying on the onboard Global Navigation Satellite System (GNSS)/ Inertial Navigation System (INS) integrated navigation system for the positioning and localization purpose. During such missions, the GNSS signals could be prone to blockage, attenuation, multipath effect, jamming and spoofing. In such complicated scenarios, the navigation solution is acquired by the INS in standalone mode prior to the GNSS signals recovery. Consequently, the navigation solution will deteriorate rapidly because of the drift exhibited by the low-cost INS during GNSS signal outages. Therefore, the necessity for an accurate and reliable navigation system in such cluttered environments is essential to achieve their missions. A variety of sensors and techniques have been exploited in an attempt to provide a reliable navigation solution in GNSS-denied environments. Although these sensors have some strengths individually, they still suffer from some limitations. Monocular Visual Odometry (VO) has been proposed as a GNSS denied environment navigation system for UAVs since it has light weight, small size and low power consumption. This monocular VO suffer from the scale ambiguity if there is no other aiding sensor or prior information of the observed scene. Furthermore, it depends on a rigorous calibrated camera and system model which may change from one flight to another or even during the flight. Therefore, a novel monocular VO based on optical flow and regression tress is proposed which eliminates the need for a calibration phase and inherently models the interior camera parameters, its lever arm and boresight parameters since, the relationship between the actual optical flow vectors and the navigation states are implicitly modeled during the flight. In addition,

this monocular VO can resolve the scale ambiguity problem by implicitly modeling the scale on its trained regression model. Although this monocular VO has such capabilities and benefits, its 3D positioning accuracy is still affected by some factors such as the lack of the observed features, inconsistent matches, and the accumulated positioning drift errors. Hence, a smart hybrid vision aided inertial navigation system (VAINS) is proposed to correct both monocular VO and INS drift errors based on trained Gaussian Process Regression (GPR) against GNSS reference data.

Although a variety of VO based approaches have been proposed to enhance the navigation solution during the GNSS signal outage, their imagery measurements are affected by brightness, lighting conditions and featureless areas. In addition, their measurements are not immune against the environmental conditions such as rain, fog and dust which could affect their usage as a GNSS denied environment navigation system. In order to avoid such limitations, a lightweight Frequency Modulated Continuous Wave (FMCW) Radar Odometry (RO) aided navigation system is proposed as a GNSS denied environment navigation system for UAVs. This system is immune to these environmental changes and it has light weight, small size, and low power consumption which make it more appealing to be mounted on small UAVs.

Although the camera has some strengths and limitations, its incorporation with radar will enhance the performance and will provide a more reliable navigation solution. In addition, the scale ambiguity of the monocular VO is resolved by the estimated RO height. Furthermore, this integrated system is more robust against the environmental conditions since the radar is immune against these environmental changes.

Acknowledgements

First and foremost, I am very grateful to Allah who gave me the ability to accomplish this research work.

I wish to express my gratitude to my supervisor, Professor Naser El-Sheimy, who gave me the opportunity to achieve this dissertation at University of Calgary. I would have never achieved this work without his invaluable support and guidance. I was very pleased to work under his supervision and I have learned a lot from working with him. Thank you is not enough for what you did with me.

I would like also thank Professor Abu B. Sesay for his helpful suggestions during the research work.

Deepest gratitude is also to Dr. Adel Moussa for his support, proposed ideas, valuable discussions throughout the research work.

Special thanks to my colleagues in my research group, Mobile Mapping Sensor Systems (MMSS), for their wonderful friendship, support, and help during the experiments: Haytham Abdallah, Shady Zahran, Mohamed Osama, Mohamed Fawzey, and Naief.

This dissertation would have never been possible without my loving wife Menna. I owe you too much for your understanding during hard times of my research. You were always supporting me and thank you for always being at my side.

I wish to express my love and gratitude to my beloved parents, you were always praying for me.

Finally, I would like to thank my country, Egypt, for funding and supporting my research, specially the Egyptian Armed Forces, my sponsor, for their support. I also would like to thank my Supervisor Dr. Naser El-Sheimy for the additional funding from NSERC and Canada Research Chairs programs.

Dedication

To My Beloved Family

My Lovely Wife, My Daughters and My Son,

My Parents,

My Brother

My Sister

(Thank You So Much)

Table of Contents

Abstract	ii
Acknowledgements	iv
Dedication	v
Table of Contents	vi
List of Tables	ix
List of Figures and Illustrations	x
List of Symbols, Abbreviations and Nomenclature	xvii
List of Symbols, Abbreviations and Nomenclature	xix
 CHAPTER ONE: INTRODUCTION FOR AUTONOMOUS UAVS NAVIGATION	 1
1.1 Motivations	1
1.2 Problem Statement	2
1.2.1 Visual sensors	2
1.2.2 Radar sensors	3
1.3 Research Objectives	4
1.3.1 First Objective - Monocular VO Aided INS	5
1.3.2 Second Objective – INS Drift Error Modeling	5
1.3.3 Third Objective - Smart Visual Odometry	6
1.3.4 Fourth Objective - RO Aided Navigation	6
1.3.5 Fifth Objective - RO/VO/mag/barometer integrated navigation system	6
1.4 Chapters Overview	7
 CHAPTER TWO: GNSS-DENIED ENVIRONMENTS NAVIGATION SYSTEMS FOR UAVS	 8
2.1 Light Detection and Ranging (LiDARs) based approach	11
2.2 Radar beacons-based approach	11
2.3 Signal of Opportunity (SOP)-based approach	12
2.4 Radar Odometry	12
2.5 Visual Odometry	15
2.6 Machine learning aided INS approaches for GNSS-denied environments	23
 CHAPTER THREE: OPTICAL FLOW BASED APPROACH FOR VISION	 25
 AIDED INERTIAL NAVIGATION USING REGRESSION TREES	 25
3.1 Sensors Specifications	26
3.2 Overview of the proposed System	27
3.3 Optical Flow Estimator	28
3.4 Motion Model Generation	30
3.5 Monocular VO/INS Fusion using EKF	32

3.6 Experimental Results	34
3.7 Summary	43
CHAPTER FOUR: PREDICTION OF INERTIAL POSITIONING ERRORS BASED ON	
GAUSSIAN PROCESS FOR UAVS IN GNSS DENIED ENVIRONMENT	44
4.1 Training Session	45
4.2 Prediction Session	47
4.3 Experimental Results	48
4.3.1 First Artificial Outage	49
4.3.2 Second Artificial Outage	51
4.3.3 Third Artificial Outage	54
4.3.4 Forth Artificial Outage	56
4.4 Summary	59
CHAPTER FIVE: A SMART HYBRID VAINS APPROACH	
FOR UAVS IN GNSS DENIED ENVIRONMENT	60
5.1 Overview of the System Architecture	62
5.2 Modes of Operation and Data Fusion	63
5.2.1 First Phase	64
5.2.2 Second Phase	68
5.2.3 Third Phase	71
5.3 Experimental Results	72
5.3.1 First Artificial Outage	74
5.3.2 Second Artificial Outage	76
5.4 Summary	80
CHAPTER SIX: LIGHTWEIGHT FMCW RADAR ODOMETRY AIDED	
NAVIGATION FOR UAVS IN GNSS DENIED ENVIRONMENT	83
6.1 Overview of the Integrated Navigational System	84
6.1.1 Radar Data Acquisition	85
6.1.2 Targets Detection and Velocity Extraction	88
6.1.3 RO/INS/ Magnetometer/ Barometer Fusion Using EKF	91
6.1.3.1 Prediction Model	92
6.1.3.2 Sensors Measurements	92
6.1.3.3 Observation Model	93
6.2 Experimental Results	98
6.2.1 Hardware setup	99
6.2.2 Results	101

6.2.2.1 First Experiment	101
6.2.2.2 Second Experiment	106
6.3 Summary	111
CHAPTER SEVEN: UAVS NAVIGATION IN DENIED GNSS ENVIRONMENTS	113
USING AN INTEGRATED RADAR AND VISUAL ODOMETRY	113
7.1 Overview of the Integrated Navigational System.....	113
7.1.1 FMCW RO	114
7.1.1.1 Data Accusation.....	114
7.1.1.2 Targets Detection and Data Extraction.....	115
7.1.2 Enhanced Monocular VO	116
7.1.2.1 Monocular VO	117
7.1.2.2 Velocity Compensation.....	119
7.1.3 Data Fusion.....	122
7.2 Hardware setup	122
7.3 Results.....	124
7.3.1 First Experiment	125
7.3.2 Second Experiment.....	131
7.4 Summary	138
CHAPTER EIGHT: CONCLUSIONS, CONTRIBUTIONS, AND FUTURE WORK..	140
8.1 Research Contributions.....	140
8.2 Conclusions.....	144
8.3 Future Work.....	148
REFERENCES	150

List of Tables

Table 2-1: Comparison between different inertial sensor grads.	10
Table 3-1: Comparison between (RMS Errors) values for all the navigation states derived from (VAINS) and (INS) during the GNSS signal outage period.	38
Table 3-2: Comparison between (RMS Errors) values for all the navigation states derived from (VAINS) and (INS) during the GNSS signal outage period.	42
Table 4-1: Comparison between (RMS Errors) values for the position states that obtained from (INS) and (INS with GPR).	55
Table 5-1: Comparison between (RMS Errors) values for the position states that obtained from (INS) and (INS with GPR).	79
Table 6-1: Comparison between (RMS errors) values for the position states obtained from (INS), and (RO) aided navigation system with respect to the ground truth values.	104
Table 6-2: Comparison between (RMS errors) values for the position states obtained from (INS), and (RO) aided navigation system with respect to the ground truth values.	109
Table 7-1: Comparison between (RMS errors) values for the position states obtained from (INS), enhanced monocular VO aided navigation, and the integrated system aided navigation with respect to the ground truth values.	129
Table 7-2: Comparison between (RMS errors) values for the position states obtained from (INS), enhanced monocular VO aided navigation, and the integrated system aided navigation with respect to the ground truth values.	135

List of Figures and Illustrations

Figure 1-1: Examples of indoor search and rescue operations.	1
Figure 2-1: Accumulated INS positioning drift errors during GNSS outage period.	10
Figure 2-2: Categories of GNSS denied environment navigation techniques.	11
Figure 2-3: Classifications for different proposed VO based approaches.	16
Figure 2-4: UAV on-board visual slam system architecture.	20
Figure 2-5: optical flow sensor/INS/magnetometer integrated navigation system architecture..	21
Figure 2-6: Google Map aided UAV navigation System Structure.....	22
Figure 3-1: The UAV that used in the data collection (Warren 2014).	26
Figure 3-2: The flight trajectory (Warren 2014).....	27
Figure 3-3: Optical flow-based approach for vision aided inertial navigation.....	28
Figure 3-4: The optical flow vectors and the averaging process among 3X3 image blocks.	31
Figure 3-5: Estimated flight trajectory using INS/GNSS Integration without GNSS Outage.....	35
Figure 3-6: Estimated flight trajectory using INS/GNSS integration during 1-min GNSS outage.	36
Figure 3-7: Estimated flight trajectory using INS/GNSS/Vision	36
Figure 3-8: Comparison between (North) values	37
Figure 3-9: Comparison between (East) values	37
Figure 3-10: Comparison between (Height) values.....	37
Figure 3-11: Estimated flight trajectory using INS/GNSS Integration without GNSS Outage...	39
Figure 3-12: Estimated flight trajectory using INS/GNSS integration.....	40
Figure 3-13: Estimated flight trajectory using INS/GNSS/Vision.	40
Figure 3-14: Comparison between (North) values	41
Figure 3-15: Comparison between (East) values.....	41

Figure 3-16: Comparison between (Height) values.....	41
Figure 4-1: Gaussian Process based approach for inertial drift compensation during the training session.....	46
Figure 4-2: Gaussian Process based approach for inertial drift compensation during the prediction session.....	47
Figure 4-3: Three-outage periods along the UAV flight trajectory.	48
Figure 4-4: Time line for the outage periods.	49
Figure 4-5: Estimated flight trajectory using INS/GNSS Integration without GNSS outage, INS/GNSS Integration with GNSS outage and INS/GNSS Integration	49
Figure 4-6: Comparison between (North) values obtained from (INS) and (INS with GPR correction) during the GNSS outage period.....	50
Figure 4-7: Comparison between (East) values obtained from (INS) and (INS with GPR correction) during the GNSS outage period.....	50
Figure 4-8: Comparison between (Height) values obtained from (INS) and (INS with GPR correction) during the GNSS outage period.....	50
Figure 4-9: Estimated flight trajectory using INS/GNSS Integration without GNSS outage, INS/GNSS Integration with GNSS outage and INS/GNSS Integration	51
Figure 4-10: Comparison between (North) values obtained from (INS) and (INS with GPR correction) during the GNSS outage period.....	52
Figure 4-11: Comparison between (East) values obtained from (INS) and (INS with GPR correction) during the GNSS outage period.....	52
Figure 4-12: Comparison between (Height) values obtained from (INS) and (INS with GPR correction) during the GNSS outage period.....	52
Figure 4-13: Estimated flight trajectory using INS/GNSS Integration without GNSS outage, INS/GNSS Integration with GNSS outage and INS/GNSS Integration	53
Figure 4-14: Comparison between (North) values obtained from (INS) and (INS with GPR correction) during the GNSS outage period.....	54
Figure 4-15: Comparison between (East) values obtained from (INS) and (INS with GPR correction) during the GNSS outage period.....	54
Figure 4-16: Comparison between (Height) values obtained from (INS) and (INS with GPR correction) during the GNSS outage period.....	54

Figure 4-17: Estimated flight trajectory using INS/GNSS Integration without GNSS outage, INS/GNSS Integration with GNSS outage and INS/GNSS Integration	56
Figure 4-18: Comparison between (North) values obtained from (INS) and (INS with GPR correction) during the GNSS outage period.....	57
Figure 4-19: Comparison between (East) values obtained from (INS) and (INS with GPR correction) during the GNSS outage period.....	57
Figure 4-20: Comparison between (Height) values obtained from (INS) and (INS with GPR correction) during the GNSS outage period.....	57
Figure 5-1: Illustrates the Smart Hybrid VAINS during the first phase.	67
Figure 5-2: Illustrates the Smart Hybrid VAINS during the second phase.	69
Figure 5-3: Illustrates the Smart Hybrid VAINS during the third phase.....	70
Figure 5-4: Lack of the observed features problem.	71
Figure 5-5: Inconstant matches between two successive frames.....	71
Figure 5-6: Two-outage periods along the UAV flight trajectory.	72
Figure 5-7: Three- experiments that performed along each outage period (VO/INS integration – VO/ (INS with GPR correction) integration - Smart Hybrid VAINS).	72
Figure 5-8: Estimated 2 D flight trajectory using INS/GNSS integration without GNSS outage, VO/INS integration, (VO/INS with GPR correction) integration and Smart Hybrid VAINS during the GNSS outage period.....	73
Figure 5-9: Comparison between (North) values obtained from VO/INS integration, (VO/INS with GPR correction) integration and Smart Hybrid VAINS during the GNSS outage period...74	
Figure 5-10: Comparison between (East) values obtained from VO/INS integration, (VO/INS with GPR correction) integration and Smart Hybrid VAINS during the GNSS outage period...74	
Figure 5-11: Comparison between (Height) values obtained from VO/INS integration, (VO/INS with GPR correction) integration and Smart Hybrid VAINS during the GNSS outage period...75	
Figure 5-12: Estimated 2 D flight trajectory using INS/GNSS integration without GNSS outage, INS in standalone mode, VO/INS integration, (VO/INS with GPR correction) integration and Smart Hybrid VAINS during the GNSS outage period.	76
Figure 5-13: Comparison between (North) values obtained from VO/INS integration, (VO/INS with GPR correction) integration and Smart Hybrid VAINS during the GNSS outage period...76	

Figure 5-14: Comparison between (East) values obtained from VO/INS integration, (VO/INS with GPR correction) integration and Smart Hybrid VAINS during the GNSS outage period...77

Figure 5-15: Comparison between (Height) values obtained from VO/INS integration, (VO/INS with GPR correction) integration and Smart Hybrid VAINS during the GNSS outage period...77

Figure 6-1: RO aided navigation system block diagram. 84

Figure 6-2: Reflected ground signals in the RDM image. 86

Figure 6-3: CFAR detected targets in the RDM image. 87

Figure 6-4: Histogram for the whole RDM. 88

Figure 6-5: Binarized RDM image by utilizing the computed threshold. 89

Figure 6-6: Detected targets based on connected components approach. 90

Figure 6-7: Utilized FMCW radar (RF-beam). 98

Figure 6-8: Utilized BULLET-M module (Ubiquity). 99

Figure 6-9: Hardware setup configuration. 99

Figure 6-10: Attached radar to the SOLO quadcopter. 100

Figure 6-11: First flight trajectory. 100

Figure 6-12: Comparison between forward ground truth velocity in the body frame, which obtained from (GNSS/INS) integration, and estimated velocity from the RO. 101

Figure 6-13: A comparison between the estimated 2D flight trajectory outage segments from the GNSS/INS integration (ground truth segment), and RO aided navigation system. 102

Figure 6-14: A comparison between the estimated 2D flight trajectory outage segments from the GNSS/INS integration (ground truth segment), and RO aided navigation system. 102

Figure 6-15: The north and east errors, which obtained from the RO. 102

Figure 6-16: A comparison between the estimated 2D flight trajectory outage segments from the GNSS/INS integration (ground truth segment), and INS in standalone mode during 135 sec of GNSS signal outage. 103

Figure 6-17: The north and east errors which obtained from INS in standalone mode during the GNSS outage period.....	103
Figure 6-18: shows RMS 3D positioning errors for RO aided.....	105
Figure 6-19: Second flight trajectory.....	105
Figure 6-20: Comparison between forward ground truth velocity in the body frame, which ...	106
Figure 6-21: A comparison between the estimated 2D flight trajectory outage segments from the GNSS/INS integration (ground truth segment), and RO aided navigation system.....	107
Figure 6-22: A comparison between the estimated 2D flight trajectory outage segments from the GNSS/INS integration (ground truth segment), and RO aided navigation system.....	107
Figure 6-23: The north and east errors, which obtained from the	107
Figure 6-24: Acomparision between the estimated 2D flight trajectory outage segments from the GNSS/INS integration (ground truth segment), and INS in standalone mode during 120 sec of GNSS signal outage.....	108
Figure 6-25: The north and east errors which obtained from INS in standalone mode during the GNSS outage period.....	108
Figure 6-26: RMS 3D positioning errors for RO.....	110
Figure 7-1: Reflected ground signals in the RDM image.....	114
Figure 7-2: Radar detected targets.....	115
Figure 7-3: RO estimated height.....	117
Figure 7-4: The optical flow vectors and the averaging process among 3X3 image cells.....	118
Figure 7-5: Illustrates the proposed system architecture during the training session.....	119
Figure 7-6: Illustrates the proposed system architecture during the prediction session.....	120
Figure 7-7: Utilized UDOO X86 single board computer.....	122
Figure 7-8: Attached camera and radar to the SOLO quadcopter.....	122
Figure 7-9: Aerial image for the first flight with a wide field of view.....	123
Figure 7-10: Aerial image for the second flight with a medium field of view.....	123
Figure 7-11: First flight trajectory.....	124

Figure 7-12: Comparison between forward ground truth velocity in the body frame, which is obtained from (GNSS/INS) integration, estimated velocity from the RO,.....	125
Figure 7-13: A comparison between the estimated 2D flight trajectory outage segments from the GNSS/INS integration (ground truth segment), and the enhanced monocular VO aided navigation system for 30 sec.	126
Figure 7-14: A comparison between the estimated 2D flight trajectory outage segments from the GNSS/INS integration (ground truth segment), and the enhanced monocular VO aided navigation system for 113 sec.	126
Figure 7-15: A comparison between the estimated 2D flight trajectory outage segments from the GNSS/INS integration (ground truth segment), and the proposed integrated system aided navigation system for 30 sec.	127
Figure 7-16: A comparison between the estimated 2D flight trajectory outage segments from the GNSS/INS integration (ground truth segment), and the proposed integrated system aided navigation system for 113 sec.	127
Figure 7-17: The North and East errors, which is obtained from the proposed integrated system aided navigation system during the GNSS outage period.	127
Figure 7-18: A comparison between the estimated 2D flight trajectory outage segments from the GNSS/INS integration (ground truth segment), and INS in standalone mode during 30 sec of GNSS signal outage.....	128
Figure 7-19: The north and east errors which are obtained from the INS in standalone mode during the GNSS outage period	128
Figure 7-20: RMS 3D positioning errors for the proposed integrated system aided navigation system during different outage periods.....	130
Figure 7-21: Second flight trajectory.....	131
Figure 7-22: Comparison between forward ground truth velocity in the body frame, which is obtained from (GNSS/INS) integration, estimated velocity from the RO, the typical VO, and the enhanced VO.	131
Figure 7-23: A comparison between the estimated 2D flight trajectory outage segments from the GNSS/INS integration (ground truth segment), and the enhanced monocular VO aided navigation system for 60 sec.	133
Figure 7-24: A comparison between the estimated 2D flight trajectory outage segments from the GNSS/INS integration (ground truth segment), and the enhanced monocular VO aided navigation system for 240 sec.	133

Figure 7-25: A comparison between the estimated 2D flight trajectory outage segments from the GNSS/INS integration (ground truth segment), and the proposed integrated system aided navigation system for 60 sec.	133
Figure 7-26: A comparison between the estimated 2D flight trajectory outage segments from the GNSS/INS integration (ground truth segment), and the proposed integrated system aided navigation system for 240 sec.	133
Figure 7-27: The North and East errors, which is obtained from the proposed integrated system aided navigation system during the GNSS outage period.	134
Figure 7-28: A comparison between the estimated 2D flight trajectory outage segments from the GNSS/INS integration (ground truth segment), and INS in standalone mode during 60 sec of GNSS signal outage.....	134
Figure 7-29: The North and East errors which are obtained from the INS in standalone mode during the GNSS outage period	134
Figure 7-30: RMS 3D positioning errors for the proposed integrated system aided navigation system during different outage periods.....	136

List of Symbols, Abbreviations and Nomenclature

Abbreviation	Definition
CA	Cell Averaging
CFAR	Constant False Alarm Rate
CNN	Convolutional Neural Network
CUT	Cell-Under-Test
DEM	Digital Elevation Model
DNN	Delayed Neural Networks
FFT	Fast Fourier Transform
FMCW	Frequency Modulated Continuous Wave
GNN	Global Nearest Neighbor
GNSS	Global Navigation Satellite System
GOCA	Greatest-of Cell Averaging
GPR	Gaussian Process Regression
HOG	Histograms of Oriented Gradients
IMU	Inertial Measurement Unit
INS	Inertial Navigation System
KF	Kalman Filter
LiDARs	Light Detection and Ranging devices
MAV	Micro Air Vehicle
MEMS	Micro-Electro-Mechanical Systems
MSAC	M-estimator Sample Consensus
MTT	Multiple-Target Tracker
NSE	Normalized Squared Error
OS-CFAR	Ordered Statistics CFAR
PF	Particle Filter
RANSAC	Random Sample Consensus
RDM	Range-Doppler Map
RF	Radio Frequency
RMSE	Root Mean Square Error
RNN	Recurrent Neural Networks
RO	Radar Odometry
SAR	Synthetic Aperture Radar
SfM	Structure from Motion
SOCA	Smallest-of Cell Averaging
SOP	Signal of Opportunity
SLAM	Simultaneous Localization and Mapping

SURF	Speeded Up Robust Features
SVD	Singular Value Decomposition
SVM	Support Vector Machines
TOA	Time of Arrival
UAVs	Unmanned Aerial Vehicles
UWB-OFDM	Ultra-Wideband Orthogonal Frequency Division Multiplexed
VAINS	Vision Aided Inertial Navigation System
VBN	Vision-Based Navigation
VO	Visual Odometry

List of Symbols, Abbreviations and Nomenclature

b, d	Bias vector of the accelerometers and gyros
c	Threshold of the MSAC loss function
C_b^n	Rotation matrix between the body and navigation frame
C_b^s	Rotation matrix between the body and sensor frame
C_n^b	Rotation matrix between the navigation and body frame
c_{light}	Speed of light
d	The selected data by MSAC algorithm
Err	The error function between the selected data and the generated hypothesis for MSAC algorithm
E^{ned}	Attitude errors in skew symmetric
e	Error of MSAC
e_p	GNSS position measurement error
e_r	GNSS position measurement error
$e_{h_{baro}}$	Barometer height measurement error
$e_{\psi_{mag}}$	Magnetometer heading measurement error
e_v	Velocity measurement noise
e_v	Velocity measurement noise
e	Earth ellipsoid eccentricity
f_*	Test outputs values
f_0	Initial transmitted frequency
f_b	Beat frequency
f_{cam}	Camera's focal length
$f_{doppler}$	Doppler frequency
f	Training outputs values
F	State dynamic matrix
G	Noise coefficient matrix
h_{GNSS}	GNSS height measurements
\tilde{h}_{baro}	Barometer height measurement
H_{RO}	RO design matrix
H_{GNSS}	GNSS design matrix
H_{baro}	Barometer design matrix
H_{mag}	Magnetometer design matrix
H_k	Design matrix
K_f	Sweep rate

K_k	Kalman gain
$k(x, x_*)$	Covariance matrix evaluated at all pairs of training and test points
l	length scale
l_{GNSS}^b	Lever-arm between the GNSS antenna and the IMU in the body frame
l_{RO}^b	Lever arm between the RO and the IMU represented in the body frame
l_{VO}^b	Lever arm between the VO and the IMU represented in the body frame
$Loss$	loss function of the MSAC
$m(x)$	Mean function
M_x, M_y, M_z	Unit-vector measurements of magnetic north in body frame
P	Point on the space
P_k	State covariance matrix
p	Image point
$P_{e,GNSS}$	East position measurement from GNSS
$P_{n,GNSS}$	North position measurement from GNSS
\tilde{p}_{GNSS}^{ned}	Measured position by the GNSS in the navigation frame
\hat{p}_{GNSS}^{ned}	Estimated GNSS position
R_k	Measurements covariance matrix
R	Equatorial earth radius
r_i	Range between the radar antenna and each scatterer inside the beam width of the radar
r_{GNSS}^n	Positions of the GNSS antenna center navigation frame
r_{IMU}^n	Position of the inertial sensor in the navigation frame
s	Pixel size
s_a, s_g	Accelerometers and gyros scale factor
T	Frequency sweep time
\tilde{V}_{RO}^s	Acquired velocity from the RO represented in the sensor frame
\hat{V}_{RO}^s	Estimated RO forward velocity
$\tilde{V}_{visual\ odom}^s$	Acquired velocity measurement from the VO represented in the sensor frame
V_{IMU}^n	Velocity of the vehicle at the center of the IMU represented in the navigation frame

$V_{\text{visual odom}}^s$	predicted velocity component in the flight path direction from VO represented in the sensor frame
V_{RO}	Estimated velocity in the flight path direction from the RO
w	Denotes the input weights (hyper-parameters) for the GPR
ω_{nb}^b	Angular rate of the body frame with respect to the navigation frame
ω_x, ω_y	Gyro's measurements
x	Denotes an input vector for the GPR training session
y	Denotes the desired output for the GPR training session
x_{pix}	x pixel coordinate
y_{pix}	y pixel coordinate
z_{GNSS}	GNSS positioning update
z_{mag}	Magnetometer heading update
Φ_k	State transition matrix
δ_{mag}	Magnetic declination
δz_v	Sensor frame residual velocity error measurement
δV_{IMU}^n	Velocity error of the vehicle at the center of the IMU
$\delta r^n, \delta v^n, \varepsilon^n$	Position, velocity and attitude error vector of INS mechanization
δz_{VRO}	RO innovation sequence between the measurement updates and the estimated measurements
δz_{baro}	Barometer innovation sequence between the measurement updates and the estimated measurements
δz_{GNSS}	GNSS innovation sequence between the measurement updates and the estimated measurements
δz_{mag}	Magnetometer innovation sequence between the measurement updates and the estimated measurements
$\delta \omega_{ib}^b$	Angular rate measurement error
$\epsilon_n, \epsilon_e, \epsilon_d$	Attitude errors in North–East–Down directions
\emptyset	Angle errors
Φ, θ	Roll and pitch angles
φ	Latitude
$\Delta V_{\text{prdicted Tree}}$	Predicted velocity increment
Δf	Frequency shift
Δt	Round trip propagation time delay
$\Delta V_{\text{prdicted Tree}}$	Predicted velocity increment from regression trees
$\Delta u, \Delta v$	Image plane displacement
$\Delta X, \Delta Y$	Real word displacement

Chapter One: Introduction for Autonomous UAVs Navigation

1.1 Motivations

Over the past few years, autonomous UAVs have been extensively deployed in a variety of civil and military applications. UAVs play a key role in different civil applications such as monitoring of territory, surveying infrastructures (roads, power lines, and pipelines), mapping, search and rescue, disaster assessment and management, firefighting, and downtown traffic management. In addition, they have been utilized in many military missions such as border mentoring, reconnaissance, and communication behind the enemy line.



(a) (pictures-and-images.com, 27/6/2018)



(b) (gizmodo.com, 27/6/2018)



(c) (DronesGlobe.com, 27/6/2018)



(d) (csl.illinois.edu, 27/6/2018)

Figure 1-1: Examples of various UAVs applications.

Deployment of UAVs on numerous aspects of our daily life can be a great help in terms of saving human lives and time. In order to meet the needs of these applications, an accurate and reliable navigation solution is required. In majority of current autonomous navigation systems, the typical onboard sensors installation for most of the commercial UAVs rely on fusing both GNSS and INS measurements using Kalman Filter (KF) for positioning and localization purpose.

1.2 Problem Statement

While UAVs performing their missions in challenging and cluttered environments, the GNSS signals might be lost or suffer from attenuation, multipath effect, jamming and spoofing. During the GNSS signals outage period, the vehicle navigation states are obtained by the INS in standalone mode until GNSS signals are retrieved. However, the navigation solution will deteriorate due to the drift exhibited by the INS solution even during periods of GNSS signal outages. Therefore, employment of another aiding sensor has a vital role in mitigating the accumulated drift errors associated with INS measurements while losing the GNSS signals. A variety of sensors and approaches attempt to provide navigation solution in GNSS-denied environments. Barometer and magnetometers measure the variation of the surrounding environment conditions. Alternately, another group of sensors such as radar [1], [2], radio beacons [3], [4], laser rangefinders [5], and cameras [6] provide range, heading and imagery measurements, respectively.

1.2.1 Visual sensors

Cameras can provide rich information in terms of color and texture, and they are, in general, small size, light weight and low power consumption that make them more convenient for small UAVs. Furthermore, cameras can assist in pose estimation, 3D environment reconstruction, and obstacle avoidance. A variety of monocular and stereo VO based on photogrammetric, and Structure from Motion (SfM) approaches have been proposed to assist the navigation process. The accuracy of

3D positioning using these techniques is still affected by some factors such as the lack of the observed features, the change of the camera calibration parameters, short base line, the scale problem in case of utilizing monocular VO, and the GNSS outage duration. On the other hand, machine learning based approaches considered to be as an alternative approach to these approaches which rely on the camera calibration parameters and the rigorous geometric model. Machine learning techniques consist of training and prediction sessions. The training algorithm attempts to learn the transformation function that directly maps the input information to the output and create a non-parametric model. During the prediction stage, the algorithm attempts to predict the output that can be obtained from a new input information by using the non-parametric model that has been obtained during the training stage.

The main problem of utilizing machine learning approach is that it depends mainly on the learning data set to optimize the hyperparameters values and to achieve a reliable performance during the prediction session. Therefore, if these hyperparameters are optimized by utilizing previously collected dataset rather than the current flight which may differ in the utilized sensors specifications, maneuvering scenarios, different platform, environmental changes, the predicted states may have poor accuracy. Therefore, the development of a reliable navigation system which can handle such challenges even during periods of GNSS signal outage is necessary.

1.2.2 Radar sensors

Radar based vehicle dynamic estimation has been explored as mean for aiding the navigation task. The inaccuracies of radar aided navigation solution based on Doppler measurements have been addressed in [7]. During the last decade, the large size, heavy weight, high power consumption, and expensive cost form significant issues for radars and restrict their usage for the navigation

filed particularly for small UAVs. Nowadays, due to the advancement of manufacturing technologies, a new sophisticated generation of radars are introduced that have light weight, small size and low power consumption which make them more appealing to be mounted on small UAVs. Unlike visual sensors which are affected by the environmental changes and featureless areas, these radars are immune to environmental changes such as illumination, rain, fog and dust [8] and they are not affected by the featureless areas. Although these radars have many benefits over other sensors, the target detection and velocity extraction from the cluttered and noisy measurements form a serious issue to obtain a reliable navigation solution.

1.3 Research Objectives

As mentioned earlier, flying in GNSS denied environment requires a reliable navigation solution. Therefore, the main objective of this thesis is to Develop and assessing a GNSS denied environment navigation system for UAVs which is capable of handling all the aforementioned challenges and reducing their effects. In addition, it is capable of reducing the low cost accumulated IMU drift errors during different GNSS outages periods through different steps to finally achieve a positioning accuracy similar to the single point GNSS accuracy which is 5 meters. This dissertation seeks to explore a visual and radar odometry approaches for the navigation of GNSS denied environments. As noted in section 1.2.1, there are some deficiencies in monocular VO are still not adequately addressed such as the scale ambiguity, and the change of the camera and system calibration parameters from one flight to another or even during the same flight for the conventional photogrammetric, SfM, and optical flow monocular VO based approaches. On the other hand, the proposed monocular VO based on machine learning approaches such as Gaussian process, Supported Vector Machine, and deep learning are pretrained before the real flight which may affect its estimated accuracy. In addition, such approaches are not capable of handling the

situations of missing inputs due to the lack of the observed features. RO has a great advantage over the visual sensors since it is not affected by the environmental conditions nor the featureless area. The main challenges for the RO are the target detection and velocity extraction from the cluttered and noisy measurements to provide an accurate navigation solution. Therefore, the thesis will include several sub-objectives that will serve the major objective. The subobjectives will focus on the development and assessment of four main algorithms and a part of them will be integrated to form the final navigation system.

1.3.1 First Objective - Monocular VO Aided INS

Developing a monocular VO algorithm with the capability of a) mitigating the INS drift errors during GNSS signal outages, b) assessing the ability to model the vehicle motion based on machine learning algorithm and the optical flow, c) find the most correlated features to be utilized during the training process, , d) eliminating the need for a calibration phase and inherently models of the interior camera parameters, its lever arm and boresight parameters by modeling the relationship between the optical flow and the vehicle forward velocity , e) exploring the effectiveness to train in online fashion during the flight to capture the behaviour of the most recent available data, and f) finding an appropriate approach to handle the situation of missing optical flow vectors in some image parts due to texture problems such as lack of features or rejected inconsistent matches caused by repeated patterns.

1.3.2 Second Objective – INS Drift Error Modeling

Developing a machine learning approach with the capability of, a) improving the positioning reliability and accuracy of the INS when the GNSS signal is blocked for short time, b) Assessing the ability to model the INS main trend drift errors (due to biases errors) when the GNSS signal is

available and predicting these errors during the GNSS signal outage. c) Assessing the ability to enhance the navigation solution based on a trained algorithm with a small data in online fashion.

1.3.3 Third Objective - Smart Visual Odometry

Enhancing the performance of the monocular VO aided navigation system which is affected by some factors such as the lack of the observed features, incorrect matches, and the sensor bias error (i.e. Camera and Inertial Measurements Unit (IMU)) by developing of a reliable navigation system that is capable of a) handling such challenges by molding the main trend drift errors for the camera and the INS based on a machine learning algorithm when the GNSS signals are available and to correct theses errors during the GNSS outages periods, b) providing the precession of the predicted errors to decide when these corrections could be applied and when discarded.

1.3.4 Fourth Objective - RO Aided Navigation

Developing RO, magnetometer, barometer, and INS integrated system in an Extended Kalman Filter (EKF) to a) enhance the 3D positioning accuracy during the GNSS signal outage b) avoid the camera limitation factors since the radar is immune against the illumination and environmental conditions, c) accurately detect and estimate the vehicle forward velocity from the cluttered measurements based on an efficient target detection approach, d). asses the ability of utilizing a small radar as GNSS denied environment navigation system for small UAV.

1.3.5 Fifth Objective - RO/VO/mag/barometer integrated navigation system

Developing a multi sensors system to a) mitigate the INS drift errors during GNSS signals outages. b) resolve the monocular VO scale ambiguity based on the RO height measurements c) handle the limitations for each of the radar and the camera individually since the radar measurements could be affected while flying over non-flat terrain, d) compensate the monocular VO drift errors based on a machine learning algorithm, e) Asses this integrated system over flat and non-flat terrain.

1.4 Chapters Overview

The thesis proposes the design and implementation of GNSS denied environment navigation system for UAVs which is capable of mitigating the effects of the navigation drifts exhibited by the INS during the GNSS signals outage.

The problem statement and the proposed solutions are addressed in the subsequent chapters. In addition, each chapter contains its experimental results to demonstrate the effectiveness of the proposed system.

- **Chapter 1** introduces the significance of deploying autonomous UAVs in enormous civil and military applications. Furthermore, the associated problems, challenges, research objectives and contributions have been addressed.
- **Chapter 2** highlights the related research works background which are focusing on different GNSS denied environment navigation systems for UAVs.
- **Chapter 3** introduces the proposed monocular VO algorithm based on optical flow and machine learning to aid the inertial navigation during GNSS signal outage (first objective). The experimental results and the summary are presented at the end of this chapter.
- **Chapter 4** purposes a GPR based approach to aid the inertial navigation during GNSS outage periods (second objective). The results are illustrated at the end of this chapter.
- **Chapter 5** presents A Smart Hybrid VAINS-based approach (third objective) to enhance the positioning accuracy and reliability of the proposed monocular VO (chapter 3) during GNSS outage periods. The experimental results also presented in this chapter.
- **Chapter 6** presents a novel FMCW RO (fourth objective) based approach for enhancing the 3D positioning accuracy of UAVs in GNSS denied environments. The proposed framework fuses the estimated velocity which is obtained from the RO with the

magnetometer, and barometer with the INS in an EKF. The experimental results are demonstrated for this integrated system.

- **Chapter 7** presents a novel RO and VO integrated system aided navigation (fifth objective) for enhancing the 3D positioning accuracy of UAVs in GNSS denied environments. The monocular VO is enhanced with the regression trees-based approach in an attempt to compensate for its associated drift errors. The estimated height from the RO is employed to resolve the monocular VO scale ambiguity's. The proposed framework fuses the estimated velocities which are obtained from the RO and enhanced monocular VO, magnetometer, and barometer with the INS in an EKF. The experimental results are demonstrated for this integrated system.
- **Chapter 8** concludes the proposed thesis by highlighting the challenges, contributions, achievement, and the suggested future work.

Chapter Two: GNSS-Denied Environments Navigation Systems for UAVs

Navigation in GNSS-denied environment forms a serious challenge for UAVs while performing their missions. The accumulated drift errors exhibited by the low-cost MEMS IMU in standalone mode during the GNSS signal outage force the solution to deteriorate rapidly during a short period of time. IMUs are one of the Inertial sensors family that work isolated from the surrounding environment and seek to estimate the vehicle dynamics. The main benefits of such IMUs that they can operate day, night, and on different environmental conditions. Some high degree of precision IMUs like those used in ballistic missiles allow them to navigate for a long distance with a high positioning accuracy. The main limitations of those IMUs that they have a large weight, size, power consumption, and cost which make them not applicable for the small commercial UAVs. Most of the commercial UAVs rely on MEMS IMUs that fit on them. Although these MEMS IMUs can help to provide a continuous navigation solution on harsh GNSS environments, a poor accuracy for the estimated navigation solution can be obtained from them since the inertial sensor's gyroscope and accelerometer outputs drift during a short period of time. Figure 2.1 shows the accumulated INS positioning drift errors over time during the GNSS signals outage period in the absence of any update source. This positioning drift error which is derived from the accelerometer and gyroscope biases can be computed as

$$\delta p = \frac{1}{2}b_f t^2 + \frac{1}{6}g b_\omega t^3 \quad (2-1)$$

Where δp is the IMU positioning drift error, b_f is the accelerometer bias, g is the acceleration gravity of the earth, b_ω is the gyro bias, and t is the time.

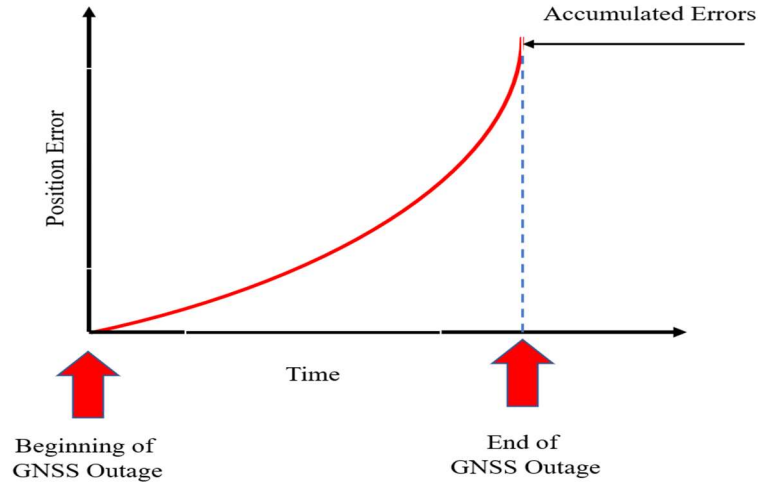


Figure 2-1: Accumulated INS positioning drift errors during GNSS outage period.

Inertial sensors have two main categories based on their accuracy [6]. The first category includes the tactical and navigational grades while the second one includes the low-cost MEMS sensors and consumer grade. The first category can provide an accurate navigation solution for long time of GNSS signals outage while the second one has a noisy measurements and drift on its output. Table 2.1 shows a comparison for the expected performance of different inertial grades [7].

Table 2.1: Comparison between different inertial sensor grades.

Category	Application Grade	Gyro Performance	Accelerometer Performance
Low Accuracy	Consumer (MEMS)	$>1 \text{ deg/s}$	$>50 \text{ mg}$
	Tactical	$\sim 1 \text{ deg/h}$	$\sim 1 \text{ mg}$
High Accuracy	Navigation	0.01 deg/h	$25 \text{ }\mu\text{g}$

From Table 2.1, it is clear that the estimated navigation solution from the low-cost MEMS IMUs will deteriorate dramatically during a short period of GNSS signals outage. Therefore, a variety of

multi sensors and techniques have been exploited in an attempt to provide a reliable navigation solution in GNSS-denied environments. These techniques can be classified in to active and passive techniques. Radar Odometry, Light Detection and Ranging, radar beacons, and Signal of Opportunity based approaches are considered to be active techniques while the Visual Odometry and the machine learning aided INS approaches are considered to be passive techniques. Figure 2.2 shows the classifications for different proposed GNSS-denied environments navigation techniques for UAVs.

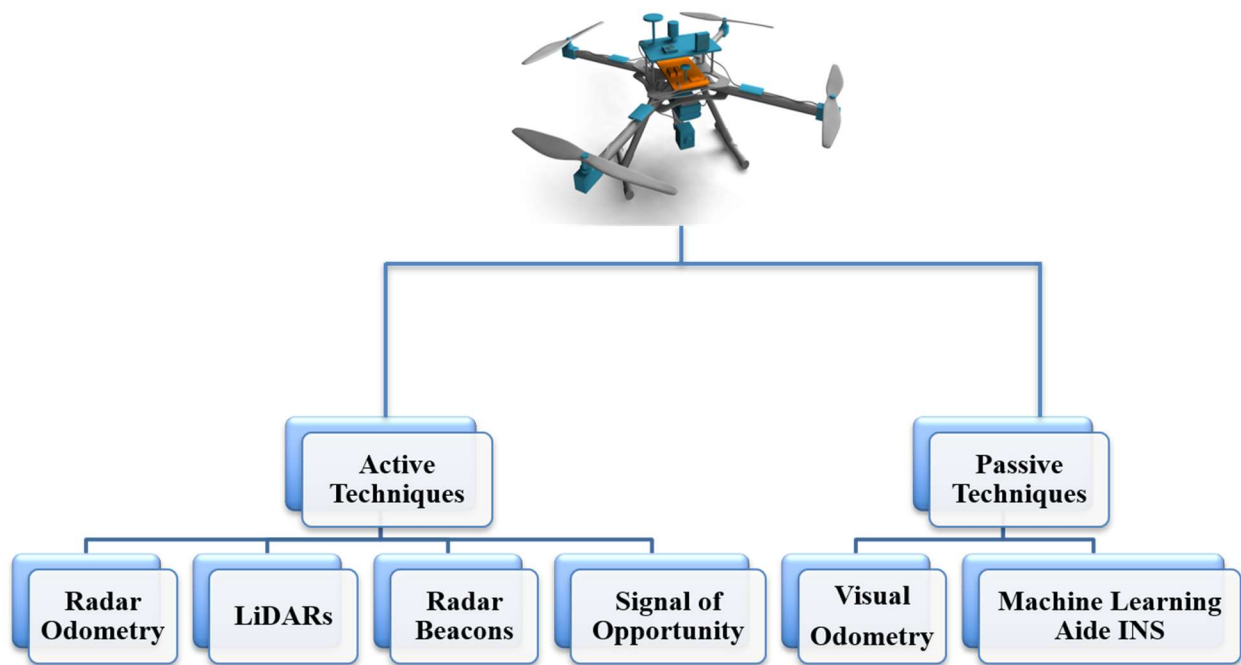


Figure 2-2: Categories of GNSS denied environment navigation techniques.

2.1 Light Detection and Ranging (LiDARs) based approach

LiDARs have been utilized in some GNSS-denied environments navigation systems for UAVs, see for example [8] and [9]. Typically, LiDARs are utilized in these GNSS-denied environments systems to generate a Digital Elevation Model (DEM) and match it to previously stored ones. The

crucial issues of utilizing such LiDARs are their heavy weight, large size and high-power consumptions, which make them inconvenient for micro and small UAVs. Moreover, the laser beam measurements are affected by some environmental factors such as rain and fog.

2.2 Radar beacons-based approach

Radar beacons are one of the main sources for navigation solutions that can be used in GNSS-denied environments. These beacons, when have well-known positions, act as landmarks across the navigation environment [10]. The beacons operation theory is analogous to the GNSS. Although these beacons can provide a very accurate navigation solution, the difficulties of installing them over a large territory restrict their usage as a GNSS-denied environments solution.

2.3 Signal of Opportunity (SOP)-based approach

Other sources of navigation solutions include SOP based approach which exploits any obtainable signals such as AM radios [11], Wi-Fi signals [12], digital and analog television signals [13], [14], and cell phone signals [15] to estimate the navigation solution. SOP depends mainly on developing a map for a certain area based on the received signals strength. This RF fingerprint mapping process is performed during the availability of the GNSS signals. This map is then used for the localization purpose during the GNSS signals outage. The main limitation of utilizing such an approach is that, the navigation solution cannot be acquired in an area that has not been mapped before. On the other hand, conventional multi-lateration method [16] could be used to navigate in GNSS-denied environments. Knowledge of the signals source positions, signal time of arrival (TOA), or signal direction of arrival is essential for this approach. One significant drawback of this

method is the need to pre-survey the transmitters' position, which is not available in different regions because they are not prepared for navigation tasks.

2.4 Radar Odometry

In the last decades, radar-based vehicle dynamic estimation (RO) has been explored as a mean for aiding the navigation task. A new generation of sophisticated radars which have the characteristics of light weight, small size and low power consumption have been developed in the last few years. Such specifications make those radars more convenient to be mounted on small UAVs for localization and mobile mapping applications. Furthermore, these radars are not affected by environmental changes such as rain, fog and dust.

Kauffman et al. in [17] presented a simulation for aerial navigation system in GNSS-denied environment based on ultra-wideband orthogonal frequency division multiplexed (UWB-OFDM) radar measurements. Targets detection is achieved by the M/N detector algorithm while the Global Nearest Neighbor (GNN) tracker is utilized for the tracking purpose [18]. The radar range measurement is combined with the INS in an EKF to obtain the navigation solution.

Quist and Beard presented an RO aided inertial navigation system for small unmanned aircraft in GNSS denied environment in [19]. A side-looking Synthetic Aperture Radar (SAR) is mounted on a fixed wing UAV to detect the ground targets. Target detection is achieved based on a pre-filtered image in conjunction with a Hough transform [20] to identify the hyperbolic targets from a range-compressed image. Then, the detected targets are utilized to extract the along-track and cross-track velocity over time, based on these detected targets. In addition, the first range bin in the range-compressed image is treated as the height above the ground. The estimated velocities and height

are fused with the INS measurements in an EKF. The proposed approach has been evaluated through a simulated data and some constraints are imposed to the flight scenario such as straight flight, constant velocity, leveled flight, and flying over flat terrain.

Quist et al. developed the previous work in [19] by flying in a more generic trajectory in a GNSS-denied environment [21]. The velocity, height, heading angle from magnetometer and estimated turn rate are utilized as measurement updates to the EKF. The proposed scheme performance has been assessed in non-straight simulated flight trajectories with various banking angles. In addition, This RO is tested in a real flight through a GNSS-denied environment for 60 secs, by fixing SAR on Cessna aircraft. A costly navigation-grade IMU is employed during this flight to provide more accurate navigation solution. On the other hand, biases and white noise are added for the IMU measurements to mimic the consumer-grade performance, which is typically equipped to the small UAVs.

Quist and Beard presented an alternative approach for the RO aided navigation for GNSS-denied environment based on the range progression from the ground targets [22]. A Recursive- Random Sample Consensus (RANSAC) algorithm has been developed for target detection, tracking, and range rate estimation. The altitude above the ground, heading from digital compass, pseudo turn rate, range to the scatterers' measurements and relative range are fused with the navigation grade IMU in an EKF to provide the navigation solution. The proposed algorithm is evaluated in real flight data set with SAR mounted on Cessna aircraft.

Scannapieco et al. presented a RO scheme for small and micro UAVs in cluttered environments [23]. The utilized radar is capable of measuring the magnitude, range, and azimuth for ground echoes. The Constant False Alarm Rate (CFAR) filter [24] is utilized for the target detection

purpose. The multiple-target tracker (MTT) based on the GNN algorithm is then applied to the detected targets to track them between successive epochs. The vehicle relative translation and rotation are then acquired from the tracked objects by the applying Singular Value Decomposition (SVD) algorithm [25].

The first ground echo is then projected by tilting angle to the vertical direction to be the height above the ground. Loosely and tightly coupled techniques are utilized to fuse RO with the INS measurements via an EKF. The former approach relays on estimating the pose variation and heading angle from the RO to update the EKF while the last approach directly utilize track range and bearing as measurements update. Two flights are conducted in various places with different radar configurations to assess the proposed system performance. During the first flight, the radar is installed in a forward-looking configuration. The second test flight is performed over different objects such as poles, wired nets, cars, and the radar is pitched by (20°) degrees. Since the proposed RO is based on the SVD algorithm, it cannot differentiate between rotation and translation especially when the vehicle rotates without any translation or with small movement.

2.5 Visual Odometry

In the last few decades, vision sensors have been used in many applications to achieve different tasks such as, camera pose estimation, 3D reconstruction of the surrounding environment, and obstacle avoidance. VO can assist to achieve these different missions through three main steps that form the basis of most VO approaches: feature detection, matching, and camera pose update. This architecture is used for example in [26], [27], and [28].

The VO based approaches can be categorized into two main categories which are VO based on closed form solutions and VO based on machine learning approaches. Figure 2.3 shows the detailed classifications for different proposed VO based approaches.

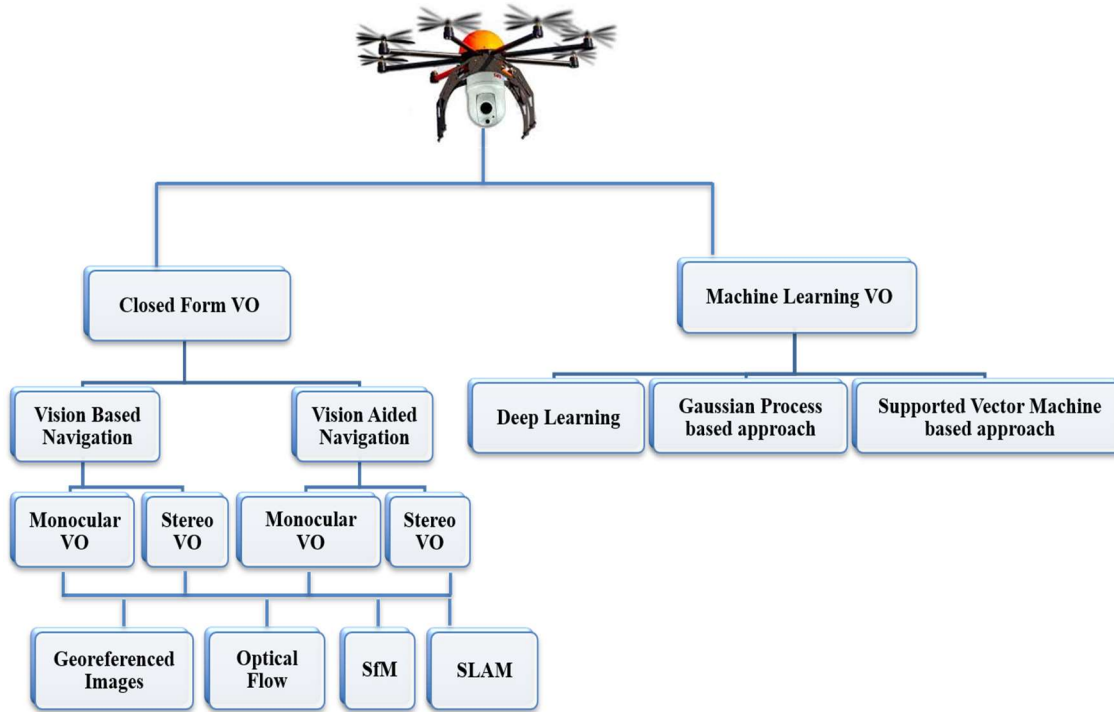


Figure 2-3: Classifications for different proposed VO based approaches.

In many cases, VO is integrated with IMU [29], [30], [31], [32] and it is so-called Vision Aided INS (VAINS). Alternatively, many other sensor configurations rely on using vision alone as a pose estimator [33], [34], [35] and it is so-called Vision-Based Navigation (VBN). Both VAINS and VBN can be classified into two main approaches (1) monocular VO and (2) stereo VO. monocular VO has received considerable attention due to the use of single camera which does not require base station and low cost [36], [37], [38], [39], [40], [41], [42] which make it more convenient for many different applications such as, robotic devices [43]. Monocular VO can be implemented by

using a variety of photogrammetric and computer vision approaches. The two major implemented types of monocular VO are, SfM approach that generates and refines structure at every time step [44], [45], [46], and a fundamental matrix approach which computes the relative translation and orientation between successive frames without constructing the 3D point clouds [47]. Although monocular VO techniques have some benefits, they still suffer from the scale ambiguity if no external aiding measurements or any a priori knowledge about the surrounding environment are available.

To disband this problem, stereo or multiple pair of a rigidly fixed cameras with overlapping views are utilized [48], [26], [49], [50]. The stereo VO solution accuracy typically depends on its lever arm and boresight parameters. Therefore, any small change in these parameters during the flight can affect the triangulation process accuracy as well as the estimated navigation solution. Moreover, the short base line between the fixed stereo pair limits the triangulation accuracy. So, the stereo VO is only used with UAVs flying at lower altitudes.

Alternatively, VO based on optical flow has been proposed in some research works to estimate the vehicle motion [51], [52]. In addition, it is employed for collision avoidance [53], [54], landing [55], and hovering [56]. Optical flow has been used to estimate the camera ego-motion. A variety of optical flow-based approaches are introduced such as [57] and [58], feature-based approach [58]. These optical flow algorithms rely on height sensor to resolve the correlation between the velocity and the height and to be able to estimate the velocity components.

Other VO are exploiting the geo-referenced imagery which are obtained from satellite or aerial images for positioning and localization purpose. The vehicle position is estimated by registering these geo-referenced imageries with the observed images from the onboard camera. Although this

approach has been utilized in UAVs navigation [59], and safe landing [60], [61], the environmental and illumination changes are considered a serious challenge for utilizing such approach.

Simultaneous Localization and Mapping (SLAM) based approach has been widely utilized to implement the VO by simultaneously estimating the vehicle pose and landmark positions [62], [63]. Multiple approaches to SLAM are exist. EKF-SLAM is considered to be one of the most popular implementation since it models noise as Gaussian and uses an EKF to estimate the map and vehicle state. FastSLAM uses a Rao-Blackwellised particle filter to handle the nonlinear process models [64]. GraphSLAM is similar to EKF-SLAM but capable of handling the large state models present in large maps more than the EKF-SLAM [65].

Alternatively, a limited amount of work base on machine learning techniques have been applied to monocular VO algorithms. Such approaches attempt to learn the relationship between image observations and cameras ego-motion, without requiring geometric camera models. A monocular VO based on GRR, and Support Vector Machines (SVM) regression algorithms have been proposed in [66], and [67] respectively. These approaches are utilizing the optical flow as inputs for the training session. Although these approaches are successfully capable of estimating the vehicle motion and resolving the scale ambiguity, their machine learning based approaches are not capable of handling missing optical flow vectors in some image parts due to, the lack of the observed features or, inconsistent matches caused by repeated patterns, which is forming a serious issue for estimating the navigation solution.

Deep learning approaches have been explored for localization purpose. The research work in [68] proposes VO based on Convolutional Neural Network (CNN) through synchrony detection between image sequences and features. The main limitation of this work is its treatment for the

pose estimation problem as a classification rather than regression. Another VO based on appearance “map” of the scene is introduced in [69]. A trained CNN model has been utilized to achieve this task. This network needs to be re-trained or at least fine-tuned while navigating in a new environment. This issue limits its usage and widespread as a generic solution in unknown environments. To tackle this problem, a dense optical flow-based approach is utilized to train CNN model rather than RGB images for motion estimation in [70]. A pre-processed dense optical flow is utilized as input for this network, which limits its incorporation for real time applications. This happens because such CNN network is not capable of modeling image sequences or videos for sequential learning.

To overcome this issue, a Recurrent Neural Networks (RNN) has been merged with the CNN in [71]. The RGB images for monocular camera, IMU acceleration, and angular velocity measurements are utilized as inputs. The 3-dimensional translation vector and 4-dimensional orientation quaternion are the outputs for this network. Although the proposed system has the ability of eliminating the need for manual calibration between the IMU and camera, and capable of performing end-to-end sequential learning, the network requires long time to be trained (6 hours). In addition, large amounts of data are required for the training purpose. Such requirements limit its usage if the vehicle platform parameters have been changed from the training time and also eliminate the ability to train this network online during the vehicle navigation.

A monocular visual SLAM algorithm has been proposed in [72] which is simultaneously estimating aircraft poses and scene structure. Figure 2-4 illustrates the structure of the system. First, the camera pose is initialized at the origin of the global reference frame, then the relative translation is estimated based on the computed essential matrix from matching five features

between two successive frames. This process is performed iteratively to obtain the camera poses and the 3D point cloud. A Sliding window bundle-adjustment is applied to enhance the solution accuracy. Finally, the camera poses are corrected by utilizing the loop closer algorithm to recognize the revisited areas. Although this system demonstrates its capability to SLAM, it still suffers from the scale ambiguity while utilizing a monocular camera. Additionally, the proposed algorithm results accuracy depends mainly on observing the revisited area which is not considered a typical situation for all flight missions.

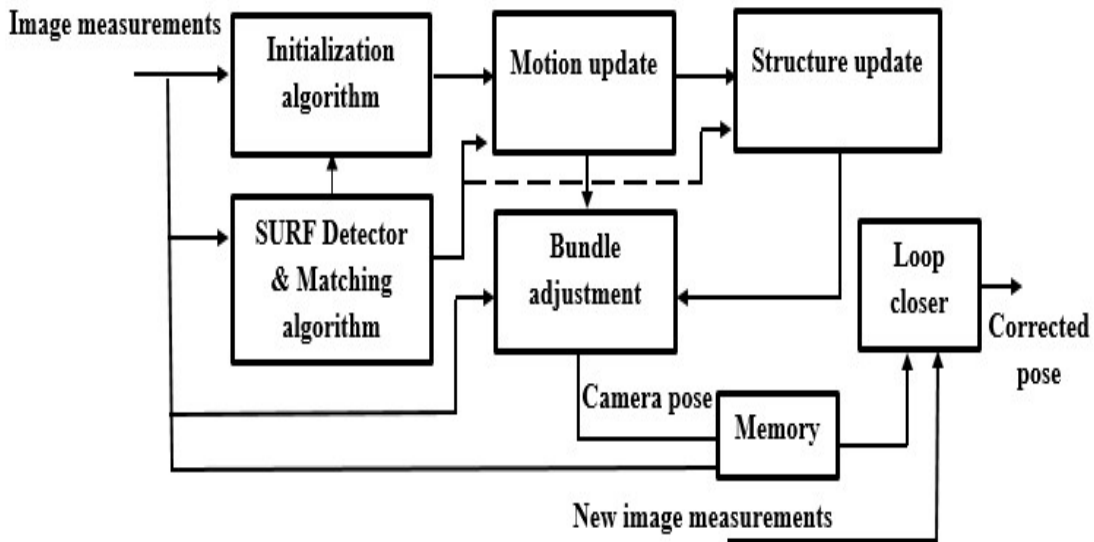


Figure 2-4: UAV on-board visual SLAM system architecture.

An optical flow sensor/INS/magnetometer integrated navigation system is presented in [73] for Micro Air Vehicle (MAV) as a GNSS denied environment navigation system. The data fusion is performed using an EKF to estimate the attitude, velocity, and position states. The system architecture is illustrated in Figure 2-5. The estimated optical flow parameters are obtained based on the block matching algorithm. An ultrasonic sensor is utilized for the height measurement which is fused with the optical flow, and accelerometer measurements to estimate the navigation solution.

The attitude can be obtained from gyroscope output signal. Drift would influence the gyroscope output. Therefore, the attitude information without drift can be obtained from the integrated accelerometer/ Magnetometer sensors during stationary or uniform motion state. The integrated accelerometer/ Magnetometer sensors then fused with the gyroscope output to limit this growing error. When the MAV is accelerating, the standalone gyroscopes are utilized for attitude estimation.

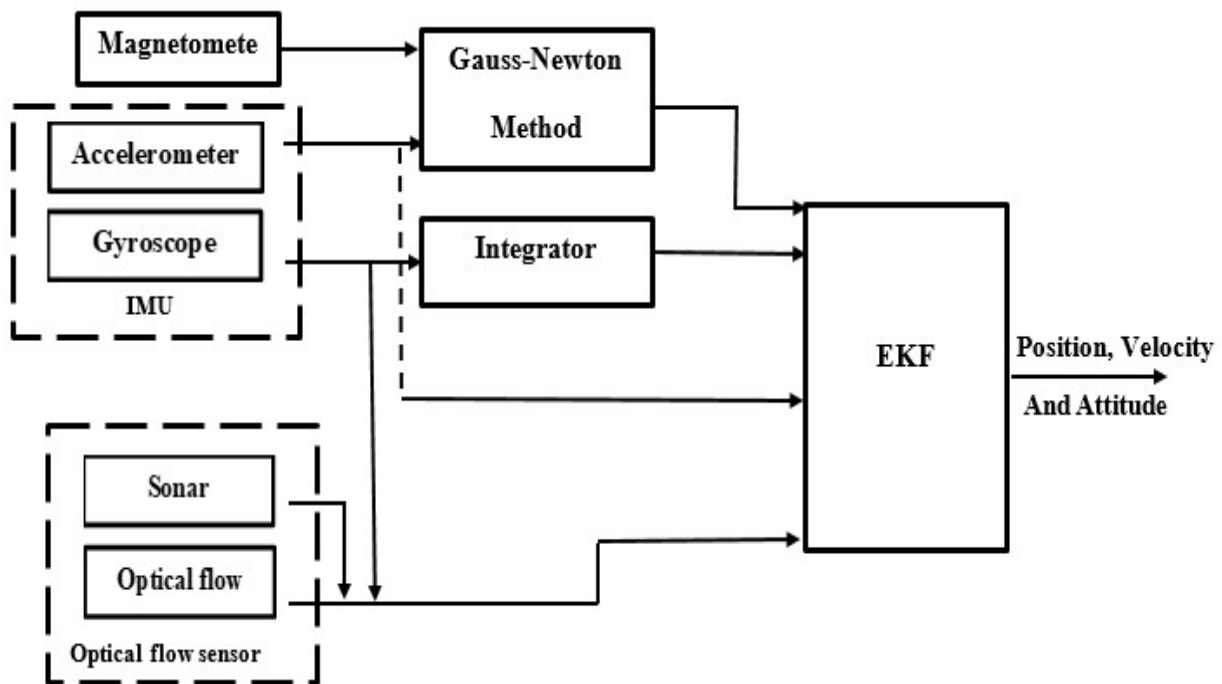


Figure 2-5: optical flow sensor/INS/magnetometer integrated navigation system architecture.

Although this system is capable of providing a GNSS denied environment navigation solution, the ultrasonic might fail to measure the height in case of a nonlinear motion such as sharp maneuvering.

Moreover, this system is depending on the projection of the earth's gravitational acceleration to estimate the attitude information of the vehicle only when the vehicle is static or in uniform motion. On the other hand, when the vehicle is accelerating this approach will not be valid anymore, and the attitude can be obtained from the gyro. The growing errors in the gyro measurements will affect the attitude estimation accuracy, and this proposed system will not be stable for a long time.

A Google Map aided UAV navigation in a GNSS-denied environment is presented in [74]. This system depends on registering the captured image which is obtained by the onboard camera to the stored Google map. The primary challenges of utilizing Google Map are the Variation in scale, orientation, and illumination in the observed scene from the stored Google images.

The proposed system depends on gradient patterns and uses Histograms of Oriented Gradients (HOG) for image registration to reduce the effect of this problem. The system architecture is illustrated in Figure 2-6.

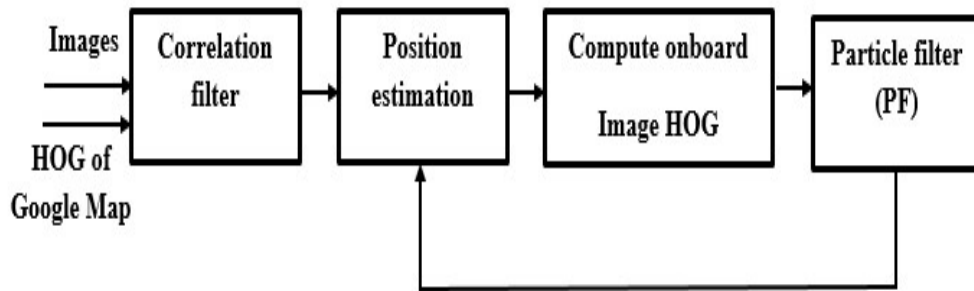


Figure 2-6: Google Map aided UAV navigation System Structure.

After taking off, the UAV location is searched in the entire map by computing the correlation between the currently captured image and the map. This process called the Global localization which initializes the location of the vehicle. After the initialization stage, the UAV position will be predicted based on Homography, and iterative Lucas-Kanade optical flow approach to narrow

down the search area on the map. The Particle Filter (PF) employed to provide the optimum searching area around the UAV location which is predicted by optical flow.

2.6 Machine learning aided INS approaches for GNSS-denied environments

Machine learning approaches can be used to predict the INS errors when the GNSS signal is lost. Then, these predicted errors are employed to compensate the INS mechanization output states to enhance the states accuracy and reliability. Different machine learning algorithms have been utilized to augment the INS during the GNSS signal outage such as neural networks, neuro-fuzzy, SVM and GPR. An auxiliary fuzzy-based model for predicting the KF positioning error states during GNSS signal outages was presented in [75]. To develop an appropriate underlying model, intensive data patterns have been collected that covered different vehicle dynamics and motion scenarios to use it through offline training. The difference between KF updated position errors, when GNSS is available, and KF predicted one's act as the desired model output during the training process.

The time elapsed since losing the GNSS signal, accelerometers measurements, gyroscopes measurements and the attitude angles were used as inputs during this stage. Although the test results indicate that the proposed algorithm capable of providing positioning corrections to the INS in standalone mode, it depends mainly on a large amount of offline training data to initialize the desired model.

Neuro-fuzzy-based data fusion module for real-time integration of INS and GNSS in vehicular navigation has been proposed in [76].

Results showed that the proposed module outperformed previous artificial intelligent-based data fusion modules with significantly low INS position errors during relatively long GNSS outages for both navigational and tactical grades INS.

An enhanced SVM based error model was proposed in [77]. The proposed algorithm was able to overcome other machine learning algorithms problems such as, local minimisation or over-fitting problems. The experimental results demonstrate that, the proposed SVM approach was able to reduce the noise standard deviation by 10–35% for gyroscopes and 61–76% for accelerometers. Moreover, the positional error drifts enhanced by 41% and 80% in comparison to Gauss Markov and neural networks approaches.

A Delayed Neural Networks (DNN) approach has been proposed in [78] to model both the INS position and velocity errors based on some past and current epochs of INS position and velocity states, respectively. The proposed algorithm was tested by using dataset that has been collected from different road trajectories by using both navigational and tactical grade INS which were mounted inside land vehicles and integrated with GNSS receivers. The results showed that, the proposed algorithm capable of enhancing the positioning accuracy especially for cases of tactical grade INS and long GNSS outages.

The GPR has been used to solve different applications problems. For example, the GPR has been trained in [79] to model the robot inverse dynamics. The GPR was used to adequately model the wireless propagation inside complex indoor environments in [80].

The GPR based approach was proposed in [81] to aid the INS during the GNSS signal outage for land vehicle. The corrected vehicle velocity and attitude that obtained from the INS output were used as inputs to the GPR during the training stage and the INS velocity and azimuth deviations

from the ground truth (GNSS measurements) were used as the desired outputs. When the GNSS signal is lost, the GPR model is used to predict the INS velocity and azimuth deviations. The predicted INS deviations are used as a virtual update to the KF. A large data set previously collected was used to optimize the hyper-parameters. The proposed technique showed an average position %RMSE reduction of 50% over a large number of experimental runs. The main objective of this paper is to provide a reliable and accurate navigation solution during a short period of GNSS signal outage. This goal is achieved through training a GPR algorithm for a short period in online fashion to correct the mechanization process (velocity and orientation) output states when the GNSS signal is lost.

Eventually, all the aforementioned background is provided through this chapter to cover a variety of the proposed GNSS denied environment navigation systems for UAVs. The proposed research work and achievements of this dissertation are illustrated in chapters 3, 4, 5 and 6.

Chapter Three: **Optical Flow Based Approach for Vision**

Aided Inertial Navigation Using Regression Trees

In this Chapter, an overview of the proposed system architecture is introduced. This discussion focusing on the proposed molecular VO methodology, and results. In addition, the utilized online dataset sensors components and their specifications are outlined. Typically, most of the proposed monocular VO techniques suffer from losing the scale if neither external measurement nor a priori knowledge about the surrounding environment are available. Moreover, these monocular VO algorithms rely on a calibrated camera model and apply the conventional photogrammetric and SfM approaches. While these approaches can help towards estimating the relative rotation and translation by tracking image features and applying geometrical constraints, they cannot estimate the motion scale using only the image visual features.

3.1 Sensors Specifications

An airborne dataset is used to test the proposed approach, this dataset is a gathered from fixed wing aircraft flown at Kagaru, Queensland, Australia on 31/08/10 (Warren et al. 2014) as shown in Figure 3-1.



Figure 3-1: The UAV that used in the data collection (Warren 2014 – [72]).

The test used the visual data from one of the two downward facing cameras. The system integrates an XSens Mti-g INS/GNSS to offer the navigation solution. A single point GPS is utilized for the positioning purpose. The dataset was collected over the rural area and includes views of grass, an air-strip, roads, trees, ponds, parked aircraft, and buildings as shown in Figure 3-2.



Figure 3-2: The flight trajectory (Warren 2014 – [72]).

A Pt Grey Flea2 firewire camera with a resolution of 1280x960, 6mm focal length lenses and 30 frames per second is employed in this dataset.

3.2 Overview of the proposed System

The proposed vision aided INS consists of 3 major blocks: (a) the optical flow estimator which extracts the optical vectors from the matched features between successive image frames, (b) the Artificial Intelligence (AI) which generates the relationship (underlying function) between image observations and vehicle motion during the GNSS signal availability, without requiring geometric camera models. ; this underlying function is used to predict the velocity component in the flight

path direction during the GNSS signal outage. Both of block (a) and (b) form the monocular VO and the (c) the AINS block which include the INS mechanization and EKF which integrate the predicted velocity from the monocular VO with the on-board INS measurements.

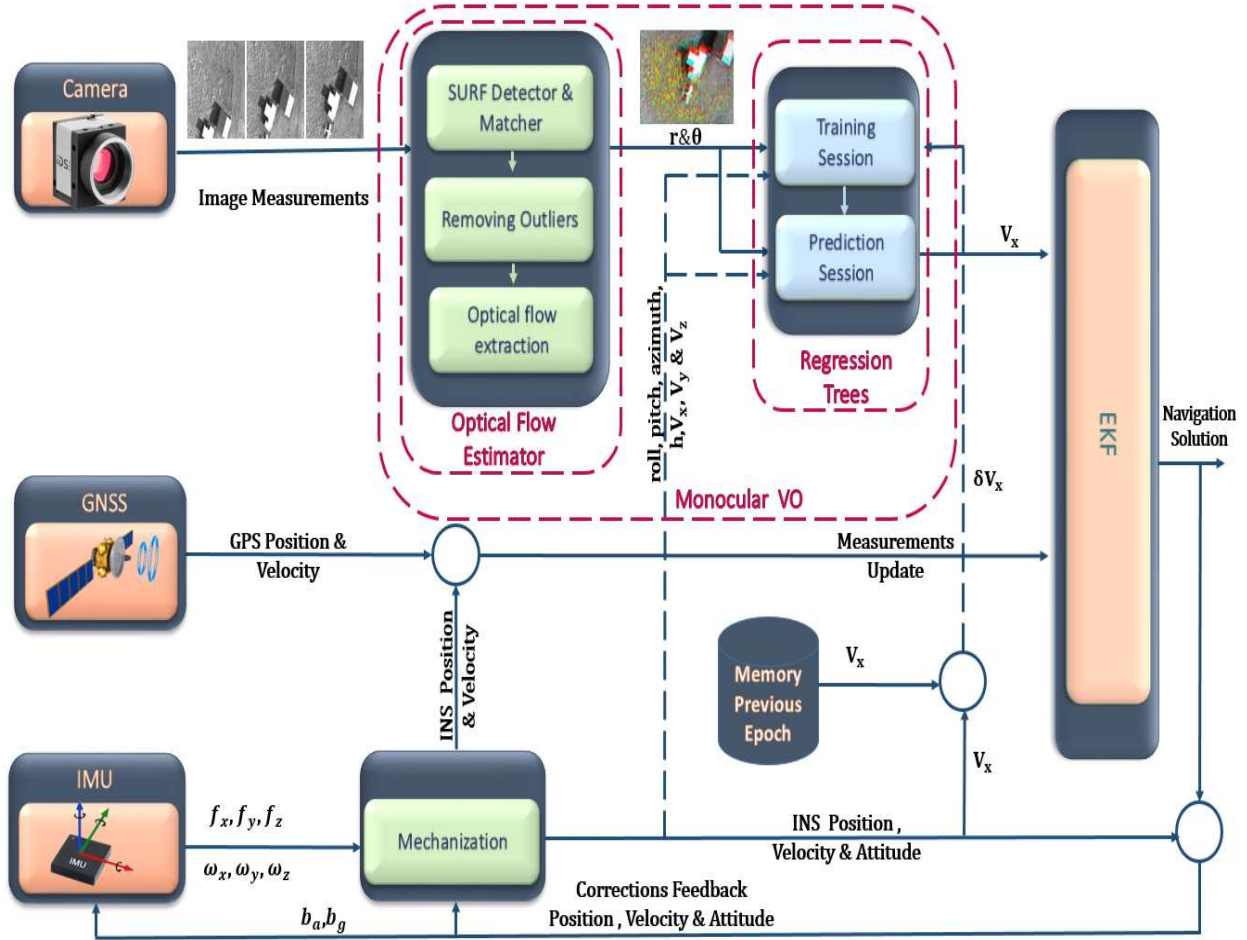


Figure 3-3: Optical flow-based approach for vision aided inertial navigation Using regression trees pipeline.

3.3 Optical Flow Estimator

The proposed algorithm (Optical Flow Estimator) detects the interest points of the image frames using Speeded Up Robust Features (SURF) approach [58].

The extracted points are then matched between the successive image frames. The matching process between two SURF points is achieved by calculating the Normalized Squared Error (NSE) between the descriptors of the two points. The main benefit of utilizing the SURF algorithm for optical flow estimation over other commonly utilized approaches such as horn schunck or lucas kanade is the reduction of the processing time since such approaches compute the optical flow for each pixel which is time consuming for the UAVs navigation task. In addition, such approaches assume that the displacement of the image contents between two nearby instants (frames) is small, and approximately constant within a neighborhood of the point p under consideration. When the flow vector may exceed this limit, the pyramid-based approach is utilized to down scale the image which is a time-consuming process. On the other hand, SURF is a rotation and scale invariant and it is not assuming a constant displacement like other approaches since the observed optical flow vectors have a different length of vectors. In addition, SURF descriptors are more efficient during the matching process than the horn schunck or lucas kanade. The matched points are assessed through M-estimator Sample Consensus (MSAC) step to avoid the outliers (incorrect matches) between matched points. The MSAC is considered as one of the members of RANSAC family. The MSAC is an iterative process of two steps, which are the hypothesis generation phase and hypothesis evaluation phase. During the first step, the MSAC picks up a subset of data randomly and estimates the model parameters from the sample. In the second stage, the datum is recognized as the inlier candidate, whose error from a hypothesis is within a predefined threshold. The MSAC solves the selection problem as an optimization problem. It is formulated as

$$\hat{M} = \arg \min \left\{ \sum_{d \in D} \text{Loss}(\text{Err}(d; M)) \right\} \quad (3-1)$$

where d is the matched features data, $Loss$ is a loss function, and Err is an error function between the selected data and the generated hypothesis. A loss function is used in evaluating a hypothesis for the RANSAC algorithm as follows:

$$Loss(e) = \begin{cases} 0 & |e| < c \\ \text{const} & \text{otherwise} \end{cases} \quad (3-2)$$

where c is the threshold and e represent the error. The loss function that represents the RANSAC algorithm in Equation2 was modified as a bounded loss function to use it in the MSAC algorithm as follows:

$$Loss(e) = \begin{cases} e^2 & |e| < c \\ c^2 & \text{otherwise} \end{cases} \quad (3-3)$$

The main benefit of utilizing this bounded loss function in the MSAC algorithm is that it will enhance the algorithm accuracy for removing the outliers and minimize the errors more than the RANSAC [82]. The optical flow vectors are obtained after removing the outliers from the matched points between two successive frames. Each image frame is divided into 3×3 cells as shown in Figure 3-4, and the extracted optical flow vectors are averaged along each cell. The main reason for this averaging process is to obtain the main trend of the optical flow vectors inside each cell and offer fixed number of vectors.

3.4 Motion Model Generation

When the GNSS signal is available, the roll, pitch, azimuth, height, velocity components estimated from the GNSS/INS integration and the optical flow vectors are used as inputs to the training block. The velocity change in the flight path direction between two successive frames is used as output during the learning process. The regression trees algorithm partitions the space of the

training data set into smaller regions to simplify the complexity and make the data more manageable. Then these regions partitioned again into sub-divisions. The recursive partitioning continues until obtaining chunks of the space that can fit a simple model between the training data input and the desired output. A 30 bag of trees are utilized during the training and the prediction session. The main benefit of utilizing this bag of trees that it is more immune to the noisy measurements than utilizing only one tree, since each tree is trained based on a different chunk of the training data set and the predicted output is obtained by averaging the whole trees which minimized its variance. A number of experiments are performed for selecting the number of bags of trees and 30 bags is founded to be the minimum number of bags which can provide an accurate prediction for the desired forward velocity without increasing the system complexity by increasing the number of bags.

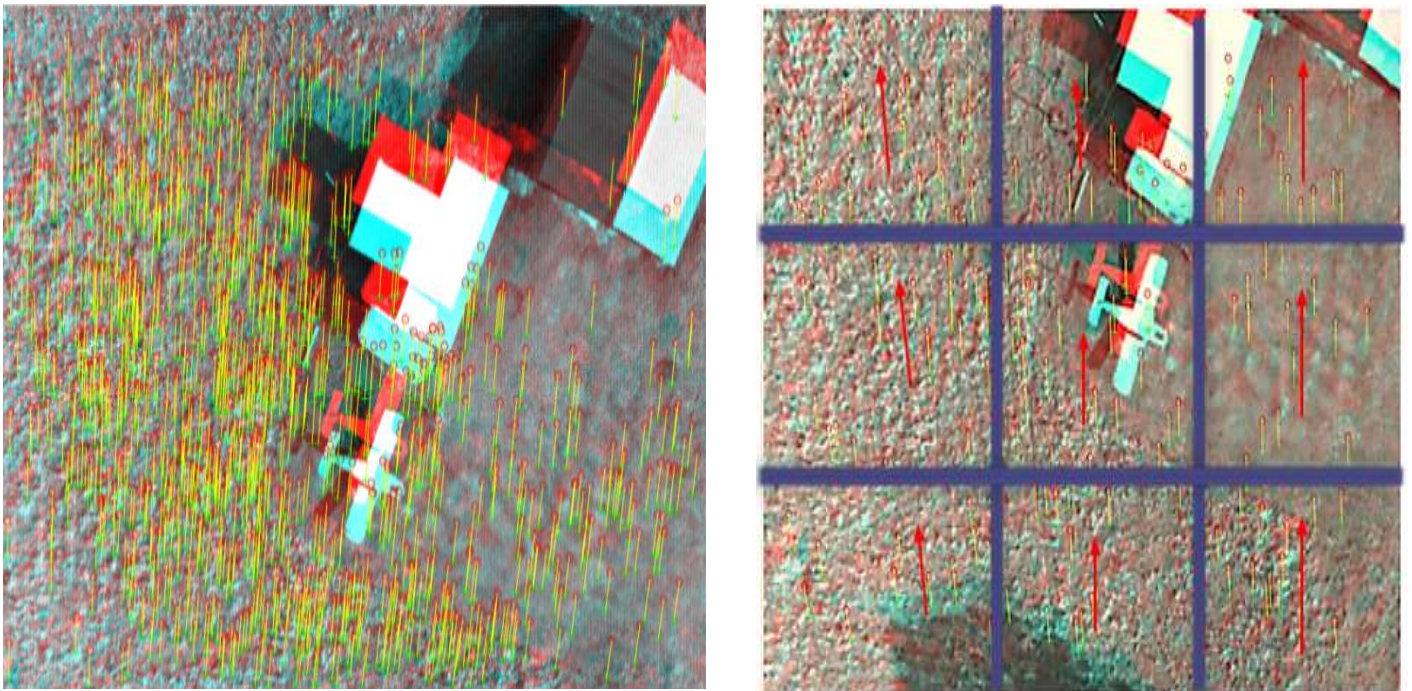


Figure 3-4: The optical flow vectors and the averaging process among 3X3 image blocks.

The proposed monocular visual odometer approach is able to predict the outputs even with the partial availability of inputs (optical flow vectors) thanks to the employed regression trees. This ability is of great help to handle the situations where the optical flow vectors are missing in some image parts due to texture problems such as lack of features or rejected inconsistent matches caused by repeated patterns. While the leaves of the sub tree we do reach are averaged to predict the value of the missing feature.

3.5 Monocular VO/INS Fusion using EKF

Once the GNSS measurements are unavailable, the prediction mode starts to predict the vehicle velocity component based on the extracted optical flow, the generated model during the training session and the last available measurements from the GNSS/INS integration.

This predicted velocity increment is added to the last available velocity observation that obtained from the GNSS/INS integration to obtain the velocity component in the current epoch as follows:

$$V_{\text{visual odom}} = V_{\text{last GNSS/INS}} + \Delta V_{\text{predicted Tree}} \quad (3-4)$$

This predicted velocity component in the flight path direction that has been obtained from the monocular VO ($V_{\text{visual odom}}$) is then optimally combined with data from the on-board INS in an EKF and can be expressed as

$$\tilde{V}_{\text{visual odom}}^s = V_{\text{visual odom}}^s + e_v \quad (3-5)$$

Where

$V_{\text{visual odom}}^s$ is the velocity obtained from the monocular VO represented in the sensor frame and e_v is the velocity measurement noise.

The lever arm conversion is necessary between the velocity of the vehicle at the center of the IMU and at the VO sensor before applying the updates. Moreover, it is necessary to consider any misalignment between the IMU frame and the VO frame (sensor frame). Therefore, the relationship between the V_{IMU}^n and $V_{visual\ odom}^s$ can be expressed as

$$V_{visual\ odom}^s = C_b^s C_n^b V_{IMU}^n + C_b^s (\omega_{nb}^b \times) l_{VO}^b \quad (3-6)$$

Where

V_{IMU}^n is the velocity of the vehicle at the center of the IMU represented in the navigation frame

ω_{nb}^b is the angular rate of the body frame, in which the velocity is measured by the VO, with respect to the navigation frame

l_{VO}^b is the lever arm between the VO and the IMU represented in the body frame

C_b^s is the rotation matrix between the body and sensor frame

C_n^b is the rotation matrix between the navigation and body frame

Referring Equation (3-3), the errors in coordinate transformation operation, which correspond to the attitude errors and the angular rate errors, were not considered. Therefore, this effect is incorporated into the computed sensor-frame velocity and can be expressed as

$$\begin{aligned} \hat{V}_{visual\ odom}^s &= C_b^s \hat{C}_n^b \hat{V}_{IMU}^n + C_b^s (\hat{\omega}_{nb}^b \times) l_{VO}^b \\ &\approx C_b^s C_n^b [I + (\phi \times)] (V_{IMU}^n + \delta V_{IMU}^n) + C_b^s (\omega_{nb}^b \times) l_{VO}^b + C_b^s (\delta \omega_{nb}^b \times) l_{VO}^b \\ &\approx V_{visual\ odom}^s + C_b^s C_n^b \delta V_{IMU}^n - C_b^s C_n^b (V_{IMU}^n \times) \phi - C_b^s (l_{VO}^b \times) \delta \omega_{nb}^b \end{aligned} \quad (3-7)$$

Where \emptyset is the angle error, δV_{IMU}^n is the velocity error of the vehicle at the center of the IMU and $\delta \omega_{ib}^b$ is the angular rate measurement error.

The sensor frame residual velocity error measurement equation can be computed as follows

$$\begin{aligned} \delta z_v &= \hat{V}_{visuual\ odom}^s - \tilde{V}_{visual\ odom}^s \\ &= C_b^s C_n^b \delta V_{IMU}^n - C_b^s C_n^b (V_{IMU}^n \times) \emptyset - C_b^s (l_{VO}^b \times) \delta \omega_{ib}^b - e_v \end{aligned} \quad (3-8)$$

From Equation (3-5) the design matrix can be expressed as

$$H_k = [0_{3 \times 3} : C_n^s : -C_n^s V_{IMU}^n : 0_{3 \times 3} : -C_b^s l_{VO}^b] \quad (3-9)$$

The estimated velocity measurement model can be calculated as follows

$$\begin{aligned} \delta \hat{z}_v &= H_k \hat{x}_k + \delta n_k \\ \delta \hat{z}_v &\approx [0_{3 \times 3} : C_n^s : -C_n^s V_{IMU}^n : 0_{3 \times 3} : -C_b^s l_{VO}^b] \begin{bmatrix} \delta r^n \\ \delta v^n \\ \varepsilon^n \\ b \\ d \end{bmatrix} \end{aligned} \quad (3-10)$$

3.6 Experimental Results

The proposed system has been evaluated through an airborne dataset. Two scenarios are performed during different trajectory segments by using the data gathered from a monocular camera to evaluate the effectiveness of the proposed algorithm in enhancing the 3D positioning accuracy during GNSS signal outages. The first scenario is performed after (3 min) from the UAV take-off for (1 min) of GNSS signal outage. Figure 3-5 shows the estimated flight trajectory obtained from the GNSS/INS integration without any GNSS signal outages. The green segment represents the location of the GNSS signal outage occurs. Figure 3-6 shows the estimated flight trajectory when

simulating one-minute GNSS signal outage. The green segment represents the INS performance in standalone mode during the outage period. The results show that the INS errors are growing and the position drift rapidly from the ground truth solution during this outage period. Figure 3-7 depicts the estimated flight trajectory by using the proposed VAINS. The standard division of the estimated forward velocity from the monocular VO is 0.15 m/s.

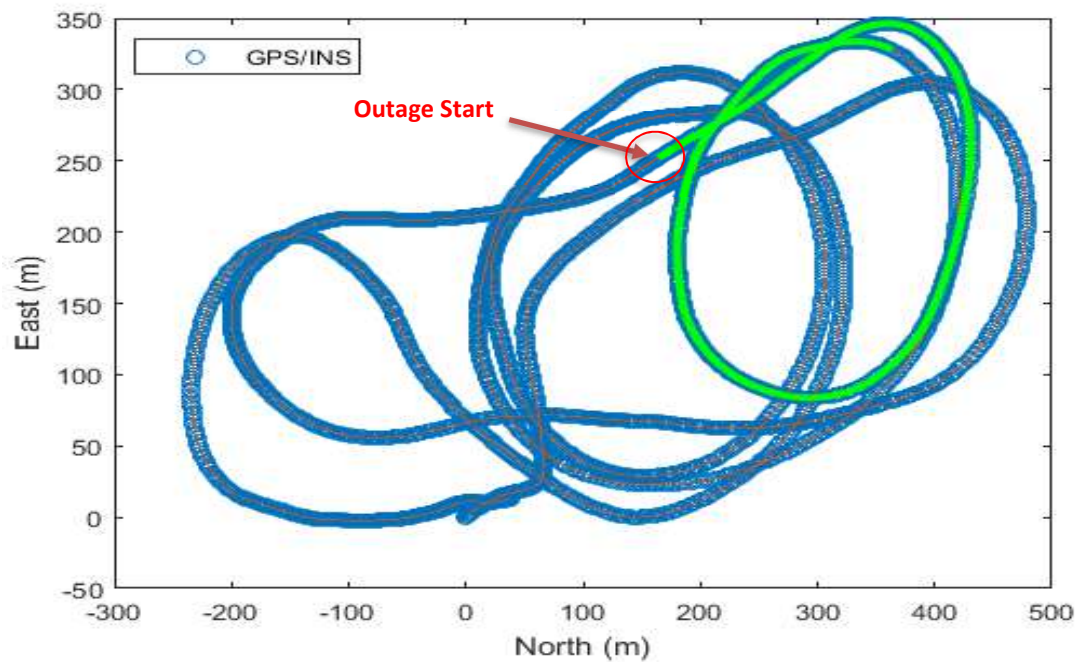


Figure 3-5: Estimated flight trajectory using INS/GNSS Integration without GNSS Outage.

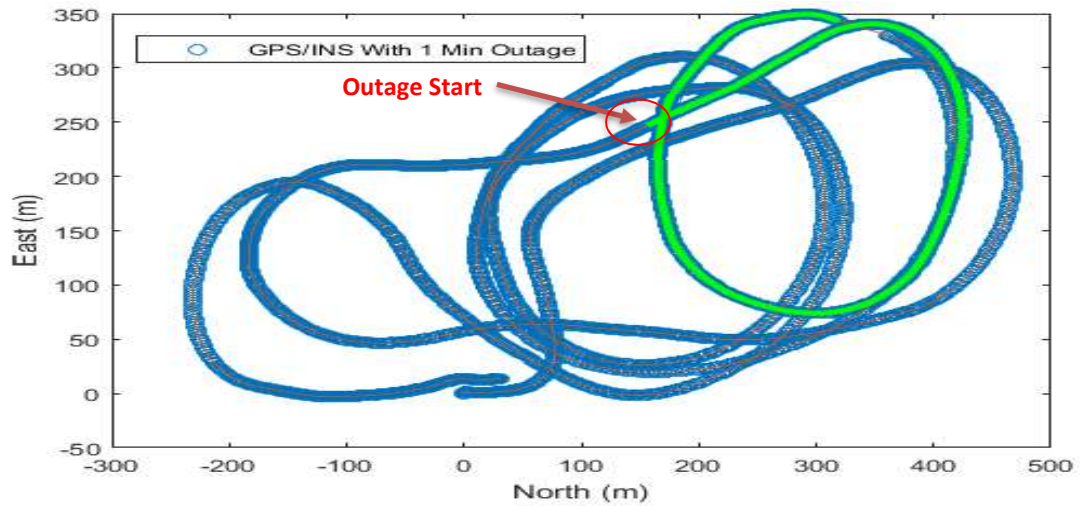


Figure 3-6: Estimated flight trajectory using INS/GNSS integration during 1-min GNSS outage.

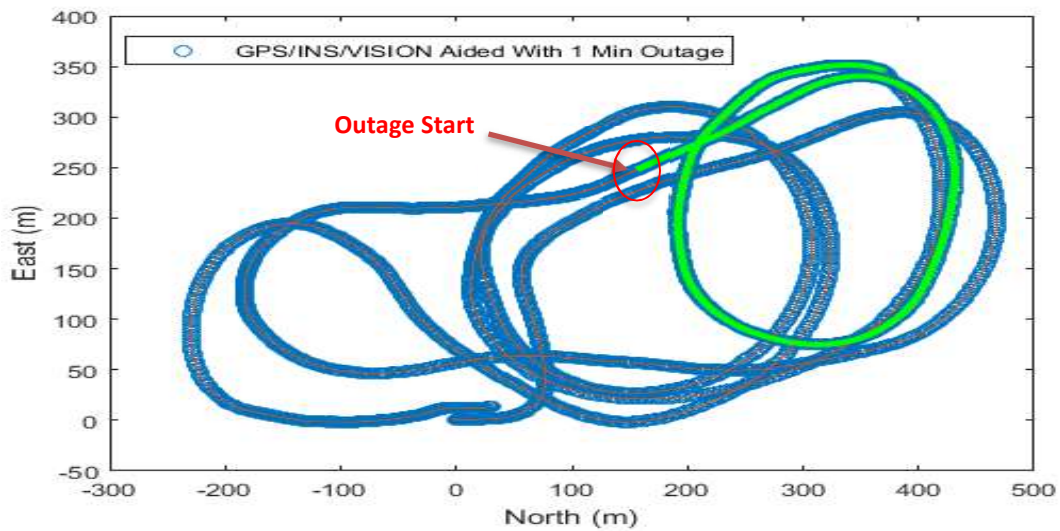


Figure 3-7: Estimated flight trajectory using INS/GNSS/Vision integration during 1-min GNSS outage.

Figure 3-8 shows the flight trajectory in the North direction in (meter) derived from (VAINS) and (INS) during the GNSS signal outage period with respect to the reference trajectory. The reference trajectory is the GNSS/INS integration without any GNSS signal outage. Figure 3-9 shows the flight trajectory in the East direction in (meter) derived from (VAINS) and (INS) during the GNSS

outage period with respect to the reference trajectory. Figure 3-10 shows the flight trajectory in the Height direction in (meter) derived from (VAINS) and (INS) during the GNSS outage period with respect to the reference trajectory.

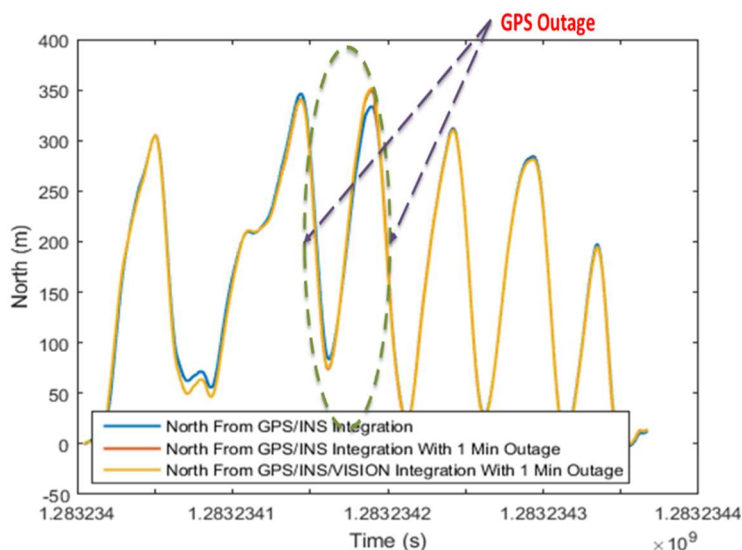


Figure 3-8: Comparison between (North) values derived from (Vision/INS) and (INS) during the GNSS outage period.

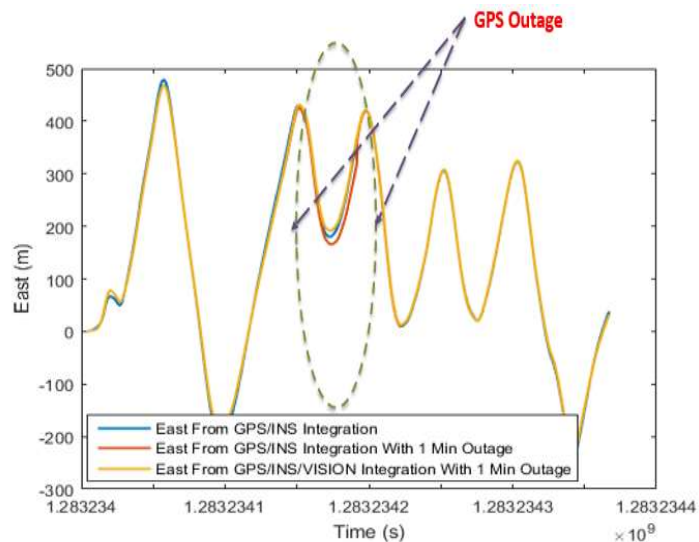


Figure 3-9: Comparison between (East) values derived from (Vision/INS) and (INS) during the GNSS outage period.

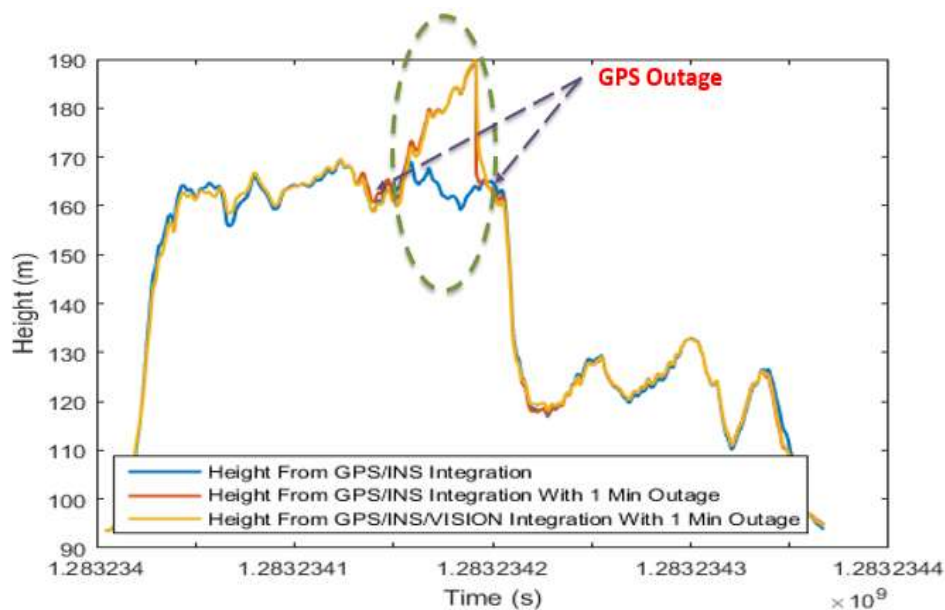


Figure 3-10: Comparison between (Height) values derived from (Vision/INS) and (INS) during the GNSS outage period.

The following table lists RMSE values for all the navigation states that obtained from (VAINS) and (INS) during the GNSS outage period with respect to the reference trajectory. The positioning results (North, East, and Height) indicate that the proposed algorithm is capable of reducing the 3D positioning errors to 75.5 % when compared with the INS drift errors in standalone mode.

Table 3 1: Comparison between RMSE for all the navigation states derived from (VAINS) and (INS) during the GNSS signal outage period.

First Scenario		
RMS Error (m)	Symbol	Outage
North Error (m)	INS	6.1
	VAINS	5.6
East Error (m)	INS	9.1
	VAINS	4.9
Height Error (m)	INS	5.6
	VAINS	5.6

The second scenario is performed after (4 min) from the UAV take-off for 1 min, GNSS signal outage. Figure 3-11 shows the estimated flight trajectory obtained from the GNSS/INS integration without any GNSS signal outages. The green segment represents the location of the GNSS signal outage occurs. Figure 3-12 shows the estimated flight trajectory when simulating one-minute GNSS signal outage. The green segment represents the INS performance in standalone mode

during the outage period. The results show that the INS errors are growing and the position drift rapidly from the ground truth solution during this outage period. Figure 3-13 depicts the estimated flight trajectory by using the proposed VAINS. Figure 3-14 shows the flight trajectory in the North direction in (meter) derived from (VAINS) and (INS) during the GNSS outage period with respect reference to the reference trajectory. The reference trajectory is the GNSS/INS integration without any GNSS signal outage. Figure 3-15 shows the flight trajectory in the east direction in (meter) derived from (VAINS) and (INS) during the GNSS outage period with respect reference to the reference trajectory. Figure 3-16 shows the flight trajectory in the height direction in (meter) derived from (VAINS) and (INS) during the GNSS outage period with respect reference to the reference trajectory. The standard deviation of the estimated forward velocity from the monocular VO is 0.15 m/s.

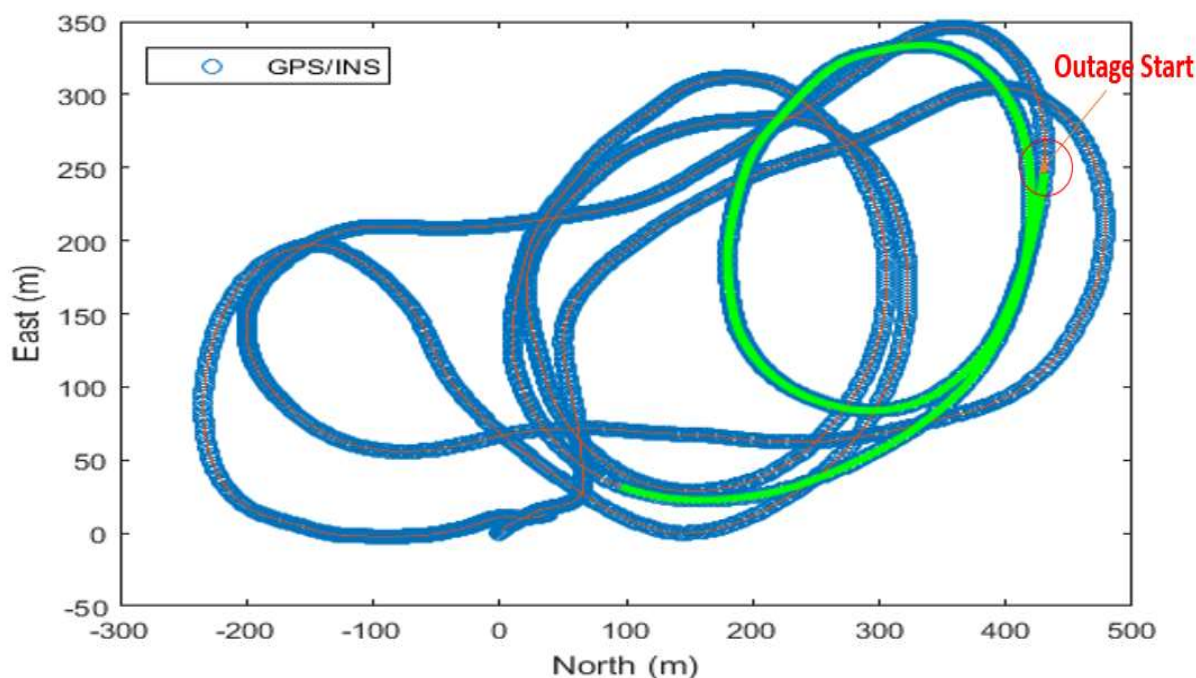


Figure 3-11: Estimated flight trajectory using INS/GNSS Integration without GNSS Outage.

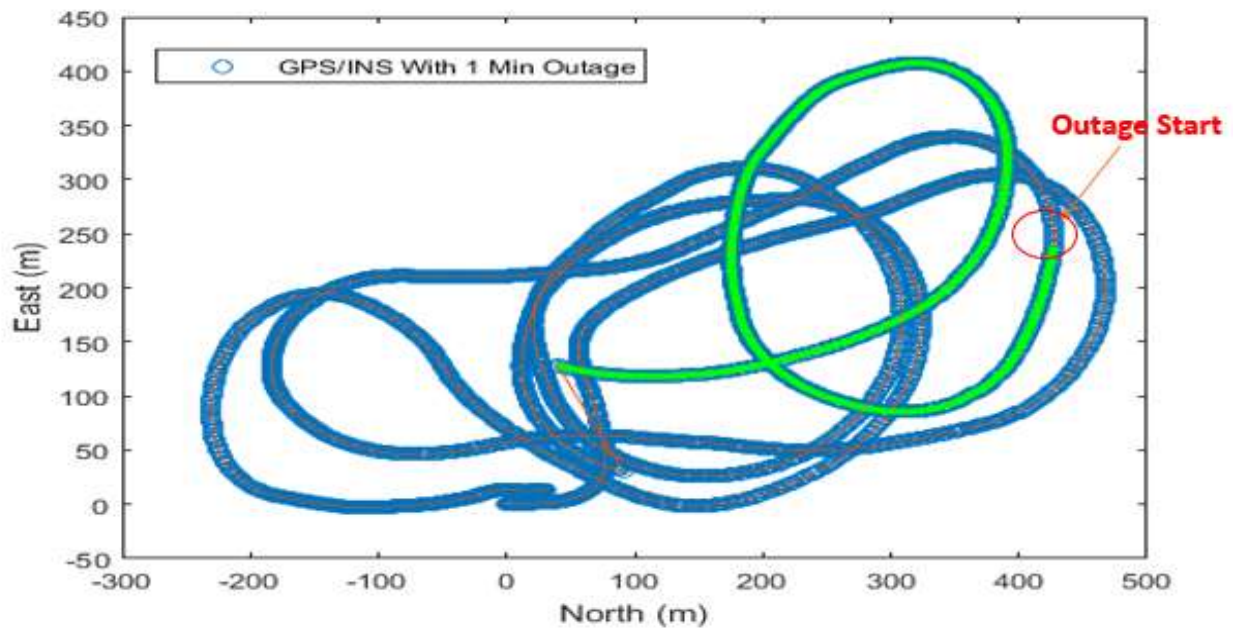


Figure 3-12: Estimated flight trajectory using INS/GNSS integration during 1-min GNSS outage.

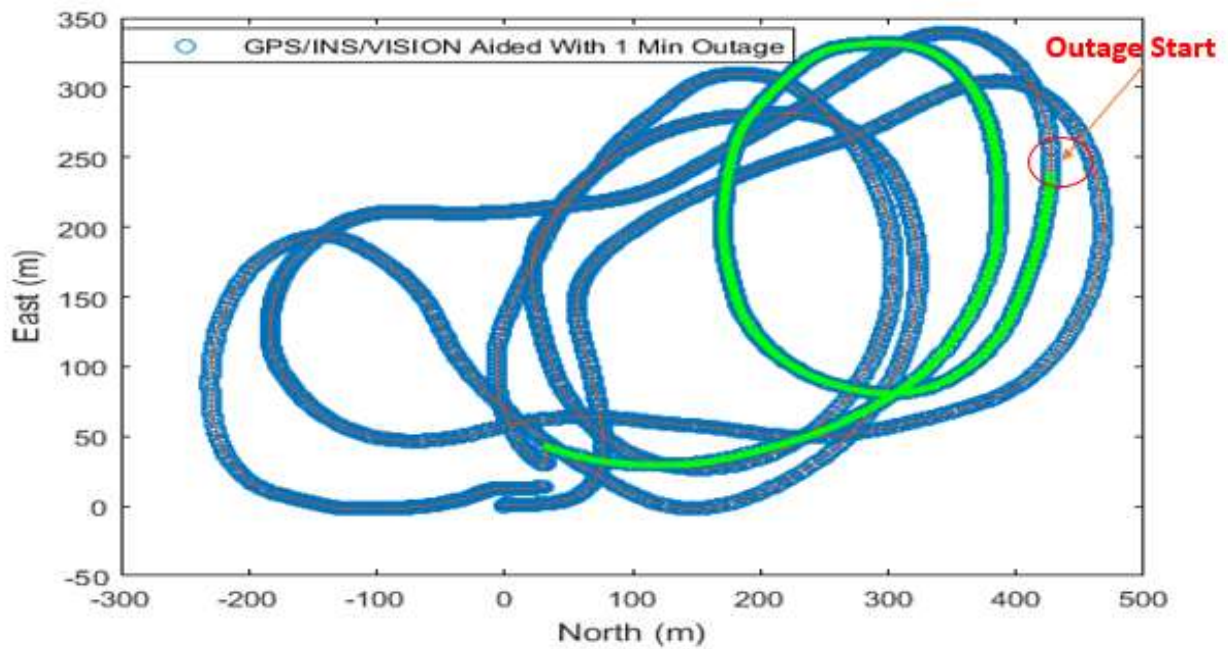


Figure 3-13: Estimated flight trajectory using INS/GNSS/Vision.

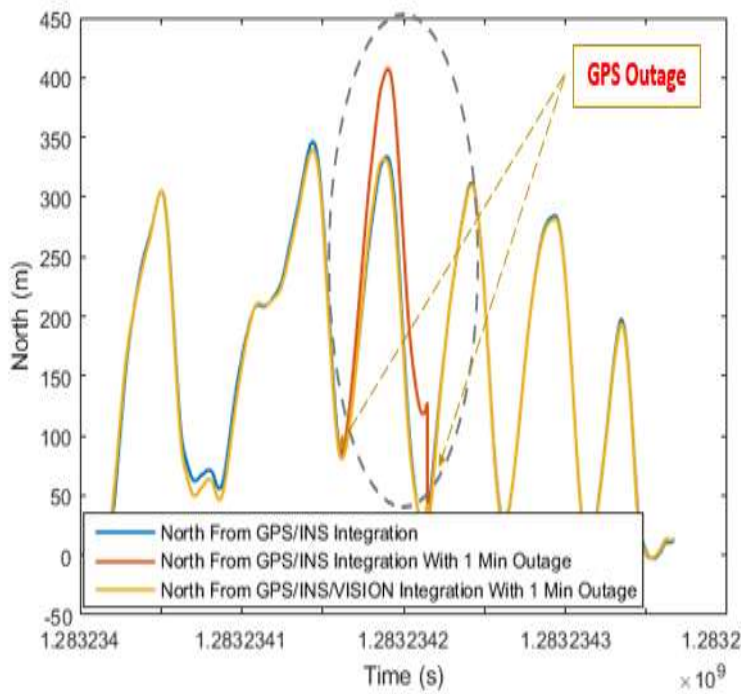


Figure 3-14: Comparison between (North) values derived from (Vision/INS) and (INS) during the GNSS outage period.

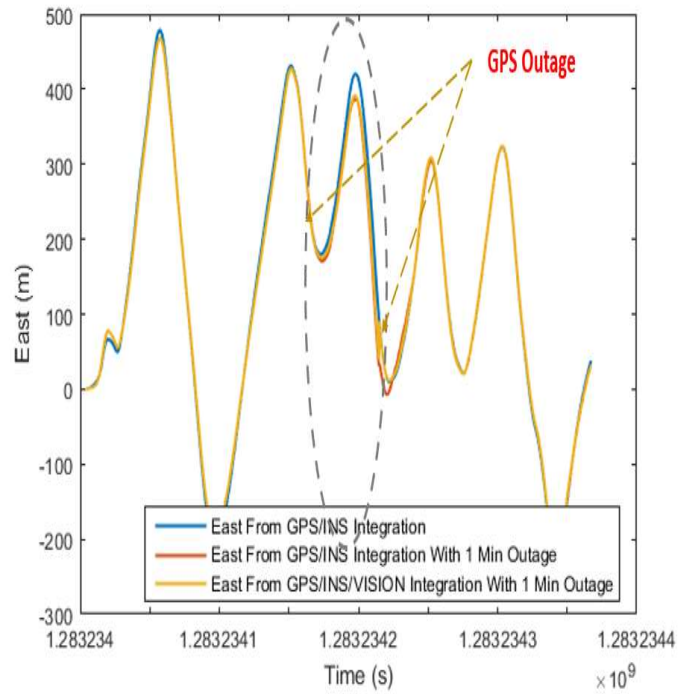


Figure 3-15: Comparison between (East) values derived from (Vision/INS) and (INS) during the GNSS outage period.

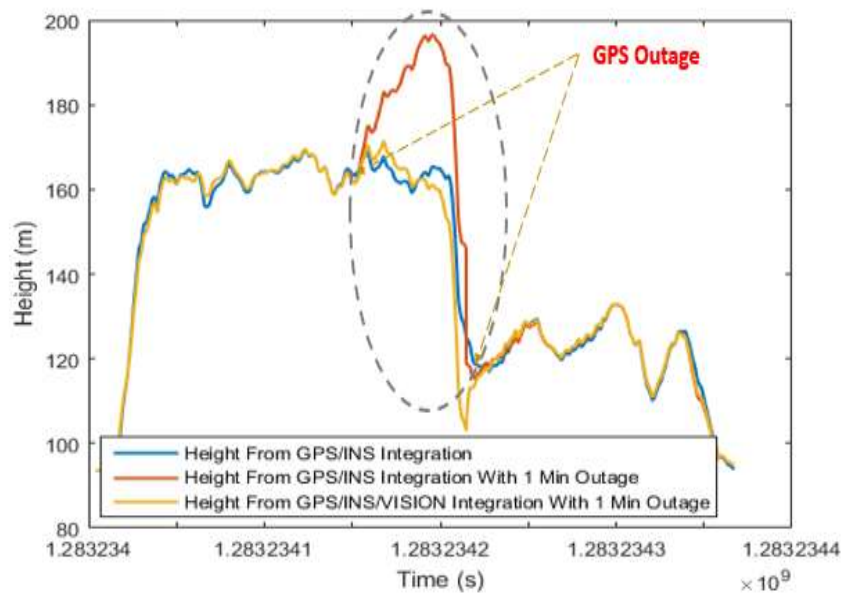


Figure 3-16: Comparison between (Height) values derived from (Vision/INS) and (INS) during the GNSS outage period.

The following table lists RMSE values for all the navigation states that obtained from (VAINS) and (INS) during the GNSS outage period with respect to the reference trajectory. The positioning results (North, East, and Height) indicate that the proposed algorithm can reduce the 3D positioning errors to 48.9 % when compared with the INS drift errors in standalone mode.

Table 3-2: Comparison between RMSE for all the navigation states derived from (VAINS) and (INS) during the GNSS signal outage period.

Second Scenario		
RMS Error (m)	Symbol	Outage
North Error (m)	INS	21.1
	VAINS	5.2
East Error (m)	INS	14.2
	VAINS	11.6
Height Error (m)	INS	8.2
	VAINS	3.1

The two experiments results show that the proposed algorithm reduced the average 3D position errors to 53% of the INS drift errors in standalone mode during the GNSS signal outage period.

3.7 Summary

A monocular VO algorithm based on optical flow and machine learning is proposed to aid the inertial navigation during GNSS signal outage by estimating the velocity component in the forward

direction. The predicted velocity is used to update the inertial navigation system via an EKF to limit its expected drift over time. As the proposed approach learns the relationship between the actual optical flow vectors and the navigation states in real time, it eliminates the need for a calibration phase and inherently models the interior camera parameters, its lever arm and boresight parameters. The results show that the proposed algorithm enhanced the 3D position errors to 47% of the INS drift errors in standalone mode during the GNSS signal outage period. Moreover, the monocular VO technique is capable of recovering the scale before the integration with the INS.

Chapter Four: **Prediction of Inertial Positioning Errors Based on Gaussian Process for UAVs in GNSS Denied Environment**

In this chapter, machine learning approaches have been implemented to predict the INS errors when the GNSS signal is lost. Then, these predicted errors are employed to compensate the INS mechanization output states and to enhance the states accuracy and reliability. GPR based approach is proposed to improve the positioning reliability and accuracy of the INS when the GNSS signal is blocked for short time. An Airborne Dataset is used to assess the performance of the proposed approach.

4.1 Training Session

The primary goal of the training session is to generate a nonlinear underlying function that directly map the inputs to the desired outputs. The training data set is denoted by (x_i, w, y_i) , where x denotes an input vector, w denotes the input weights (hyper-parameters) and y denotes the desired output. GPR-based approach is utilized to achieve this goal and it is used to describe a distribution over functions. It is specified by its mean

$$f(x) \sim GPR(m(x), k(x, x')) \quad (4-1)$$

where $m(x) = E[f(x)]$

This covariance kernel function can take many forms [79]. In this thesis the squared exponential covariance function is used as a covariance kernel function to specify the similarity between pairs of random variables as follows:

$$k(x, x') = \mathbb{E}[(f(x) - m(x))(f(x') - m(x')))] \quad (4-2)$$

The covariance kernel function determines the covariance between output vectors in terms of input vectors and some hyper-parameters. The squared exponential covariance function is used as a covariance kernel function to specify the similarity between pairs of random variables as follows

$$\text{cov}(f(x), f(x')) = k(x, x') = \exp\left(-\frac{1}{2} \frac{|x - x'|^2}{l}\right) \quad (4-3)$$

where l = length scale

The hyper-parameters are optimized during the training session by maximising the log marginal likelihood of the observations $\{x_i, y_i\}$ conditioned on the hyper-parameters. When the GNSS signal is available, the vehicle orientation and velocity components in the body frame that resulted from the mechanization process after EKF error states correction are used as inputs to the GPR during the training session. The estimated velocity (in the body frame) and orientation error states that resulted from the GNSS/INS integration in an EKF are used as outputs to the GPR during this stage. The used velocity components during the training session are transformed into the body frame to reflect the vehicle dynamics properly. Figure 4-1 provides an overview of the proposed system during the training session.

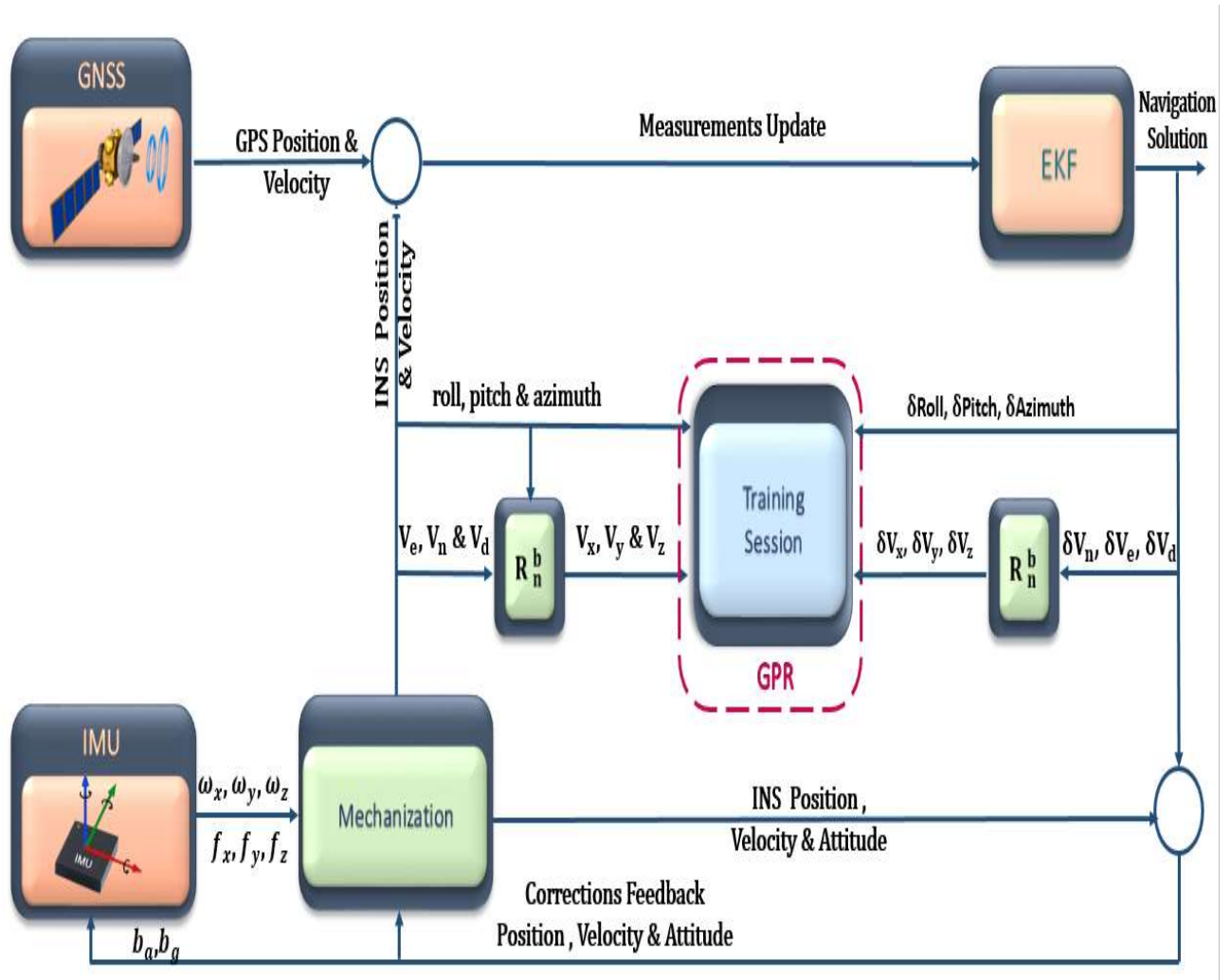


Figure 4-1: Gaussian Process based approach for inertial drift compensation during the training session.

4.2 Prediction Session

Once the GNSS measurements are unavailable, the prediction mode starts to predict the velocity and orientation error states to correct the velocity and orientation drift exhibited by the inertial navigation solution in standalone mode. This error compensation will enhance the 3D position accuracy of the vehicle during the GNSS signal outage. Figure 4-2 provides an overview of the proposed system during the prediction session.

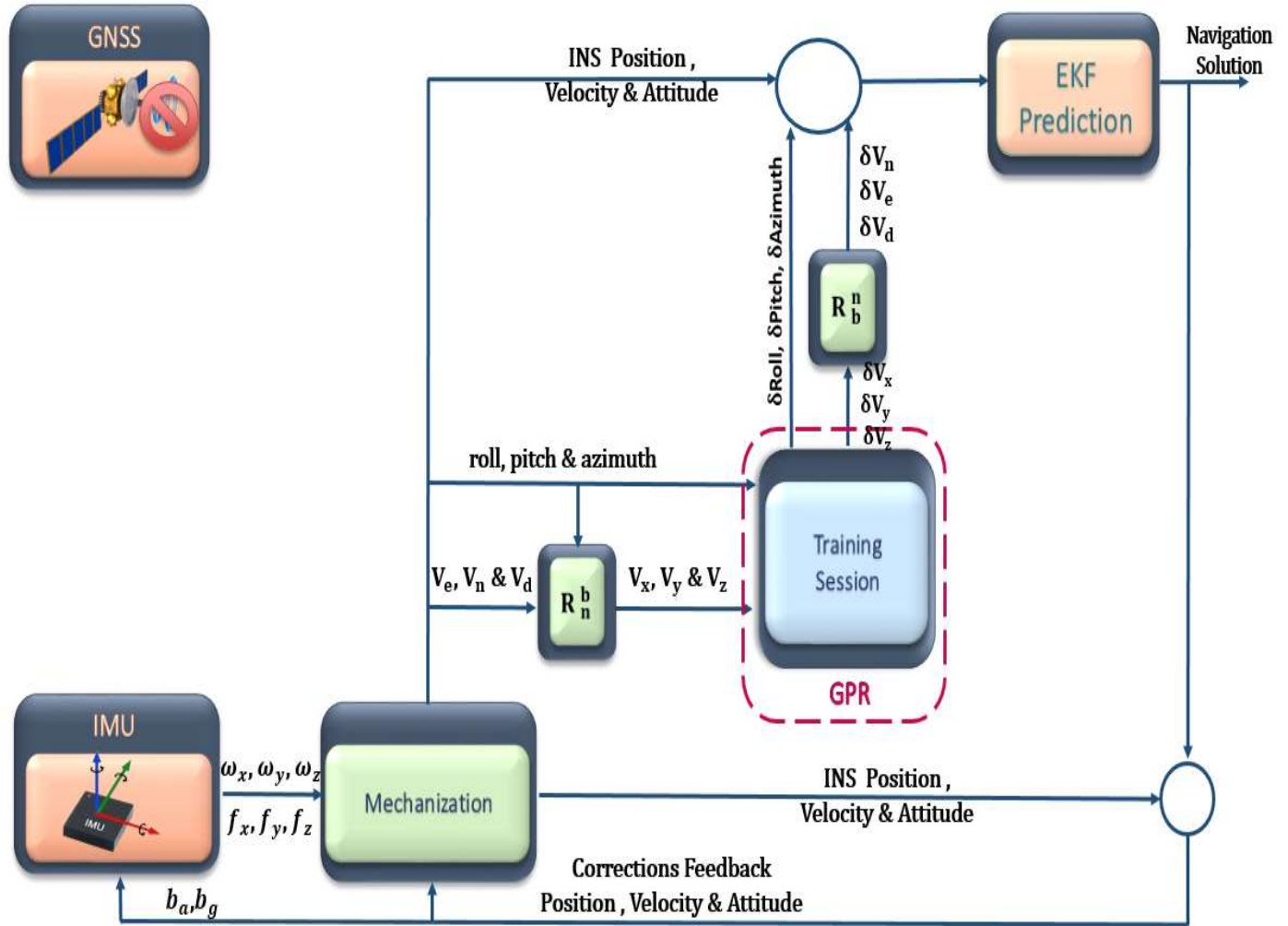


Figure 4-2: Gaussian Process based approach for inertial drift compensation during the prediction session.

The prediction process incorporates the knowledge that obtained by the training data $\{(x_i, f_i | i = 1, \dots, n)\}$ and the new inputs (test points x_*) to predict the new outputs values (test outputs f_*). The joint distribution of the training outputs, f , and the test outputs f_* according to the prior is

$$\begin{bmatrix} f \\ f_* \end{bmatrix} \sim N \left(m(x), \begin{bmatrix} k(x, x) & k(x, x_*) \\ k(x_*, x) & k(x_*, x_*) \end{bmatrix} \right) \quad (4-4)$$

where $k(x, x_*) =$ covariance matrix evaluated at all pairs of training and test points

4.3 Experimental Results

Three experiments are performed in different trajectory parts to evaluate the effectiveness of the proposed algorithm in enhancing the 3D position accuracy during the GNSS signal outage. The UAV flight mission duration is 5.25 minutes. Figure 4-3 illustrates the three-outage periods along the UAV flight trajectory.

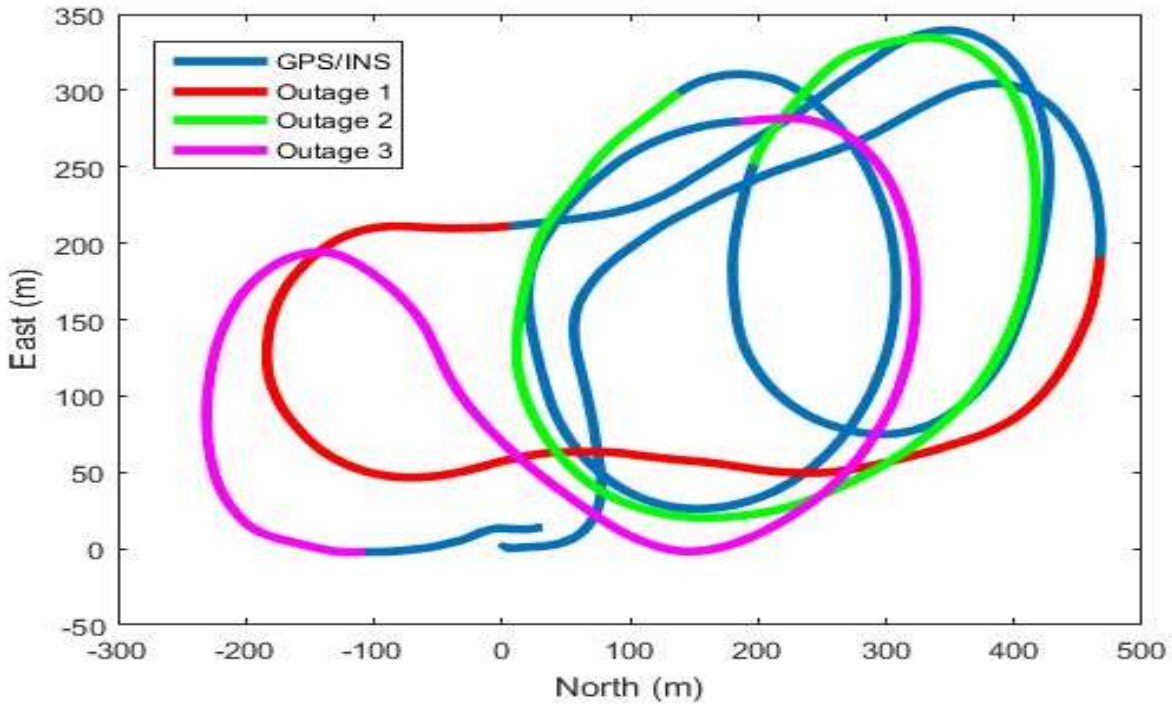


Figure 4-3: Three-outage periods along the UAV flight trajectory.

Figure 4-4 illustrates the time line for the outage periods along the UAV flight trajectory.

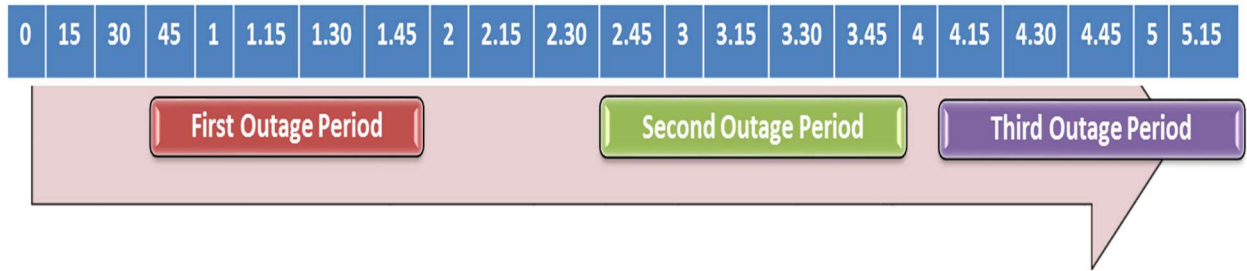


Figure 4-4: Time line for the outage periods.

4.3.1 First Artificial Outage

The first artificial outage period experiment is performed between 45 second to 1.45 minute after the UAV take off. Figure 4-5 illustrates a comparison between the estimated 2D flight trajectory outage segments that obtained from the GNSS/INS integration (ground truth segment), INS in standalone mode and INS with GPR correction.

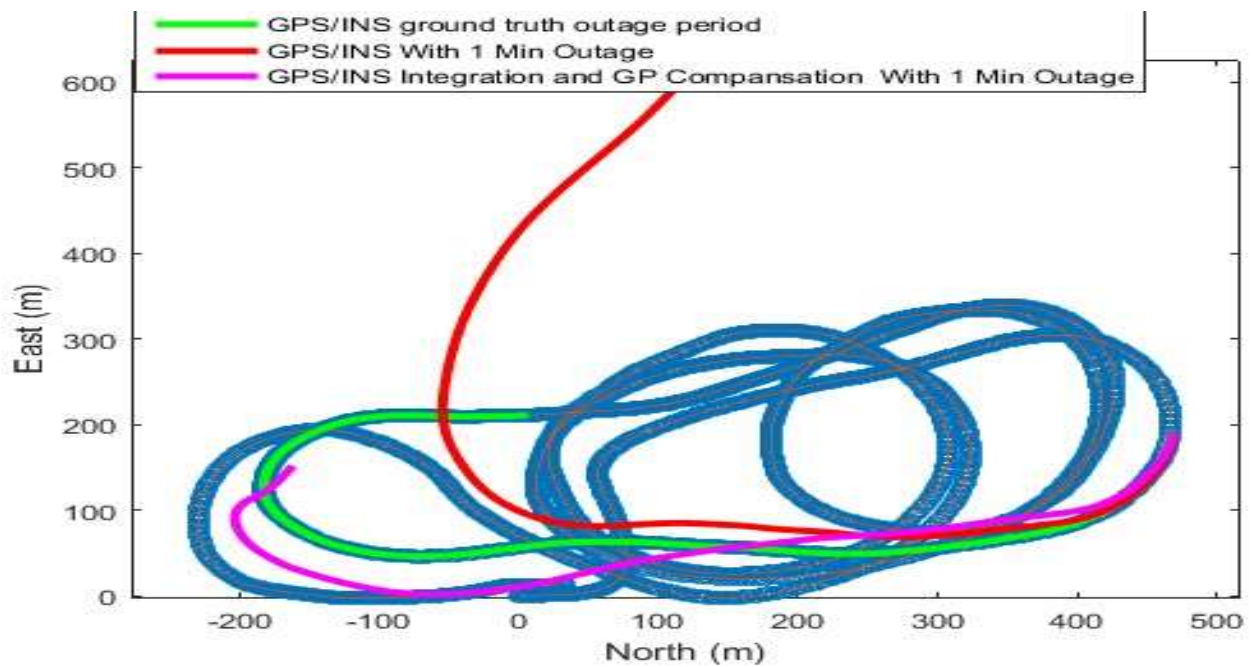


Figure 4-5: Estimated flight trajectory using INS/GNSS Integration without GNSS outage, INS/GNSS Integration with GNSS outage and INS/GNSS Integration with GNSS outage and GPR correction.

Figures 4-6, 4-7 and 4-8 illustrate a comparison between (North, East and Height) position values respectively obtained from (GPR/INS), (INS) during the GNSS outage period with

respect to the ground truth-value. The results indicate that the GPR capable of aiding the INS during a short GNSS signal outage and it demonstrates its ability to reduce the 3D positioning errors to 49.6% of the INS drift errors in standalone mode even with this small learning period (45sec).

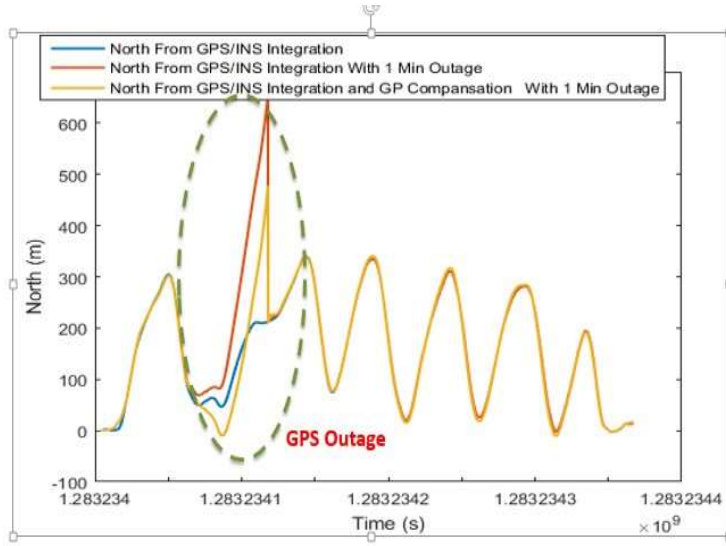


Figure 4-6: Comparison between (North) values obtained from (INS) and (INS with GPR correction) during the GNSS outage period.

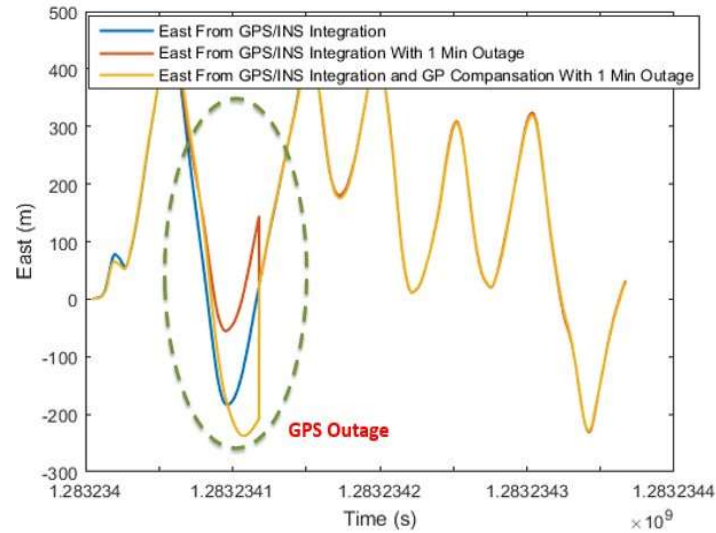


Figure 4-7: Comparison between (East) values obtained from (INS) and (INS with GPR correction) during the GNSS outage period.

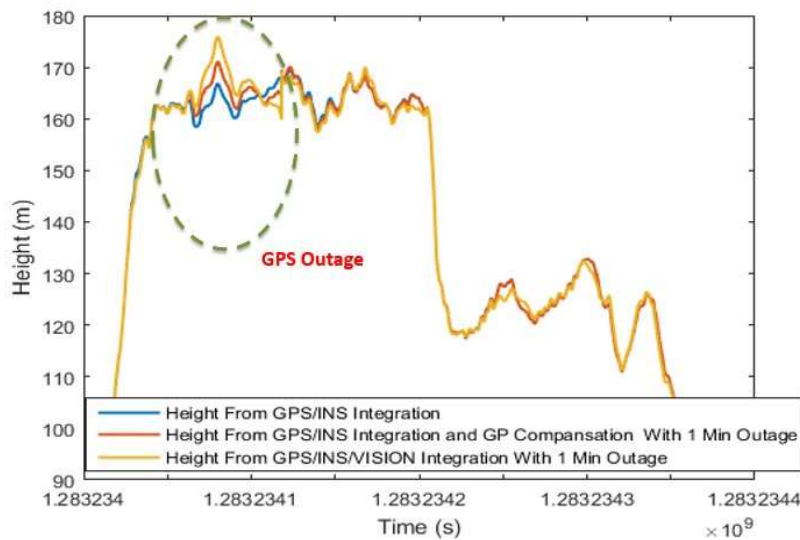


Figure 4-8: Comparison between (Height) values obtained from (INS) and (INS with GPR correction) during the GNSS outage period.

4.3.2 Second Artificial Outage

The Second artificial outage period experiment is performed between 2.45 min to 3.45 min after the UAV take off. Figure 4-9 illustrates a comparison between the estimated 2D flight trajectory outage segments obtained from the GNSS/INS integration (ground truth segment), INS in standalone mode and INS with GPR correction. Figures 4-10, 4-11 and 4-12 illustrate a comparison between (North, East and Height) position values respectively that obtained from (GPR/INS), (INS) during the GNSS outage period with the ground truth-value.

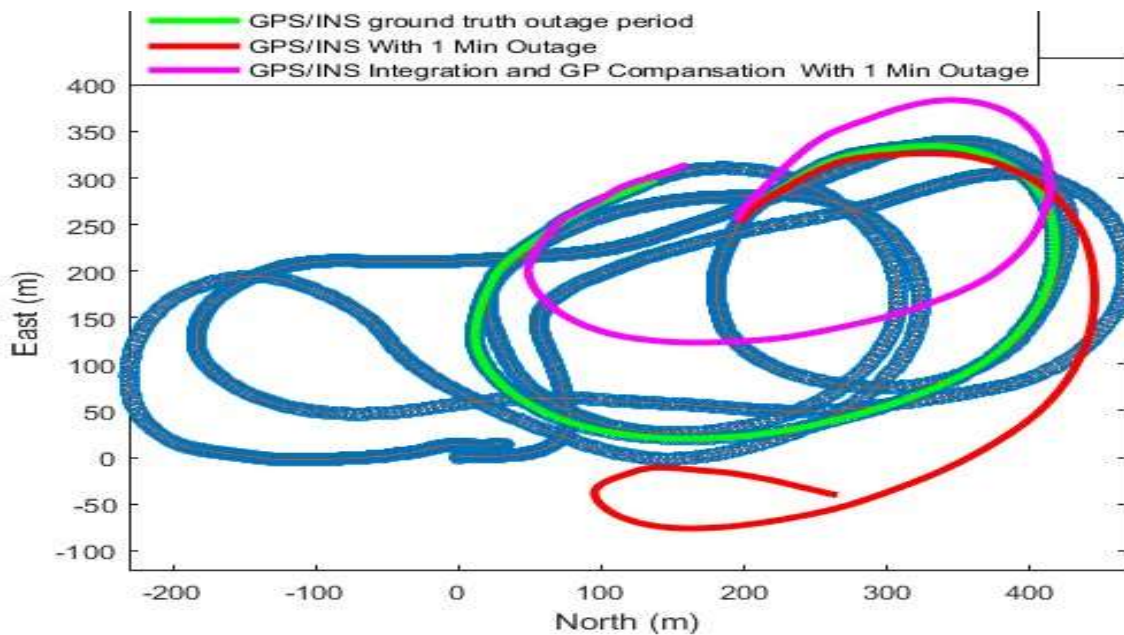


Figure 4-9: Estimated flight trajectory using INS/GNSS Integration without GNSS outage, INS/GNSS Integration with GNSS outage and INS/GNSS Integration with GNSS outage and GPR correction.

The results indicate that the GPR capable of aiding the INS during a short GNSS signal outage and it demonstrates its ability of reducing the 3D positioning errors to 45.7% of the INS drift errors in standalone mode.

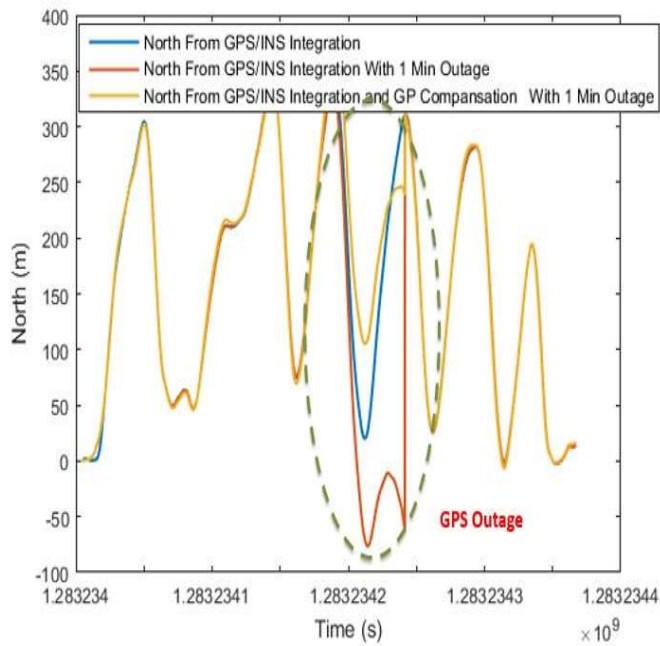


Figure 4-10: Comparison between (North) values obtained from (INS) and (INS with GPR correction) during the GNSS outage period.

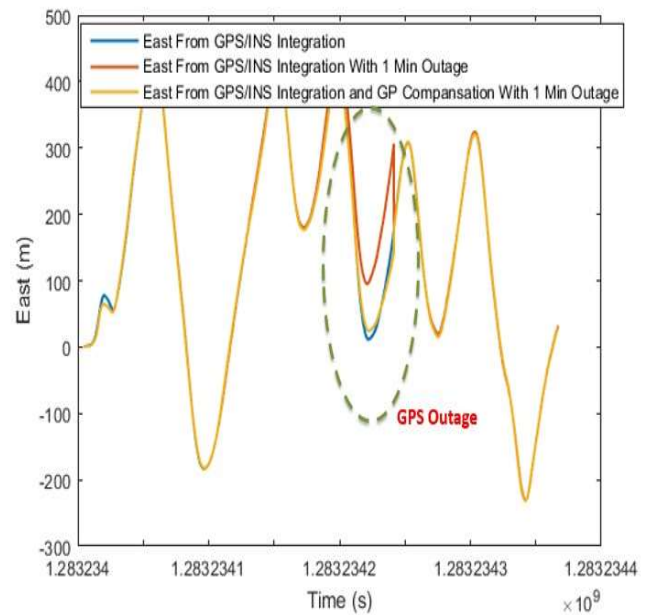


Figure 4-11: Comparison between (East) values obtained from (INS) and (INS with GPR correction) during the GNSS outage period.

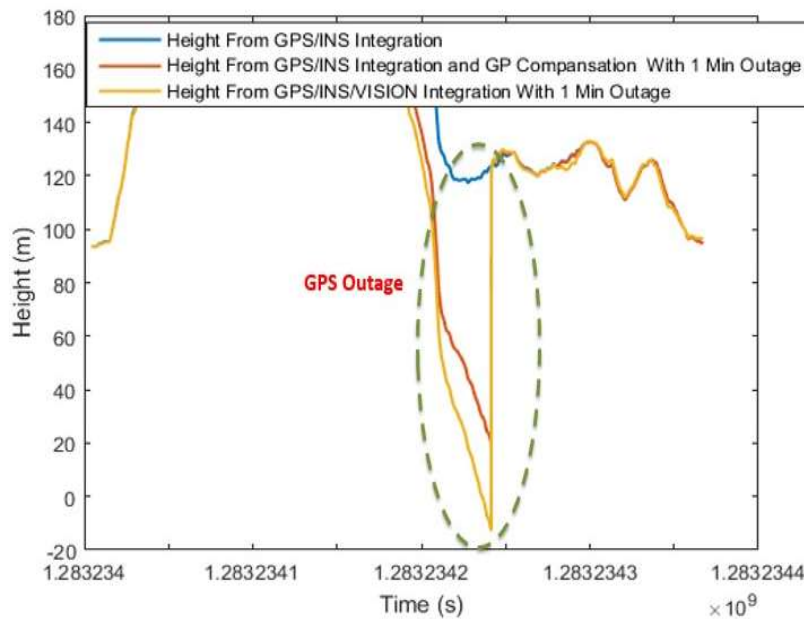


Figure 4-12: Comparison between (Height) values obtained from (INS) and (INS with GPR correction) during the GNSS outage period.

4.3.3 Third Artificial Outage

The third artificial outage period experiment is performed between 4.15 min to 5.15 min after the UAV take off. Figure 4-13 illustrates a comparison between the estimated 2D flight trajectory outage segments that obtained from the GNSS/INS integration (ground truth segment), INS in standalone mode and INS with GPR correction. Figures 4-14, 4-15 and 4-16 illustrate a comparison between (North, East and Height) position values respectively that obtained from (GPR/INS), (INS) during the GNSS outage period with the ground truth-value. The results indicate that the GPR capable of aiding the INS during a short GNSS signal outage and it demonstrates its ability of reducing the 3D positioning errors to 45 % of the INS drift errors in standalone mode.

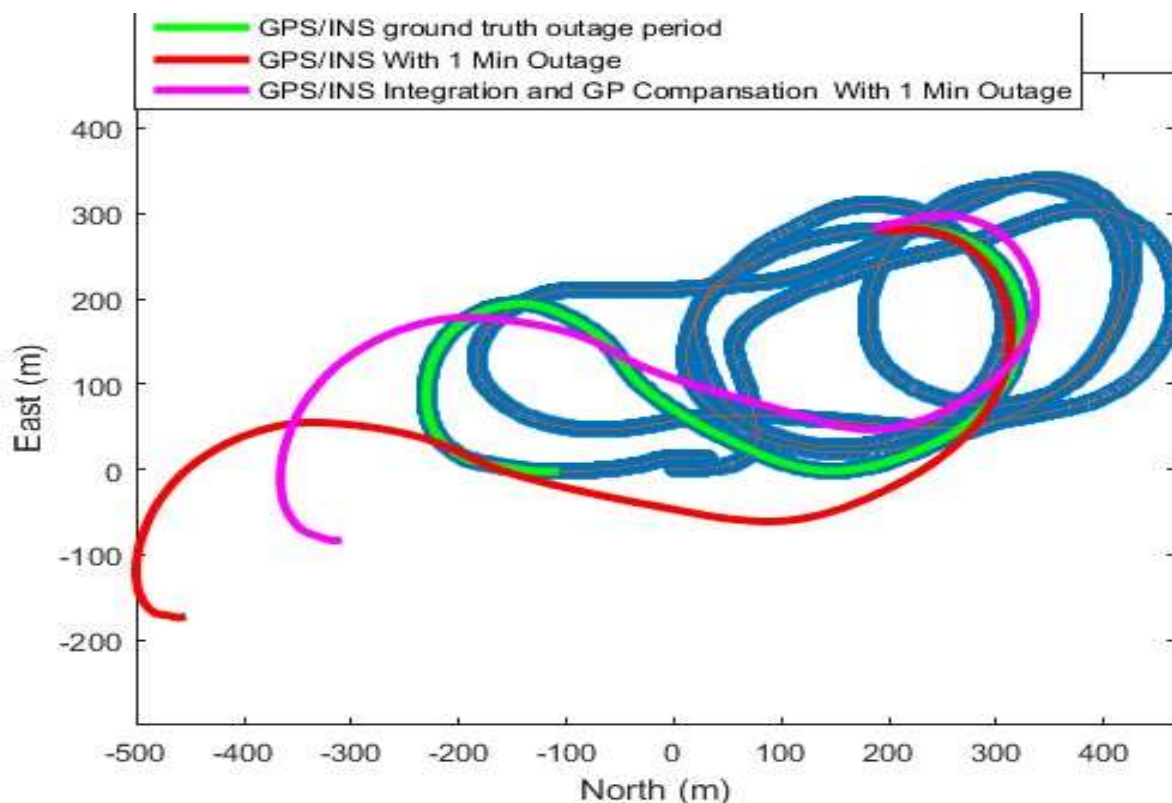


Figure 4-13: Estimated flight trajectory using INS/GNSS Integration without GNSS outage, INS/GNSS Integration with GNSS outage and INS/GNSS Integration with GNSS outage and GPR correction.

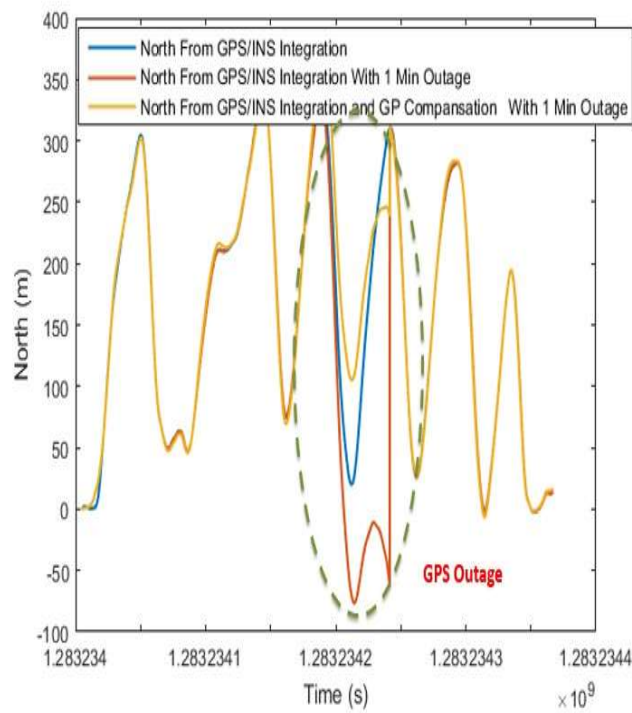


Figure 4-14: Comparison between (North) values obtained from (INS) and (INS with GPR correction) during the GNSS outage period.

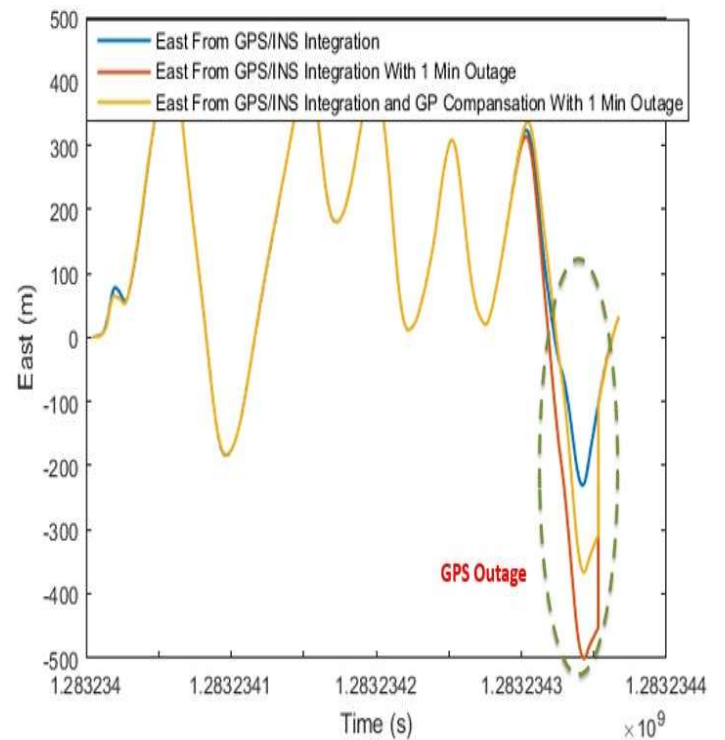


Figure 4-15: Comparison between (East) values obtained from (INS) and (INS with GPR correction) during the GNSS outage period.

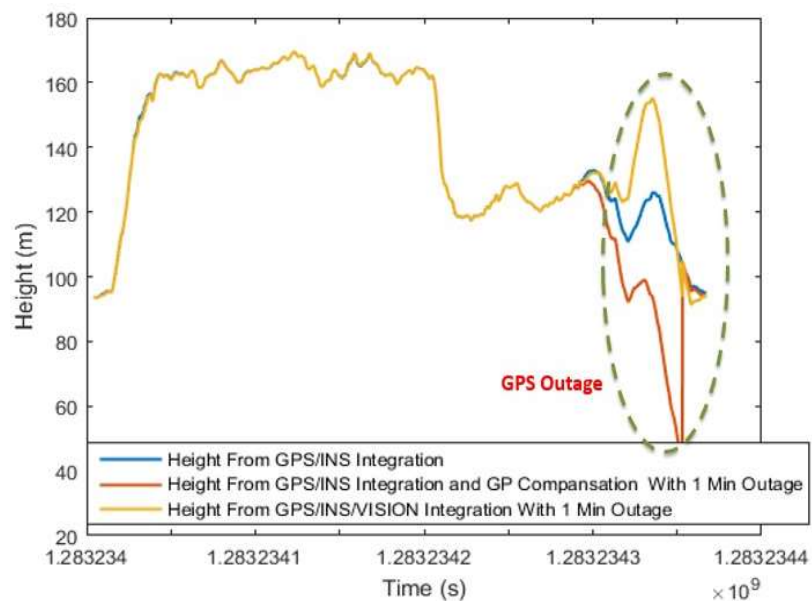


Figure 4-16: Comparison between (Height) values obtained from (INS) and (INS with GPR correction) during the GNSS outage period.

The following table provides a comparison between (RMS Errors) values for the position states that obtained from (INS) and (INS with GPR compensation) during the GNSS outage period with the ground truth-values. The results indicate that the proposed algorithm is outperforming the INS during the GNSS signal outage. Moreover, this technique reduced the average 3D positioning errors to 46.7% of the INS drift errors in standalone mode.

Table 4-1: Comparison between (RMS Errors) values for the position states that obtained from (INS) and (INS with GPR).

RMS Error (m)	First	Second	Third
	Outage	Outage	Outage
INS North Error (m)	66	66.2	46.1
INS&GPR North Error (m)	26.2	28.3	19.6
INS East Error (m)	40	29.3	71.2
INS&GPR East Error (m)	27.9	10.5	32.6
INS Height Error (m)	1.1	23.3	12.1
INS&GPR Height Error (m)	1.9	17.4	6.3
INS 3D position Error (m)	77.2	76.1	85.6
INS&GPR 3D Error (m)	38.3	34.8	38.5
INS&GPR Enhancement %	50.4%	54.3%	55%

4.3.4 Forth Artificial Outage

To assess the GPR ability to model the drift errors, another artificial outage period is performed between min 2.00 to min 3.00 after the UAV take off where an extensive tuning has been

performed to remove the bias errors as much as possible during this minute. Figure 4-17 illustrates a comparison between the estimated 2D flight trajectory outage segments that obtained from the GNSS/INS integration (ground truth segment), INS in standalone mode and INS with GPR correction. Figures 4-18, 4-19 and 4-20 illustrate a comparison between (North, East and Height) position values respectively that obtained from (GPR/INS), (INS) during the GNSS outage period with the ground truth-value. The results indicate that the 3D positioning errors obtained by GPR is worse than the INS in standalone mode by 75.2%. The experiment illustrates the disability of GPR to predict the random noise behavior

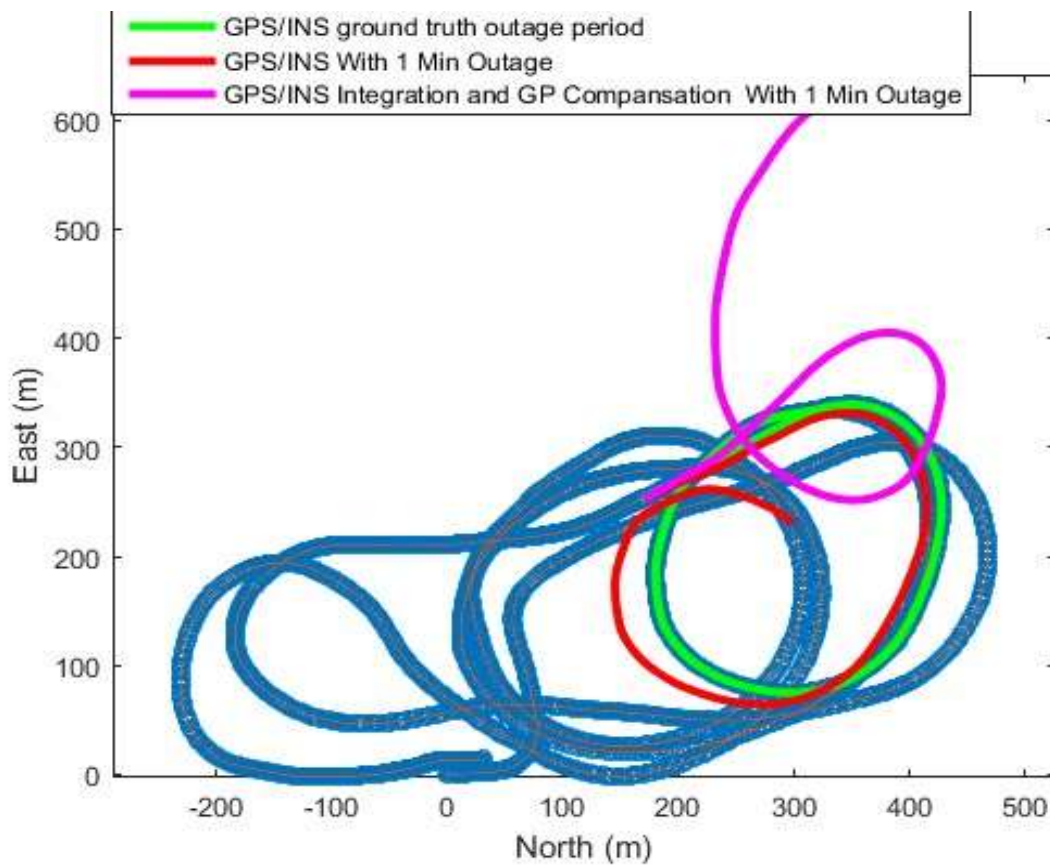


Figure 4-17: Estimated flight trajectory using INS/GNSS Integration without GNSS outage, INS/GNSS Integration with GNSS outage and INS/GNSS Integration with GNSS outage and GPR correction.

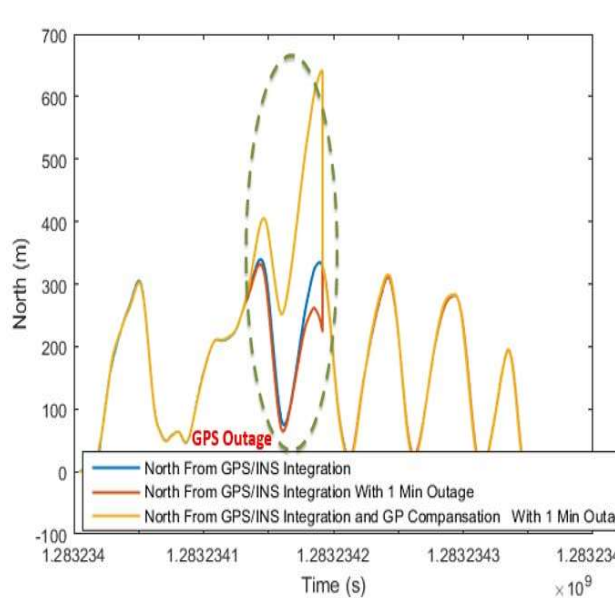


Figure 4-18: Comparison between (North) values obtained from (INS) and (INS with GPR correction) during the GNSS outage period.

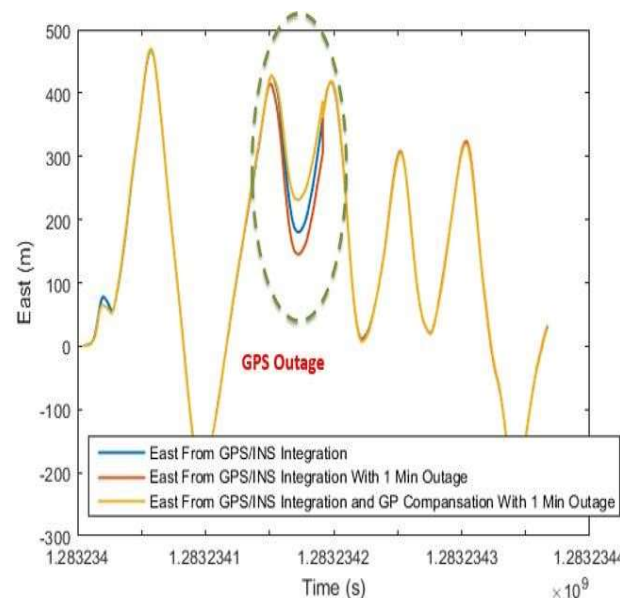


Figure 4-19: Comparison between (East) values obtained from (INS) and (INS with GPR correction) during the GNSS outage period

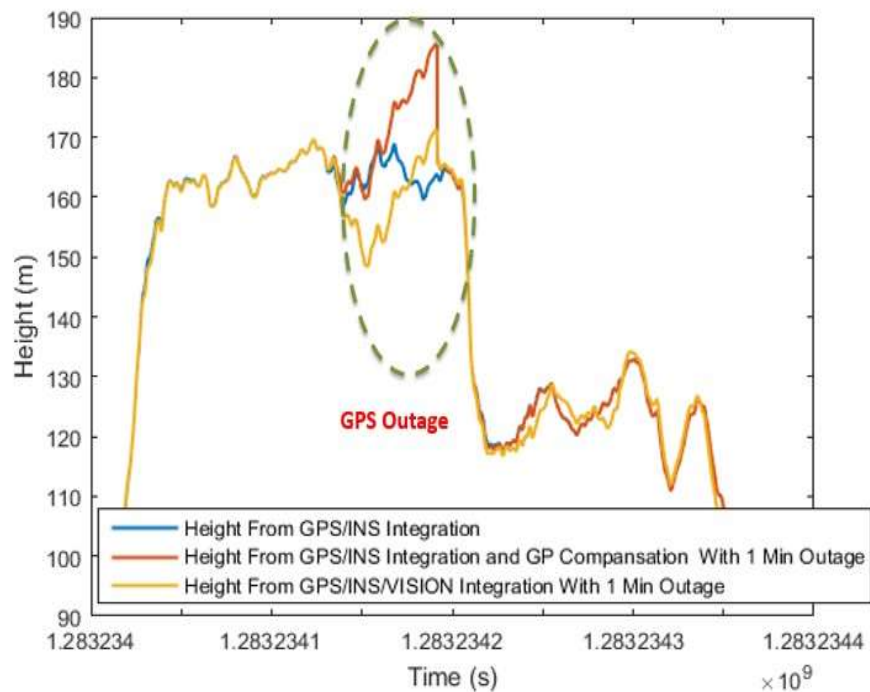


Figure 4-20: Comparison between (Height) values obtained from (INS) and (INS with GPR correction) during the GNSS outage period.

4.4 Summary

A GPR based approach is proposed to aid the inertial navigation during GNSS outage periods. The vehicle orientation and velocity components in the body frame that resulted from the mechanization process after the EKF error states correction are used as inputs to the GPR during the learning session. The estimated velocity (in the body frame) and orientation error states that resulted from the GNSS/INS integration in an (EKF) are used as outputs to the GPR during this stage. During the GNSS, signal outage, the predicted velocity and orientation error states from the GPR algorithm are used to compensate the INS mechanization velocity and orientation drift errors. The proposed system is evaluated through three outage periods.

An airborne dataset is used to test the proposed approach; this dataset is gathered from a radio-controlled aircraft flown at Kagaru, Queensland, Australia on 31/08/10 (Warren et al. 2014).

The test used the XSens Mti-g INS/GNSS onboard unit to offer the navigation solution with the help of a USB NMEA GNSS. The experiments results indicate that, the GPR algorithm can reduce the average INS 3D positioning errors to 46.7% of the average INS drift errors in standalone mode during the GNSS signal outage even with a short learning period. In addition, the experiments illustrate the ability of GPR to predict only the main trends (due to biases errors) and its failure to predict the random noise behavior.

Chapter Five: A Smart Hybrid VAINS Approach for UAVs in GNSS Denied Environment

Although a variety of monocular VO-based on photogrammetric, Structure from Motion, and machine learning approaches have been proposed to assist the navigation process, the accuracy of 3D positioning using these techniques is still affected by some factors such as the lack of the observed features, the incorrect matches (outliers), and the sensor biases (i.e. IMU). Therefore, the development of a reliable navigation system that can handle such challenges is necessary.

In this study, a novel smart hybrid vision aided inertial navigation system is proposed based on the main idea of optical flow-based for vision-aided inertial navigation using regression trees [83].

Our previous monocular VO system [83] eliminates the need for a calibration phase and inherently models the interior camera parameters, its lever arm and boresight parameters since, the relationship between the actual optical flow vectors and the navigation states are implicitly modeled in the monocular VO. This monocular VO technique can resolve the scale ambiguity problem by implicitly modeling the scale on its trained regression model. The employment of regression trees algorithm in the monocular VO enabled predicting the vehicle forward velocity even with the partial availability of optical flow vectors. The proposed system in this thesis extends our previous work as follows

- The proposed system attempts to correct the VO and INS systems used by the previous work [83] by predicting both monocular VO drift and INS drift based on trained GPR [84] against GNSS reference data.

- The proposed system has a real-time training performance since the monocular VO, GPR for INS and, GPR for monocular VO training times are 0.027, 0.018, and, 0.012 s respectively for a one minute of collected data. Such computational performance allows a real-time and incremental training of the employed GPRs whenever the GNSS is available as reference to enhance the learnt GPR and capture the recent and new drift behaviors over time.
- In contrary to many other machine learning drift prediction approaches, the employed GPR can provide both predictions and their associated uncertainties to be utilized to assess the quality of the GPRs predicted states and to decide when these corrections are applied to the monocular VO and INS outputs and when are discarded.
- Unlike many other approaches that depend on a priori collected data for the training purpose, the proposed training process can take place during the flight upon availability of reference GNSS data. Such ability enables the system to capture the effect of sensor parameter changes from flight to another as it allows using the most recent data for training.

The proposed system handles both the INS and VO drifts in a smart fashion as the proposed system does not employ a single off-line training session before the operation. Instead, it adopts a real-time and incremental learning sessions whenever the GNSS is available as reference to enhance the learnt GPR and capture the recent and new drift behaviors over time. In contrary to many other visual/INS navigation approaches that adopt a single training session such as [70], the proposed

incremental learning allows the system to adapt its model for new VO/INS drift behavior that emerge during the flight and allows in-situ learning if no prior data is available for training.

5.1 Overview of the System Architecture

The proposed system employs monocular VO, INS, EKF, and GPR. In addition, this system consists of three main blocks, which are, 1) monocular VO [83], 2) GPR for INS drift prediction [84] and, 3) GPR for monocular VO drift prediction. All these blocks are integrated together to obtain a more accurate navigation solution.

The employed machine-learning approaches consist of two sessions, which are training and prediction. During the training phase, the GNSS/INS derived navigation states are utilized as a ground truth inputs for these different blocks to build the proper underlying function, which maps the inputs to the desired outputs. The training takes place during the flight (even if no previous data are available for training purpose). The best performance from the proposed system is expectedly achieved when all three blocks have been trained while the GNSS signals are available. For example, if the GNSS signal is lost after the training of the first and second blocks and before the training of the third block, the navigation solution will be based on the first and second blocks only. On the other hand, if the GNSS signals are available for long time, the third block can be trained, and the navigation solution will be based on the three blocks. The proposed system employs the different types of predictions (Monocular VO, VO drift, INS drift) in a hybrid fashion and it switches between the usage of these predictions based on the availability of their accomplished learning at each time.

In the proposed system, the GPR has two functionalities. (a) The first, GPR is utilized to predict the velocity and orientation error states and correct the velocity and orientation drifts exhibited by the inertial navigation mechanization output, and (b) The second, GPR is used to obtain the velocity errors in the flight path direction between the ground truth (GNSS/INS) and the predicted velocity component from the monocular VO during the GNSS signal outage. The main benefit of using such scheme is its ability to model the different drift errors (monocular VO drift and INS drift) when the GNSS measurements are available and to predict those errors during the GNSS signal outage. This helps to improve the system reliability. This system is implemented in 6 major steps as follows:

- 1) Extraction of optical flow parameters.
- 2) GNSS/INS integration
- 3) GPR-based INS drift correction.
- 4) Monocular VO based on optical flow and regression trees.
- 5) VAINS (monocular VO/INS integration).
- 6) GPR-based monocular VO drift correction.

5.2 Modes of Operation and Data Fusion

The system consists of three main operational phases. The first and second phases are considered upon the GNSS signal availability while the third phase is when the GNSS signal is lost. The first phase is a training session for the monocular VO and INS drift predictor (GPR). The second phase is the training stage for the monocular VO drift predictor (GPR) to model the errors associated with the predicted velocity from the monocular VO. The third phase is a prediction stage for the monocular VO drift predictor (GPR) when the GNSS signal are lost.

5.2.1 First Phase

During this phase, our system extracts the optical flow vectors based on the same algorithms which have been utilized in chapter 3.

The GNSS signal is assumed to be available during the first phase. To fuse the onboard IMU with the GNSS measurements in an EKF, the IMU (accelerometer and gyro) raw measurements in the body frame are integrated over time via a mechanization algorithm to obtain the navigation states (i.e., position, velocity, and attitude) in the navigation frame (n-frame). The INS mechanization output states are then combined with GNSS measurements in an EKF to correct the accumulated INS drift errors. The EKF error state vector that has been used to aid the INS is, therefore, a 15-state, as follows:

$$x = \begin{bmatrix} \delta r^n \\ \delta v^n \\ \varepsilon^n \\ b \\ d \end{bmatrix} \quad (5-1)$$

where $\delta r^n, \delta v^n, \varepsilon^n$ are the (position, velocity and attitude) error vector of INS mechanization and b, d are the bias vector of the (accelerometers and gyros), respectively. The system model that represents different INS error states can be obtained by applying the linear perturbation approach to the mechanization equations and can be described using the following first order state equations:

$$\dot{x} = Fx + Gw \quad (5-2)$$

where F is the state dynamic matrix, x is the error states, G is the noise coefficient matrix and w is the system noise. The first order Gauss-Markov model was utilized for modeling the inertial

sensor biases. After discretization of Equation 5-2, the discrete KF system state equation that represents the prediction of error states is given as:

$$\hat{x}_{k+1}^- = \Phi_k \hat{x}_k \quad (5-3)$$

The Prediction of error states covariance matrix can be obtained as follows:

$$P_{k+1}^- = \Phi_k P_k \Phi_k^T + \bar{G}_k Q_k \bar{G}_k^T \quad (5-4)$$

where Φ_k is the state transition matrix, P_k is the state covariance matrix, \bar{G}_k is the discretized noise coefficient matrix and Q_k is the covariance matrix of system noise.

$$K_k = P_k^- H_k^T (H_k P_k^- H_k^T + R_k)^{-1} \quad (5-5)$$

$$\hat{x}_k = \hat{x}_k^- + K_k \delta z_k \quad (5-6)$$

$$P_k = (I - K_k H_k) P_k^- \quad (5-7)$$

where K_k is the Kalman gain, R_k is the measurements covariance matrix and H_k is the design matrix. The IMU and the GNSS antenna cannot be fixed at the same place in the vehicle, the difference between the GNSS antenna position and the IMU position is called the lever-arm effect.

This lever-arm can be described as follows:

$$r_{\text{GNSS}}^n = r_{\text{IMU}}^n + D^{-1} C_b^n l_{\text{GNSS}}^b \quad (5-8)$$

$$D^{-1} = \begin{bmatrix} 1 & 0 & 0 \\ \frac{1}{R_M + h} & 0 & 0 \\ 0 & \frac{1}{(R_N + h) \cos \varphi} & 0 \\ 0 & 0 & -1 \end{bmatrix} \quad (5-9)$$

$$R_M = \frac{R(1 - e^2)}{(1 - e^2 \sin^2 \varphi)^{3/2}} \quad (5-10)$$

$$R_N = \frac{R}{(1 - e^2 \sin^2 \varphi)^{1/2}} \quad (5-11)$$

where r_{GNSS}^n and r_{IMU}^n are the positions of the GNSS antenna center and the center of the inertial sensor in the navigation frame, l_{GNSS}^b is the lever-arm between the GNSS antenna and the IMU in the body frame, C_b^n is the rotation matrix between the body and navigation frame, R is the equatorial earth radius, e is the eccentricity of the earth ellipsoid, and φ is the latitude, R_M and R_N are the meridian and prime vertical radii of curvature for the ellipsoid at a given latitude. The computed position at the center of the GNSS antenna can be obtained from the truth model in Equation 5-8 as follows:

$$\begin{aligned} \hat{r}_{\text{GNSS}}^n &= \hat{r}_{\text{IMU}}^n + D^{-1} C_b^n l_{\text{GNSS}}^b \\ &= r_{\text{IMU}}^n + D^{-1} \delta r_{\text{IMU}}^n + D^{-1} [I - (\emptyset \times)] C_b^n l_{\text{GNSS}}^b \\ &= r_{\text{GNSS}}^n + D^{-1} \delta r_{\text{IMU}}^n - D^{-1} (\emptyset \times) C_b^n l_{\text{GNSS}}^b \\ &= r_{\text{GNSS}}^n + D^{-1} \delta r_{\text{IMU}}^n + D^{-1} (C_b^n l_{\text{GNSS}}^b \times) \emptyset \end{aligned} \quad (5-12)$$

The measured position by the GNSS can be written as

$$\tilde{r}_{\text{GNSS}}^n = r_{\text{GNSS}}^n + D^{-1} e_r \quad (5-13)$$

where e_r is the GNSS position measurement error and \emptyset is the angle error. From Equation

5-12 and Equation 5-13 the residual for the EKF is

$$\begin{aligned}
\delta z_r &= D(\hat{r}_{GNSS}^n - \tilde{r}_{GNSS}^n) \\
&= \delta r_{IMU}^n + (C_b^n l_{GNSS}^b \times) \delta - e_r \\
&= [I_{3 \times 3} : 0_{3 \times 3} : C_b^n l_{GNSS}^b : 0_{3 \times 6}] x - e_r
\end{aligned} \tag{5-14}$$

From Equation (5-14) the design matrix can be expressed as

$$H_k = [I_{3 \times 3} : 0_{3 \times 3} : C_b^n l_{GNSS}^b : 0_{3 \times 6}] \tag{5-15}$$

First phase is also a training session for the INS drift predictor (GPR) which attempts to model the main trend for the INS drift errors by generating a nonlinear underlying function [43]. The inputs of the GPR are the vehicle orientation and velocity components in the body frame that resulted from the mechanization process after EKF error states correction. The estimated velocity (in the body frame) and orientation error states that resulted from the GNSS/INS integration in an EKF are then used as outputs to the GPR during this stage. The used velocity components during the training session are finally transformed into the body frame to reflect the vehicle dynamics properly. Furthermore, this phase is a training session for the monocular VO. This VO is based on regression trees algorithm [85]. The roll, pitch, azimuth, height, and velocity components in the body frame that have been estimated from the GNSS/INS integration and the extracted optical flow vectors are used as inputs during this training stage. The velocity change in the flight path

direction between the previous and current frame is applied as output during this stage [80].

Figures 5-1 illustrates the proposed system during the first phase.

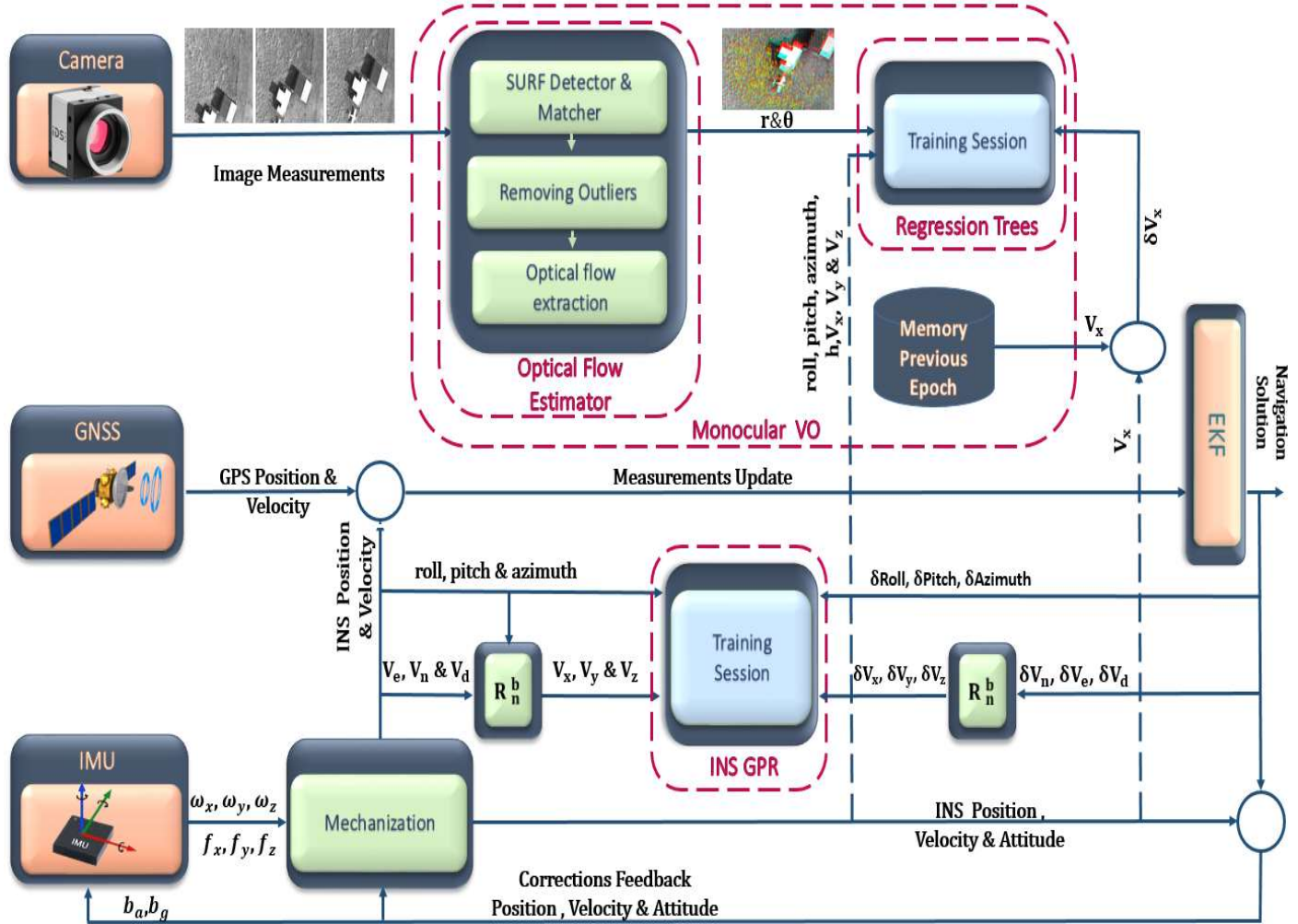


Figure 5-1: Illustrates the Smart Hybrid VAINS during the first phase.

5.2.2 Second Phase

During the second phase, the GNSS signal is still available, the monocular VO starts to predict the velocity component in the flight path direction. The INS drift predictor (GPR) predicts the velocity and orientation error states to correct the velocity and orientation drift exhibited by the inertial navigation solution. Although the GNSS signal is still available during this phase, both the

monocular VO and INS drift predictor operate in the prediction mode to simulate the same situation when the GNSS signal is lost. During the monocular VO prediction mode, the vehicle velocity component is obtained based on the extracted optical flow, the generated model during the training session and the last available measurements from the GNSS/INS integration. This predicted velocity increment is added to the last available velocity observation that obtained from the GNSS/INS integration to obtain the velocity component in the current epoch as follows:

$$V_{\text{visual odom}} = V_{\text{last GNSS/INS}} + \Delta V_{\text{prdicted Tree}} \quad (5-16)$$

The predicted velocity component in the flight direction obtained from the monocular VO is then fused with data from the on-board INS in an EKF [83]. This predicted velocity component in the flight direction from monocular VO is used as an input to train other GPR algorithm (monocular VO drift predictor). The difference between the velocity component in the flight direction obtained from the GNSS/INS integration and the same velocity component obtained from the monocular VO is used as an output to learn this GPR. In this phase, two separate EKFs are utilized. The first EKF is used for the GNSS/INS integration to obtain the vehicle navigation solution during this phase, use the difference between the estimated velocity component in the flight direction from GNSS/INS integration, and from the VO as outputs to train the monocular VO drift predictor (GPR). The second EKF is utilized to differentiate the monocular VO/INS integration from the GNSS/INS integration. The main reason for that is to obtain the monocular VO input states from the INS mechanization in standalone mode. Hence, the predicted monocular VO output is obtained based on the INS mechanization states in standalone mode during the availability of the GNSS measurements in this phase to simulate same scenario when the GNSS signal lost (phase three). Figures 5-2 illustrates the proposed system structure during the second phase. The INS drift

predictor (GPR) output is constrained by its predicted variance. The GPR correction is only applied if the GPR predicted variance for the velocity and orientation error states is less than the INS estimated variance. These constrained corrections have a significant impact on the enhancement of navigation solution since it ensures that only reliable corrections are applied (typically obtained using available training).

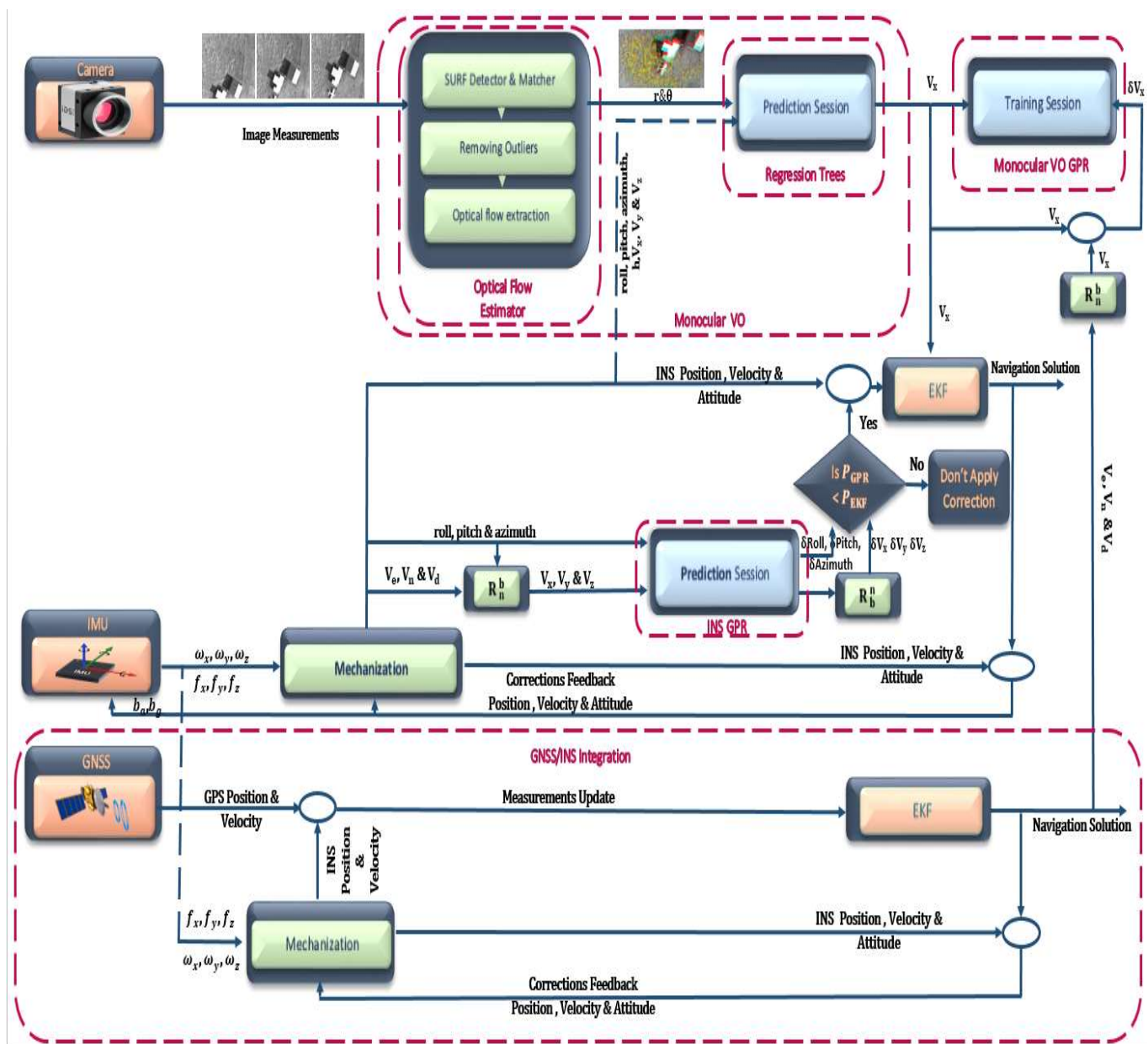


Figure 5-2: Illustrates the Smart Hybrid VAINS during the second phase.

5.2.3 Third Phase

The GNSS signal outage is considered to occur during the third phase. During this phase, the monocular VO drift predictor (GPR) starts to predict the velocity difference in the flight direction between the ground truth and the monocular VO velocity. Then, this velocity difference is used to correct the velocity component in the flight direction obtained from the monocular VO, which will enhance the accuracy of the EKF velocity measurement update. The monocular VO drift predictor (GPR) output is also constrained by its predicted variance. The GPR correction is only applied if the GPR predicted variance for the velocity error state is less than the INS estimated variance.

Figures 5-3 illustrates the proposed system structure during the third phase.

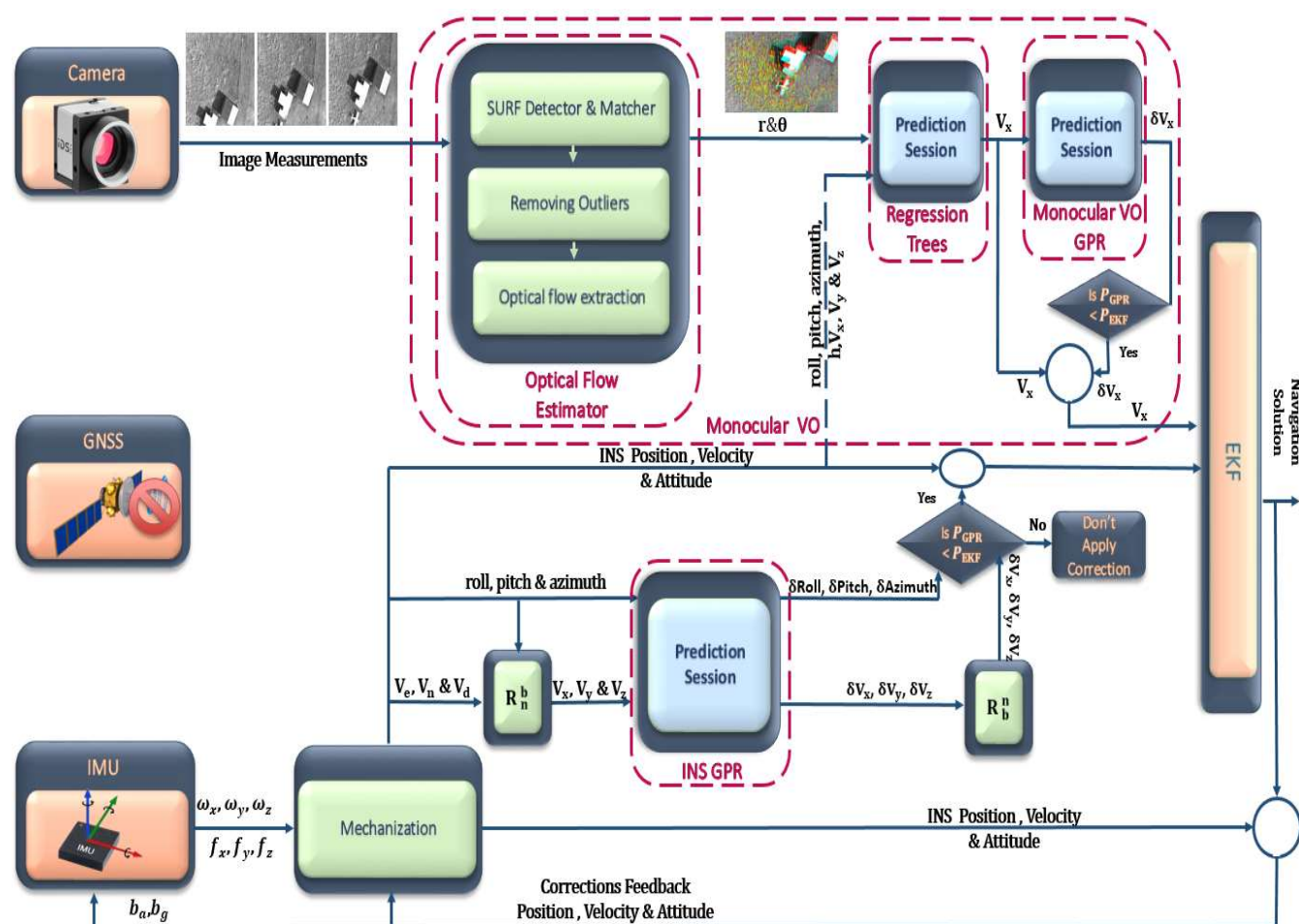


Figure 5-3: Illustrates the Smart Hybrid VAINS during the third phase.

5.3 Experimental Results

The proposed approach has been evaluated using a public dataset, which is collected by a fixed wing aircraft flown at Kagaru, Queensland, Australia on 31/08/10. This aircraft flew over a rural area and captured views of grass, roads, trees, parked aircraft, ponds and buildings. This UAV is equipped with XSens Mti-g INS/GNSS to offer the full navigation solution and Pt Grey Flea2 firewire camera with a resolution of 1280x960, 6mm focal length lenses and 30 frames per second to collect the visual information. These aerial images are obtained from one of the two downward facing cameras. Figure 5-4 illustrates the lack of the observed features problem while. Figure 5-5 shows the inconstant matches (outliers) between two successive frames issue.

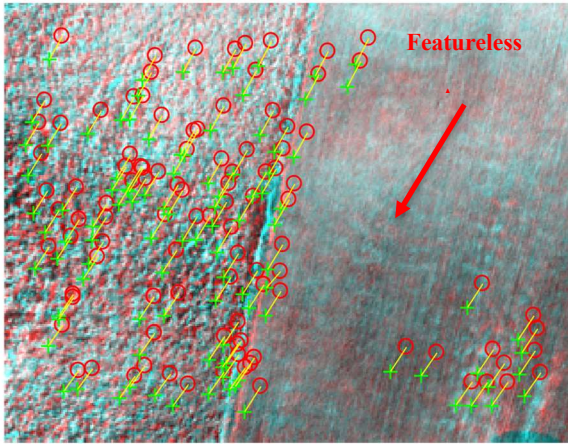


Figure 5-4: Lack of the observed features problem.

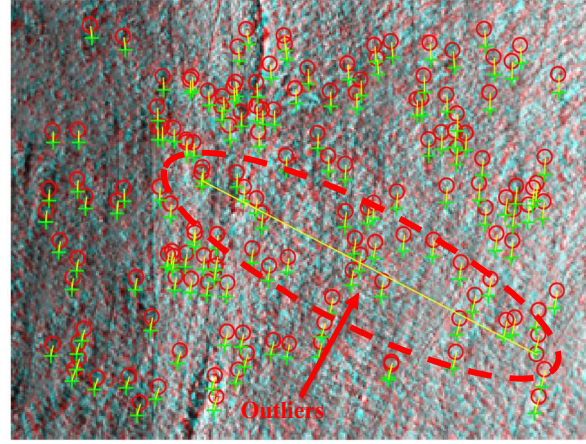


Figure 5-5: Inconstant matches between two successive frames.

Two simulated GNSS Signal outages scenarios are carried out for one-minute period. Each outage was at different trajectory parts with three experiments for each outage period to evaluate the effectiveness of the proposed algorithm in enhancing the 3D position accuracy during GNSS signal outages. Figure 5-6 shows the two-outage periods along the UAV flight trajectory. Figure 5-7

shows the three performed experiments along each outage period. Notably, the proposed algorithm achieved better localization accuracy than the monocular VO aided INS in [80].

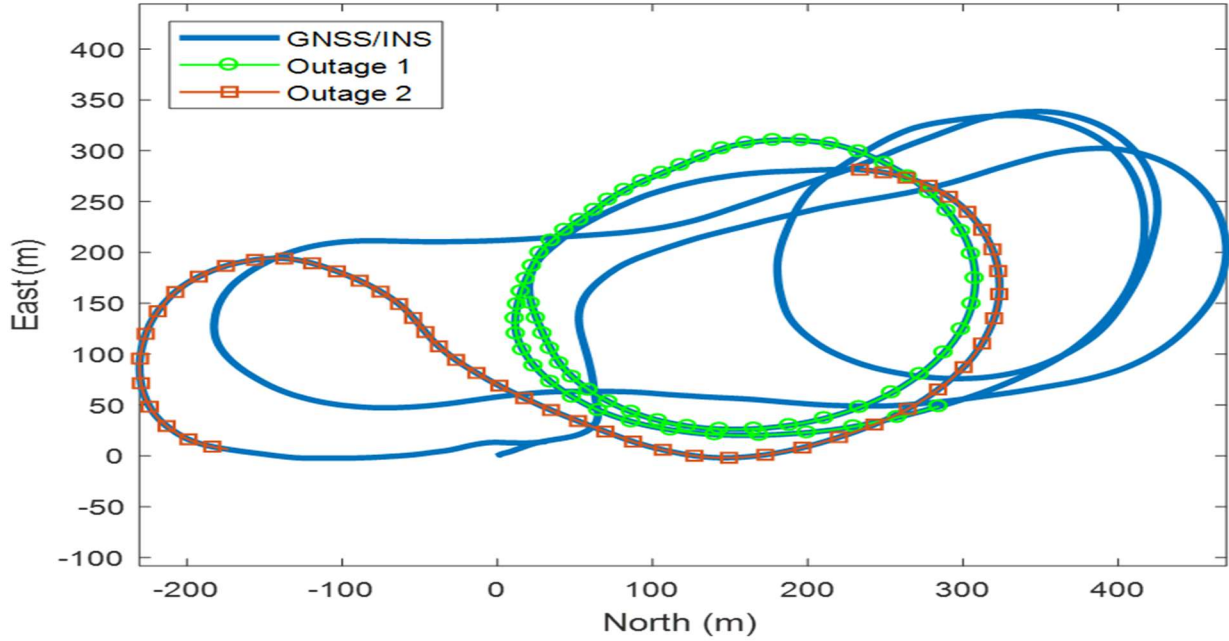


Figure 5-6: Two-outage periods along the UAV flight trajectory.

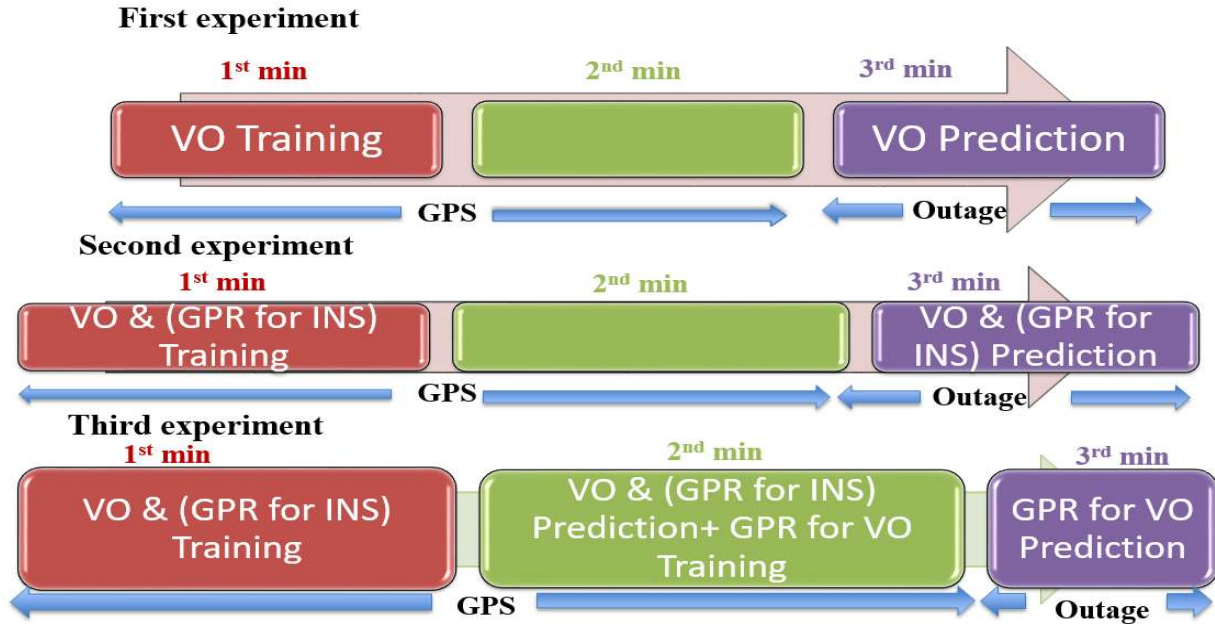


Figure 5-7: Three- experiments that performed along each outage period (VO/INS integration – VO/ (INS with GPR correction) integration - Smart Hybrid VAINS).

5.3.1 First Artificial Outage

Figure 5-8 shows a comparison between the estimated 2D flight trajectory outage segments from the GNSS/INS integration (ground truth segment), VO/ INS integration, VO/ INS with GPR correction integration, and Smart Hybrid VAINS. The standard division of the estimated forward velocity is 0.15.

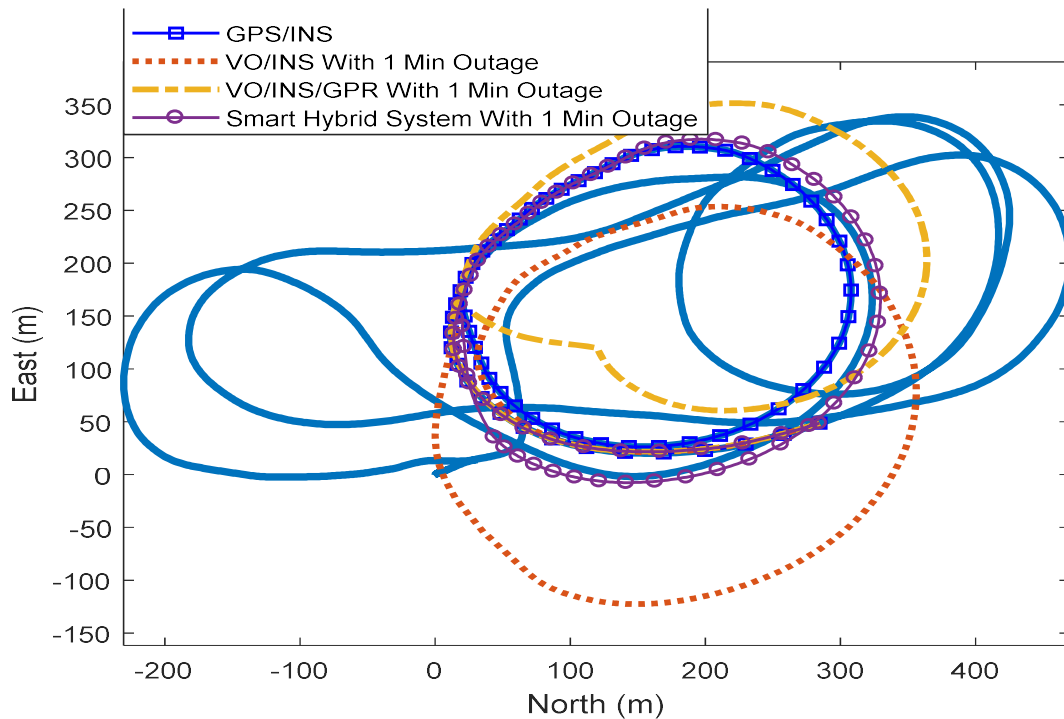


Figure 5-8: Estimated 2 D flight trajectory using INS/GNSS integration without GNSS outage, VO/INS integration, (VO/INS with GPR correction) integration and Smart Hybrid VAINS during the GNSS outage period.

Figures 5-9, 5-10 and 5-11 illustrate a comparison between (North, East and Height) position values obtained from (INS) in standalone mode, VO/INS integration, (VO/INS with GPR correction) integration, and Smart Hybrid VAINS during the GNSS outage period with the ground truth-value (GNSS/INS), respectively.

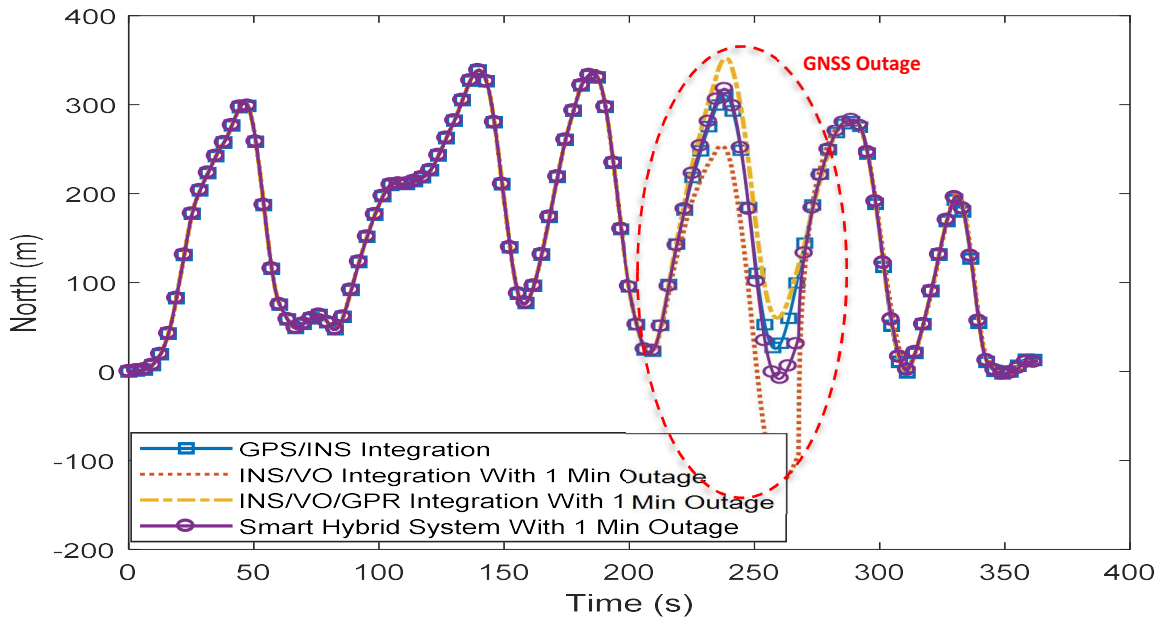


Figure 5-9: Comparison between (North) values obtained from VO/INS integration, (VO/INS with GPR correction) integration and Smart Hybrid VAINS during the GNSS outage period.

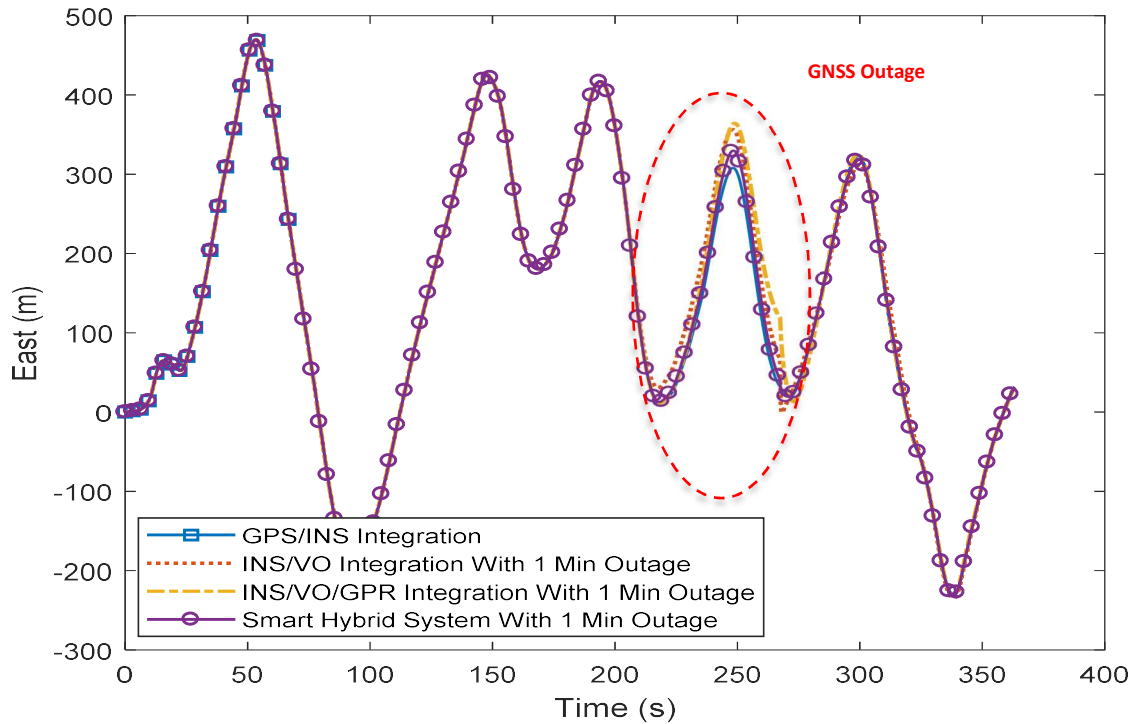


Figure 5-10: Comparison between (East) values obtained from VO/INS integration, (VO/INS with GPR correction) integration and Smart Hybrid VAINS during the GNSS outage period.

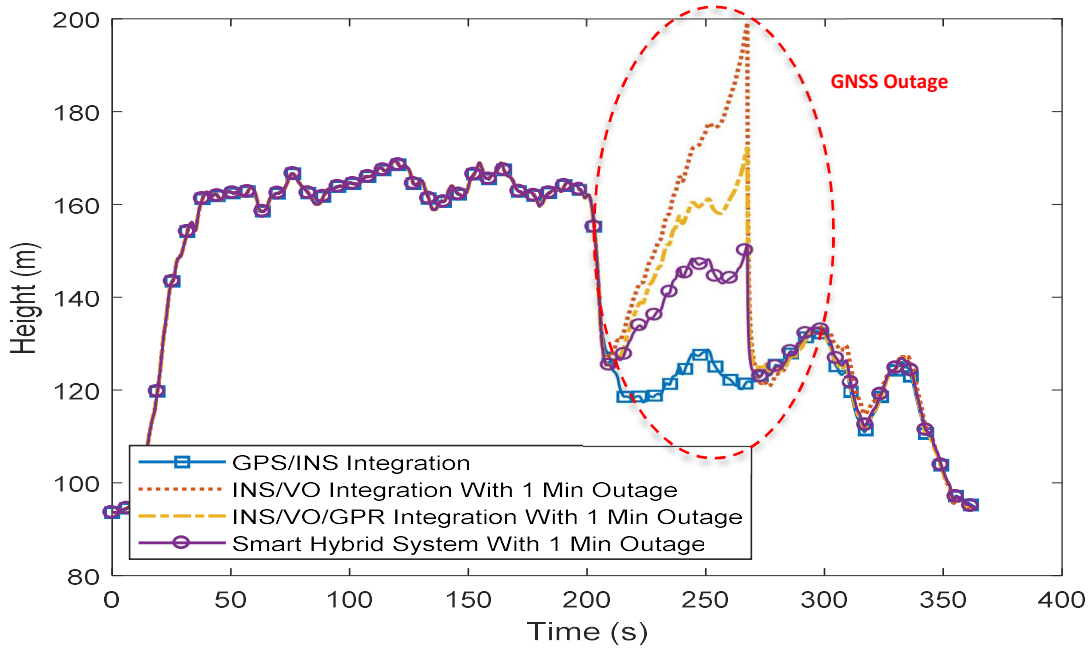


Figure 5-11: Comparison between (Height) values obtained from VO/INS integration, (VO/INS with GPR correction) integration and Smart Hybrid VAINS during the GNSS outage period

The results clearly indicate that the smart hybrid VAINS can aid the INS during a short GNSS signal outage. It also demonstrates its capability in reducing the 3D RMS positioning errors to 29.5% and %58.9 of the VO/INS integration, and VO/INS with GPR correction integration respectively over a one minute of GNSS signals outage.

5.3.2 Second Artificial Outage

Figures 5-12 illustrates a comparison between the estimated 2D flight trajectory outage segments obtained from the GNSS/INS integration (ground truth segment), VO/ INS integration, VO/ INS with GPR correction integration, and Smart Hybrid VAINS. Figures 5-13, 5-14 and 5-15 illustrate a comparison between (North, East and Height) position values obtained from VO/INS integration, VO/INS with GPR correction integration, and Smart Hybrid VAINS during the GNSS outage period with the ground truth-value (GNSS/INS), respectively. The standard division of the estimated forward velocity is 0.15 m/s.

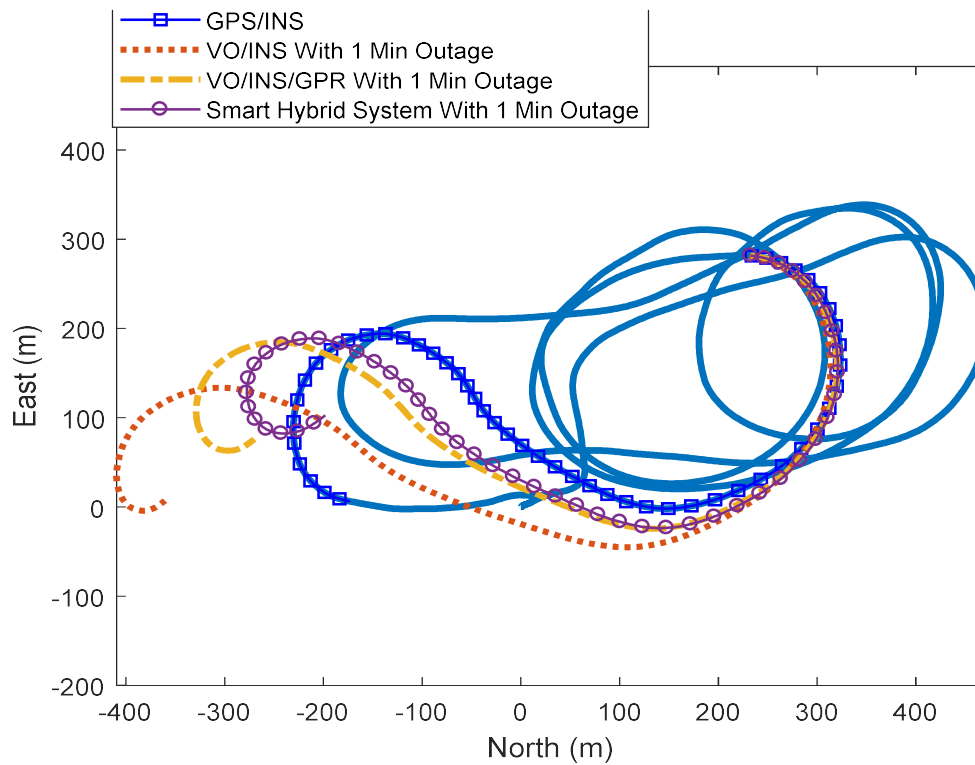


Figure 5-12: Estimated 2 D flight trajectory using INS/GNSS integration without GNSS outage, INS in standalone mode, VO/INS integration, (VO/INS with GPR correction) integration and Smart Hybrid VAINS during the GNSS outage period.

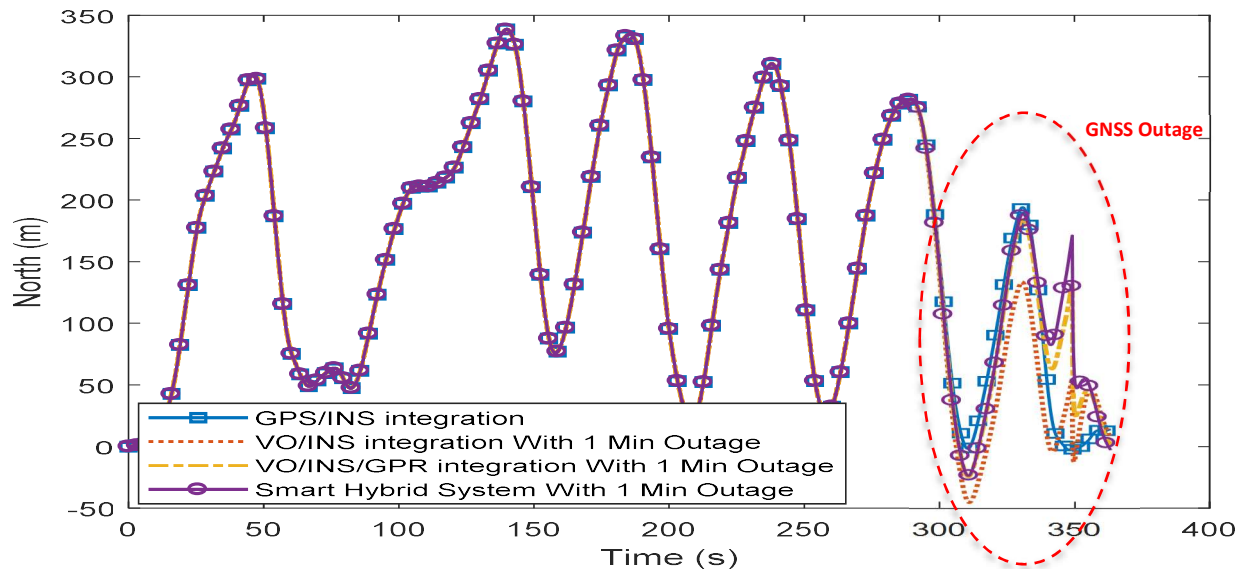


Figure 5-13: Comparison between (North) values obtained from VO/INS integration, (VO/INS with GPR correction) integration and Smart Hybrid VAINS during the GNSS outage period.

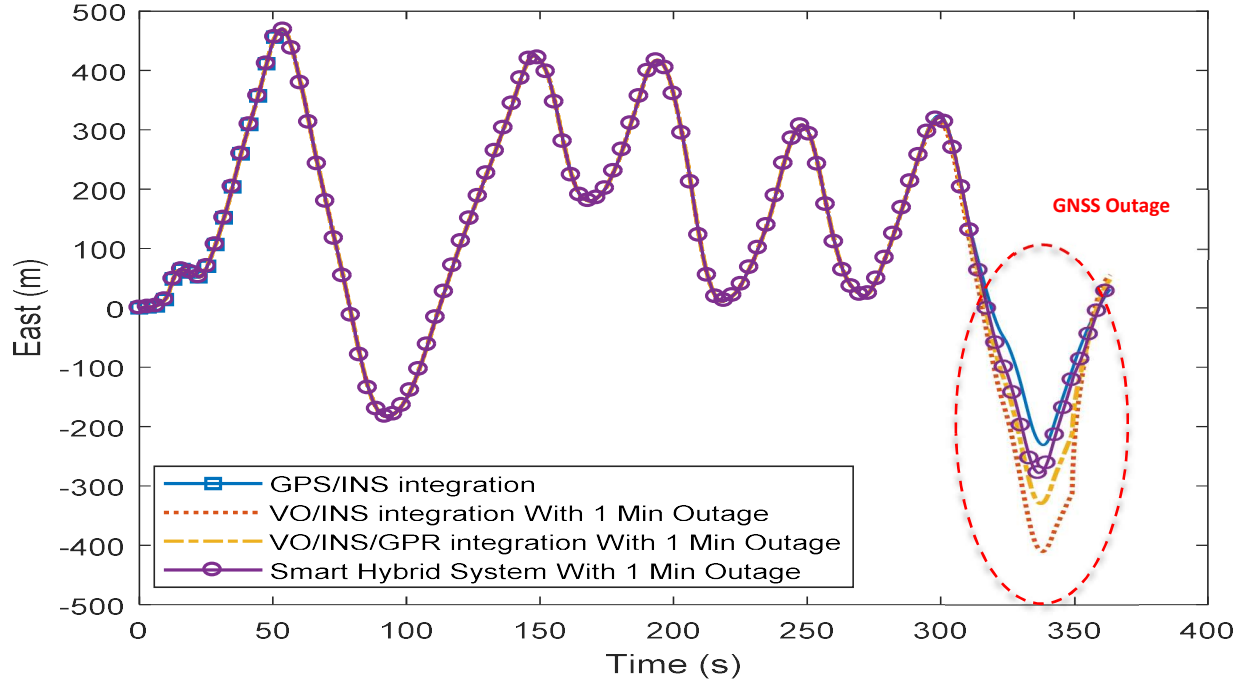


Figure 5-14: Comparison between (East) values obtained from VO/INS integration, (VO/INS with GPR correction) integration and Smart Hybrid VAINS during the GNSS outage period.

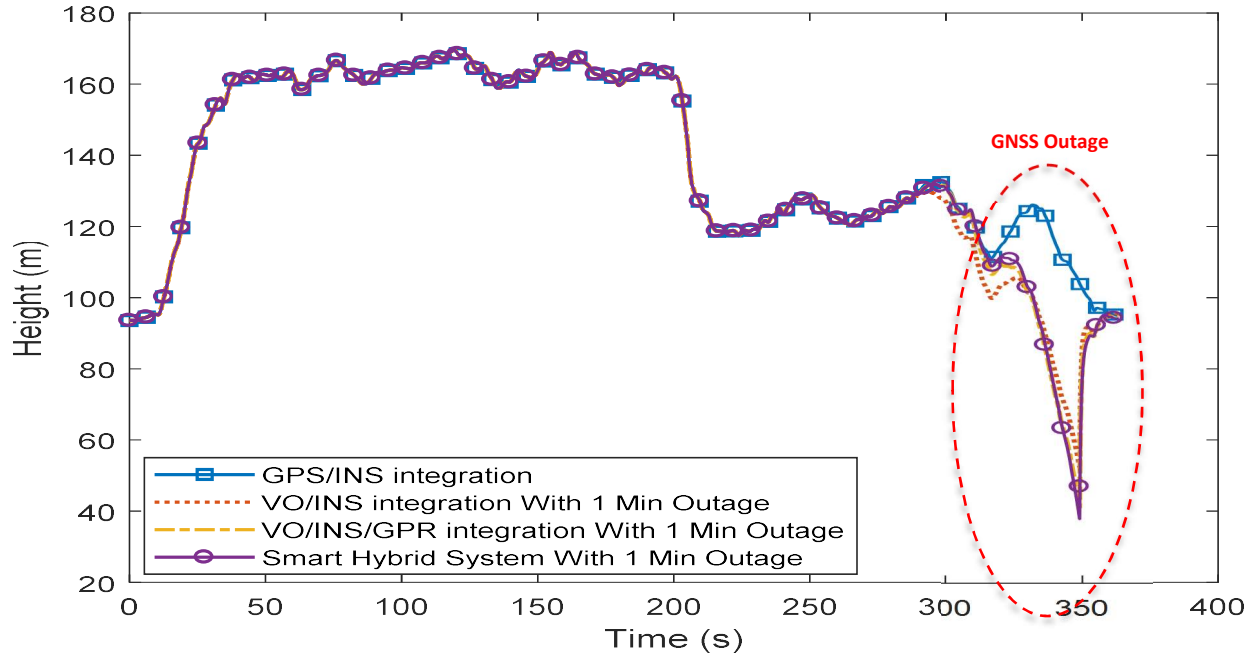


Figure 5-15: Comparison between (Height) values obtained from VO/INS integration, (VO/INS with GPR correction) integration and Smart Hybrid VAINS during the GNSS outage period.

The results demonstrate the ability of the proposed smart hybrid VAINS in aiding the INS during short GNSS signal outages. It also shows its capability in reducing the 3D RMS positioning errors to 47.6% and 76.3% of the VO/INS integration, and (VO/INS with GPR correction) integration, respectively over a one minute of GNSS signals outage. The following table provides a comparison of the RMS errors values for the position states obtained from VO/INS integration, VO/INS with GPR correction integration, and smart hybrid VAINS during the GNSS outage period with the ground truth-values. The proposed smart hybrid VAINS technique reduced the 3D average positioning errors for the two outages periods to 38.5%, and 67.6% of the VO/INS integration, and (VO/INS with GPR correction) integration, respectively.

Table 5-1: Comparison between (RMS Errors) values for the position states that obtained from (INS) and (INS with GPR).

	Symbol	First Outage	Second Outage
North Error (m)			
	VO/INS	38.1	18.4
	VO/INS with GPR	12.5	15.8
	Smart Hybrid VAINS	9.3	19.4
East Error (m)			
	VO/INS Error	16	49.5
	VO/INS with GPR	18.2	27.7
	Smart Hybrid VAINS	5.7	14.1
Height Error (m)			
	VO/INS	17.2	9.2
	VO/INS with GPR	12.1	10.1
	Smart Hybrid VAINS	7.5	8.9
3D Position Error (m)			
	VO/INS	44.7	53.6
	VO/INS with GPR	22.4	33.4
	Smart Hybrid VAINS	13.2	25.5
Enhancement Percentage From VO/INS%			
	Smart Hybrid VAINS	70.5	52.4
Enhancement Percentage From VO/INS with GPR %			
	Smart Hybrid VAINS	41.1	23.7

5.4 Summary

A Smart Hybrid VAINS-based approach was proposed to enhance the positioning accuracy and reliability of the molecular VO aided INS algorithm [79] during GNSS outage periods. This VAINS algorithm is affected by the IMU biases and lack of the observed features or inconstant matches. The proposed system can reduce such effects on the performance by modeling the main trend for different drift errors (monocular VO drift and INS drift) when the GNSS measurements

are available and predicting those errors during the GNSS signal outage. The proposed system is divided to three main modes of operation as follow:

1-The first phase is a training phase for the monocular VO and the INS drift predictor when the GNSS signal is available.

2-The second phase is a prediction phase for the monocular VO and the INS drift predictor when the GNSS signal is available. To properly model the monocular VO drift error behavior as same as the situation when the GNSS signal is lost, two separate EKFs are used to fuse the GNSS/INS and monocular VO/INS, respectively. This phase is also a training phase for the monocular VO drift predictor. The predicted velocity in the flight direction obtained from the VO is used as training input and the difference between the ground truth forward velocity obtained from GNSS/INS integration and the predicted velocity from VO is used as output for this monocular VO drift predictor.

3- The third phase is a prediction phase for the monocular VO, INS drift predictor, and monocular VO drift predictor when the GNSS signal is lost.

The proposed system is evaluated through two outage periods. To assess the proposed system performance, four experiments were performed in each outage period as follow:

1-The INS was tested in standalone mode for one minute of GNSS signals outage.

2- The monocular VO/INS integration (VAINS) was tested for one minute of GNSS signals outage. The VO was trained for one minute when the GNSS signal is available. The VO starts to

predict after one minute from the training session and the VO/INS integration is assessed in the third minute (GNSS signal outage). This experiment is illustrated in the first row of Figures 5-5.

3- The monocular VO/INS integration enhanced with the INS drift predictor was tested for one minute of GNSS signals outage. The VO and INS drift predictor were trained during the first minute when the GNSS signal is available. The VO and INS GPR started to predict in the second minute and assessed in the third minute (GNSS signal outage). This experiment is illustrated in the second row of Figures 5-5.

4- The smart hybrid VAINS was tested for one minute of GNSS signals outage. The VO and INS GPR were trained during the first minute when the GNSS signal is available. The VO and INS GPR started to predict in the second minute and the VO GPR was trained during this minute when the GNSS signal is still available. The monocular GPR started to predict during the third minute. This experiment is illustrated in the third row of Figures 5-5.

An airborne dataset is used to assess the proposed system performance. The experiments results demonstrated the ability of smart hybrid VAINS for enhancing the average 3D RMS positioning errors to 61.5%, and 32.4% of monocular VO/INS integration, and monocular VO/INS integration enhanced with the INS drift predictor during the GNSS signal outage even with a short learning period, respectively. In addition, the experiments illustrate the ability of Smart Hybrid VAINS to reduce the effect of the problems associated with VAINS in [80].

Chapter Six: **Lightweight FMCW Radar Odometry Aided**

Navigation for UAVs in GNSS Denied Environment

Navigation in GNSS-denied environment forms a serious challenge for UAVs while performing their missions. A variety of VO based approaches are proposed as a GNSS denied environment navigation systems. Although onboard cameras have small size, light weight, low power consumption and ability to provide useful measurements in term of color and texture that can be used to enhance the navigation solution during the GNSS outages periods, their imagery measurements are affected by brightness, lighting conditions and featureless areas. Therefore, a FMCW RO based approach is proposed for enhancing the 3D positioning accuracy of UAVs in GNSS denied environments. This radar is cable of avoiding the visual sensors limitations since it is immune to the environmental changes such as illumination, rain, fog, dust, and featureless areas. In addition, it has a light weight, small size and low power consumption which make it more appealing for many mobile mapping and navigation applications mounted on small UAVs.

The main contributions of the proposed system are its ability to accurately detect the forward vehicle speed based on adaptive thresholding target detection technique to identify the main ground target and avoid the clutters. While many of the proposed RO solutions assume different assumptions about the vehicle navigation states, the proposed solution does not make such assumptions and provides a generic enhancement to the navigation solution under the typical maneuvering scenarios. In addition, the proposed algorithm has a real-time performance since the target detection processing time is around 1 ms. Unlike other radar aided navigation systems that rely on artificial reflectors even for detecting or tracking the targets, the proposed RO benefits from ground scatterers such as grass, trees or any other objects in the surrounding environment, to

aid the navigation during the GNSS signal outage. Finally, the results of this system demonstrate the system's ability to mitigating the low cost MMES MPU-6000 IMU drift errors in a real flight data. The positioning accuracy of previous RO research works in [67], [68] are 135 meters in 1 minute, and 92 meters in 1 minute respectively. The proposed RO approach is tested for 2 minutes of GNSS signal outage period during two-real flights with 3D positioning errors up to 8.15 meters.

6.1 Overview of the Integrated Navigational System

A RO aided navigation system is proposed to enhance the positioning reliability and accuracy during the GNSS signal outage. This system fuses the estimated forward velocity component in the body frame, which is obtained from the RO with the IMU, barometer, and magnetometer measurements via an EKF. The barometer and magnetometer are utilized as additional aiding sensors since they are typically mounted on the utilized UAV. Figure 6-1 illustrates the proposed system architecture. The proposed system is divided to three main steps as follows:

- Radar Data Acquisition
- Targets Detection and Velocity Extraction
- RO/INS/ Magnetometer/ Barometer Fusion Using EKF

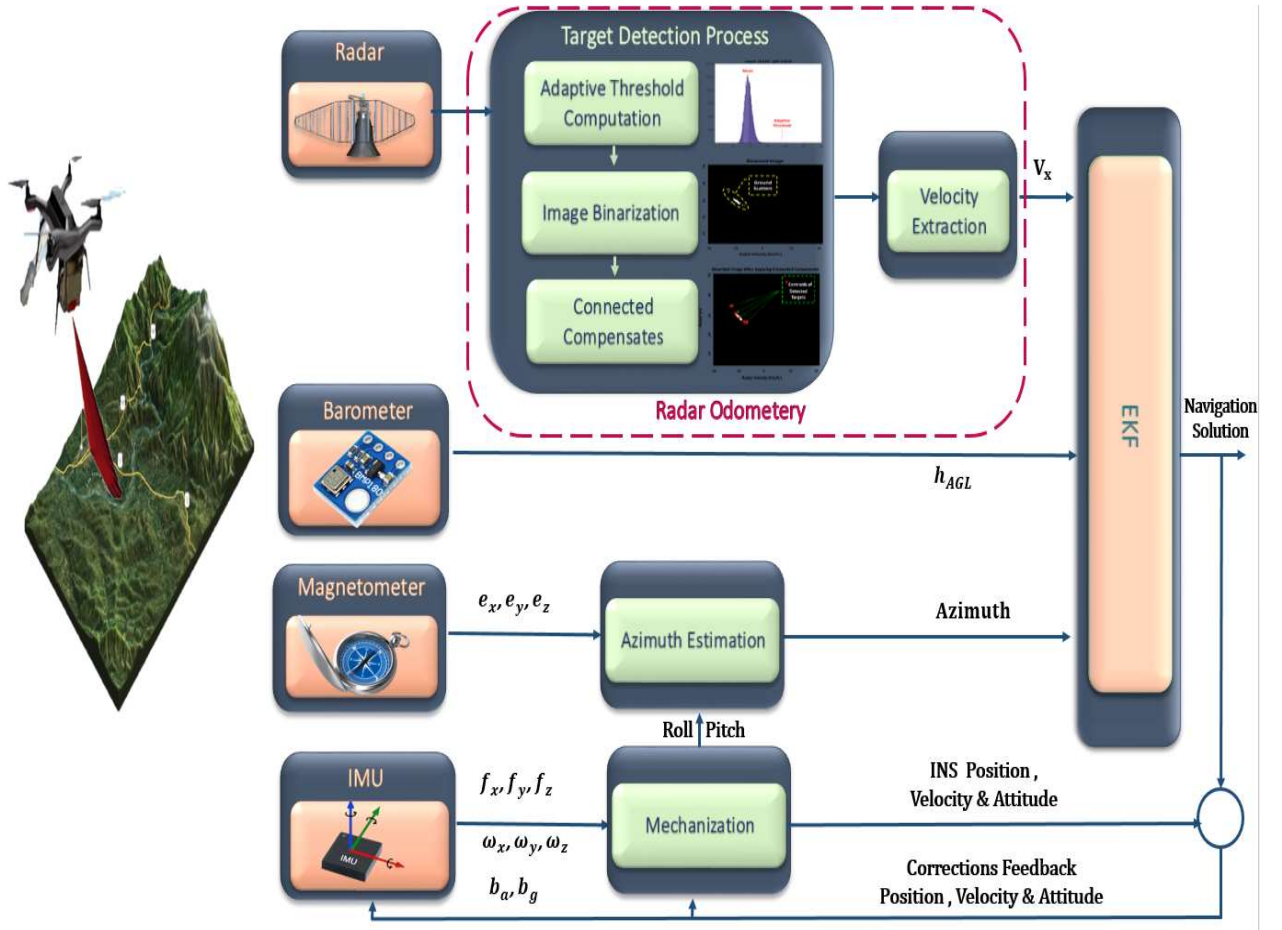


Figure 6-1: RO aided navigation system block diagram.

6.1.1 Radar Data Acquisition

The proposed system is based on acquiring the range and velocity measurements from a micro FMCW radar after performing internal radar signal processing. While the vehicle is flying in unknown environment, the radar is continuously transmitting a frequency modulated sawtooth shaped frequency shift chirps $f_{RF\ TX}$ toward the ground objects as follows:

$$f_{RF\ TX} = f_0 + K_f * t, 0 \leq t < T \quad (6-1)$$

Where f_0 is the initial transmitted frequency, K_f is the sweep rate, T is the frequency sweep time.

The frequency sweep rate (K_f) is obtained from:

$$K_f = \frac{BW}{T} \quad (6-2)$$

Where BW is the transmitted chirp signal bandwidth. Due to the traveling distance to the scatterers and back toward the radar's receiving antennas, there is a round trip propagation time delay Δt and a small frequency shift Δf between the two-radio frequency (RF) signals. These time and frequency delays occur due to the range propagation effect. The time delay between the transmitted and received signals for each i reflector is:

$$\Delta t = 2 \frac{r_i}{c_{\text{light}}} \quad (6-3)$$

Parameter r_i is the range between the radar antenna and each scatterer inside the beam width of the radar, and c_{light} is the speed of light. The received signal frequency is shifted by the time delay Δt as:

$$f_{RF\ RX} = f_0 + K_f * (t - \Delta t) , \Delta t \leq t < T + \Delta t \quad (6-4)$$

The received signal is then mixed by the original transmitted signal and passed through low pass filter to obtain the video signal $x(t)$ that has a low differential frequency or Beat frequency f_b as follows:

$$f_b = K_f * \Delta t \quad (6-5)$$

By substituting Equation (6-4) in Equation (6-5), Δf can be rewritten as:

$$f_b = \frac{BW}{T} * 2 \frac{r_i}{c} \quad (6-6)$$

The Doppler frequency f_{doppler} is then extracted from the phase changes of this signal. The f_{doppler} helps to estimate the object velocity. The radar range and velocity measurements are

obtained for different scatterers by applying two-dimensional signal processing to the sampled video signal. More details on this process can be found in [86]. The utilized radar has 12.150 kHz repetition rate for the transmitted chirps. In each chirp, 256 sampling points are taken with a sample rate of 264 ns. After applying the Fast Fourier Transform (FFT) for the sampled signals which has been received through three receiving antennas, a mean Range-Doppler Map (RDM) is generated that has 256x256 pixels with 32 Bit amplitude value for each pixel by averaging the RDM from all antennas. Figure 6-2 illustrates an RDM image where the X-axis represents the speed measurements while the Y-axis provides the range measurements. The 32-Bit amplitude value at each pixel represents the echo strength for the received signals from different ground scatterers.

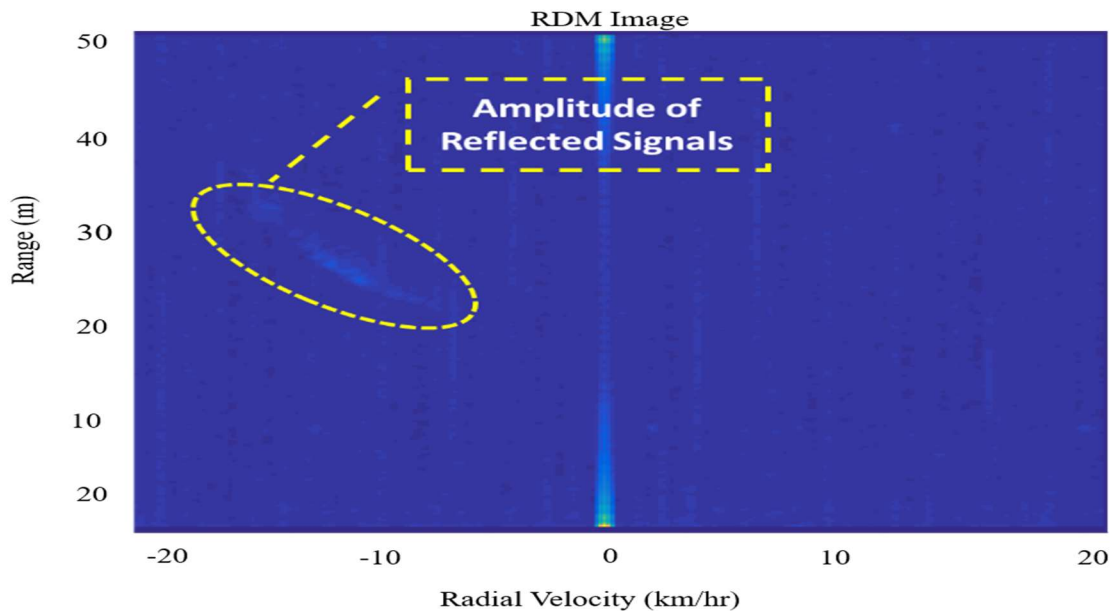


Figure 6-2: Reflected ground signals in the RDM image.

This map is acquired through an Ethernet cable from the radar after performing the aforementioned signal processing inside the radar. This constructed map is then utilized for the target detection and velocity extraction purpose.

6.1.2 Targets Detection and Velocity Extraction

Constant False Alarm Rate (CFAR) is typically utilized for radar target detection, which attempts to extract distinctive information from the cluttered background of the received signals.

The role of operation for the CFAR is to adaptively estimate the threshold power level and declare the target detection when the returned echo signal exceeds this threshold. This detection process is achieved by locally comparing the power for the cell-under-test (CUT) against its neighborhood cells (background). Different CFAR approaches can be used for target detection such as cell averaging (CA), greatest-of cell averaging (GOCA), or smallest-of cell averaging (SOCA) and ordered statistics CFAR (OS-CFAR) [24], [87]. Although the CFAR is an effective detection approach for many applications such as detection of aerial targets using ground radar stations and airborne radars, this detector is not convenient for the proposed system since the ground scatterers approximately have the same power level on the RDM. The CFAR-detected targets for the RDM image is shown in Figure 6-3 where the CFAR could detect a part of the main reflected arc of the ground objects while it is missing the rest of it.

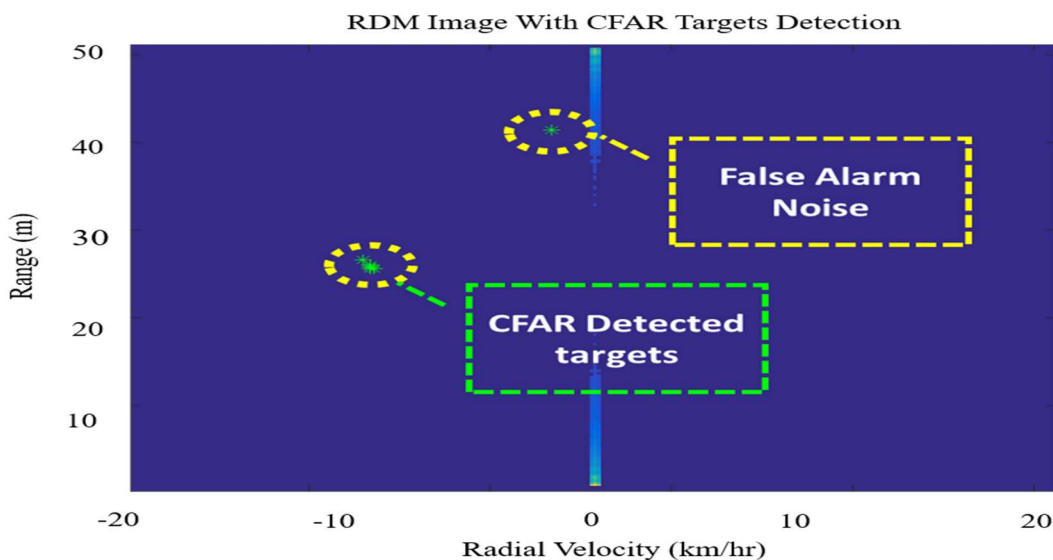


Figure 6-3: CFAR detected targets in the RDM image.

CFAR also detected a false target (noise) which has a prominent power level from its background. The first problem occurs when estimating the power level of the CUT from its surrounding background inside a patched area of real ground scatters. In this case, the CFAR could not detect all targets because the CUT has the same power level as its neighborhood which makes it not distinctive. The second issue results from random noises which have relatively high-power level compared to its local neighborhood cells.

Unlike the CFAR, which depends on the local neighborhood cells for target detection, an alternative adaptive global thresholding technique has been proposed to avoid the CFAR associated problems. This scheme globally computes a histogram for the whole RDM image to be used for threshold level estimation at each epoch. This adaptive threshold is obtained based on a certain confidence level from the mean value of its distribution. This confidence level is picked to be seven times the histogram standard deviation, which ensures the distinction of any strong ground scatters above this threshold from the cluttered or noisy image background as shown in Figure 6-4.

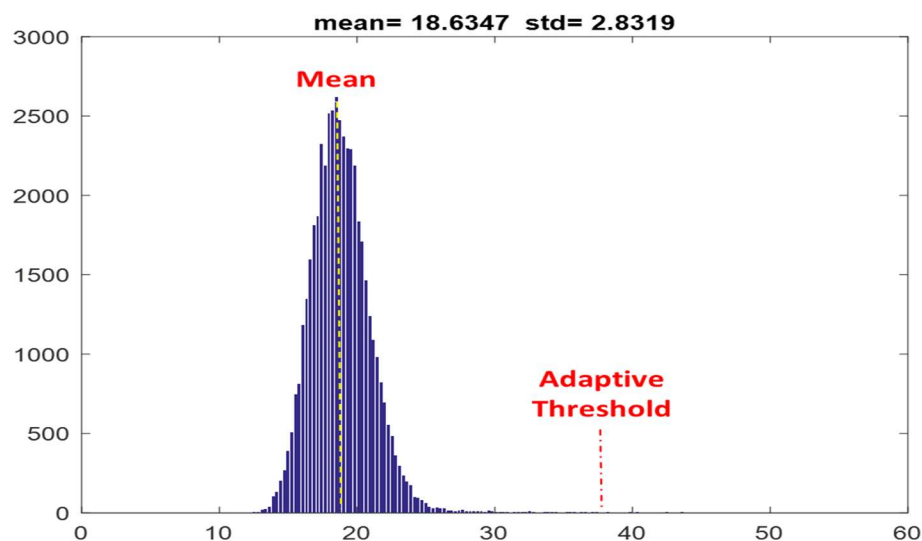


Figure 6-4: Histogram for the whole RDM.

A binary image is then created by replacing all pixel values above this adaptive threshold with 1s and setting all the remaining values to 0s as illustrated in Figure 6-5.

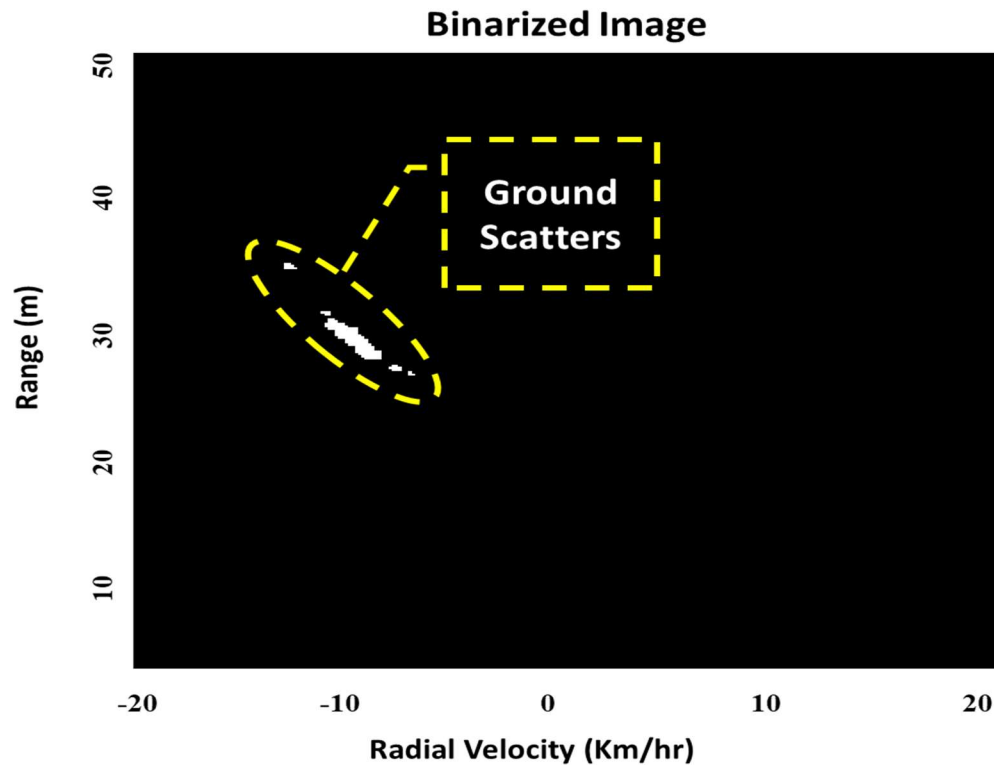


Figure 6-5: Binarized RDM image by utilizing the computed threshold.

A connected component-based approach is then applied to this binary image to gather neighbor pixels with values of 1 into one region. After forming these regions as shown in Figure 6-6, the centroid of each region is obtained by averaging its neighborhood pixels in X and Y directions. The radial velocity for each detected target can be acquired directly from the X-axis of this binarized image. These radial velocities are then projected by the radar tilting angles which is 60 degrees toward the flight path direction. The areas of detected targets in the image are used to exponentially weight the targets velocities. The output of this averaging process is the resultant forward velocity of the vehicle in the body frame.

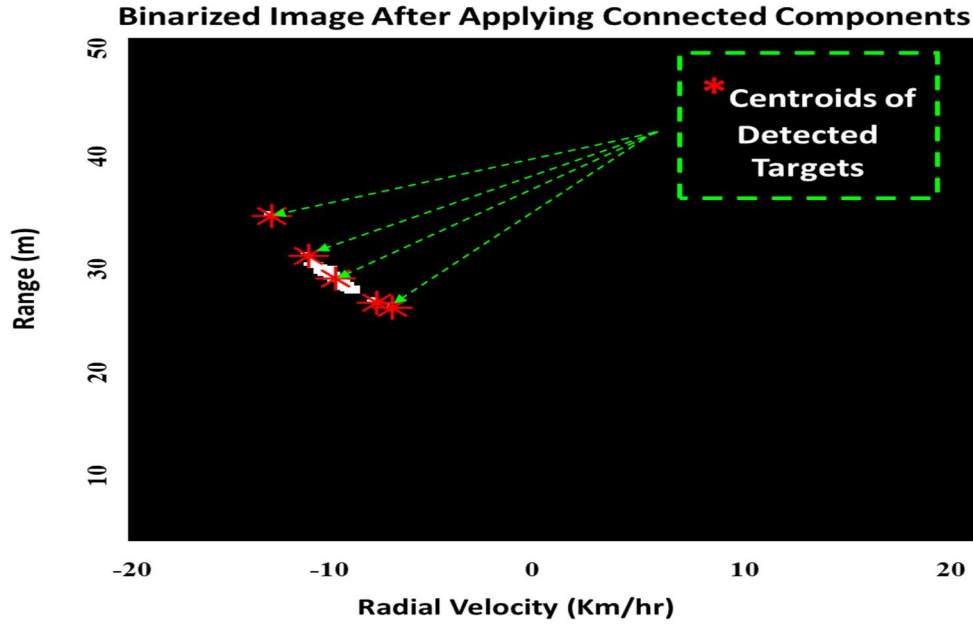


Figure 6-6: Detected targets based on connected components approach.

6.1.3 RO/INS/Magnetometer/ Barometer Fusion Using EKF

This section describes the data fusion between INS, magnetometer, barometer, and RO measurements and GNSS during its availability in an EKF. The navigation states which are position, velocity, and attitudes in the navigation frame (n-frame) are derived from the IMU raw measurements through a mechanization process. The EKF error states vector are 21 states, as follows:

$$\mathbf{x} = [\delta \mathbf{r}^n_{1 \times 3} \quad \delta \mathbf{v}^n_{1 \times 3} \quad \boldsymbol{\varepsilon}^n_{1 \times 3} \quad \mathbf{b}_{1 \times 3} \quad \mathbf{d}_{1 \times 3} \quad \mathbf{s}_a_{1 \times 3} \quad \mathbf{s}_g_{1 \times 3}] \quad (6-7)$$

Where $\delta \mathbf{r}^n, \delta \mathbf{v}^n, \boldsymbol{\varepsilon}^n$ are the (position, velocity and attitude) error vector of INS mechanization respectively and \mathbf{b}, \mathbf{d} are the accelerometers bias and gyros drift respectively. Finally, \mathbf{s}_a and \mathbf{s}_g are the accelerometers and gyros scale factor. The whole sensors are fused in loosely coupled

fashion through two main steps inside the EKF, which are, prediction phase, and measurements update phase.

6.1.3.1 Prediction Model

The system model, which describes how different INS error states evolve with time, is obtained by linearly perturbing the mechanization equations and can be represented as follows:

$$\hat{x}_{k+1}^- = \Phi_k \hat{x}_k + G_k w_k \quad (6-8)$$

Where Φ_k is the state transition matrix, x_k is the error states, G_k is the noise coefficient matrix and w_k is the system noise. The inertial sensor stochastic errors are modeled as a first order Gauss-Markov process. The prediction of state-error covariance matrix P_k at a certain epoch is:

$$P_{k+1}^- = \Phi_k P_k \Phi_k^T + \bar{G}_k Q_k \bar{G}_k^T \quad (6-9)$$

Where Q_k is the covariance matrix of the system noise.

6.1.3.2 Sensors Measurements

While the GNSS signal is available, its positioning measurements P_{GNSS}^{ned} in the navigation frame are utilized to update the predicted INS states. The North–East–Down GNSS position can be written as:

$$P_{GNSS}^{ned} = [P_{n,GNSS} \quad P_{e,GNSS} \quad h_{GNSS}] \quad (6-10)$$

Where $P_{n,GNSS}$ is the North position, $P_{e,GNSS}$ is the East position and $h_{MSL,GNSS}$ is the ellipsoidal height.

The barometer is utilized to provide height update h_{baro} while the heading update ψ_{mag} is acquired from the magnetometer raw measurements (3D-magnetic field components) as:

$$\psi_{\text{mag}} = \tan^{-1} \left(\frac{-M_y \cos \Phi + M_z \sin \Phi}{M_x \cos \theta + (M_y \sin \Phi + M_z \cos \Phi) \sin \theta} \right) + \delta_{\text{mag}} \quad (6-11)$$

Where $[M_x \ M_y \ M_z]$ are the unit-vector measurements of magnetic north in body frame, Φ is the roll angle, θ is the pitch angle, and δ_{mag} is the magnetic declination, which is the bearing difference between true north and magnetic north. Finally, the estimated velocity in the flight path direction from the RO (V_{RO}) is utilized as velocity update during the GNSS signal outage.

6.1.3.3 Observation Model

The differences between the GNSS positioning measurements and the INS positioning measurements in the navigation frame are utilized as measurement updates to the EKF. The computed positions of the GNSS antenna center from the center of the IMU in the navigation frame can be written as

$$\hat{\mathbf{P}}_{\text{GNSS}}^{\text{ned}} = \mathbf{P}_{\text{GNSS}}^{\text{ned}} + \mathbf{D}^{-1} \delta \mathbf{P}_{\text{IMU}}^{\text{ned}} + \mathbf{D}^{-1} (\mathbf{C}_{\text{b}}^{\text{l}} l_{\text{GNSS}}^{\text{b}} \times) \boldsymbol{\phi} \quad (6-12)$$

Where $\hat{\mathbf{P}}_{\text{GNSS}}^{\text{ned}}$ and $\hat{\mathbf{P}}_{\text{IMU}}^{\text{ned}}$ are the computed positions of the GNSS antenna center and the center of the IMU in the navigation frame respectively, $l_{\text{GNSS}}^{\text{b}}$ is the lever-arm between the GNSS antenna and the IMU in the body frame, $\mathbf{C}_{\text{b}}^{\text{l}}$ is the rotation matrix between the body and local level frame and $\boldsymbol{\phi}$ is the attitude errors which can be expressed in skew symmetric E^{ned} (or cross product $\boldsymbol{\phi} \times$) form as:

$$E^{\text{ned}} = \boldsymbol{\phi} \times = \begin{bmatrix} 0 & -\epsilon_d & \epsilon_e \\ \epsilon_d & 0 & -\epsilon_n \\ -\epsilon_e & \epsilon_n & 0 \end{bmatrix} \quad (6-13)$$

Where ϵ_n, ϵ_e and ϵ_d are the attitude errors in North–East–Down directions. The measured position by the GNSS can be written as

$$\tilde{P}_{GNSS}^{ned} = P_{GNSS}^{ned} + D^{-1} e_p \quad (6-14)$$

Where e_p is the GNSS position measurement error. From Equation 6-12 and Equation 6-14 the positioning measurements used for updating the EKF are:

$$\begin{aligned} z_{GNSS} &= D(\hat{P}_{GNSS}^{ned} - \tilde{P}_{GNSS}^{ned}) \\ &= \delta P_{IMU}^{ned} + (C_b^l l_{GNSS}^b \times) \phi - e_p \\ &= [I_{3 \times 3} : 0_{3 \times 3} : C_b^l l_{GNSS}^b : 0_{3 \times 12}] x - e_p \end{aligned} \quad (6-15)$$

From Equation 6-15 the design matrix can be expressed as:

$$H_{GNSS} = [I_{3 \times 3} : 0_{3 \times 3} : C_b^l l_{GNSS}^b : 0_{3 \times 12}] \quad (6-16)$$

Finally, the innovation sequence between the measurement updates z_{GNSS} and the estimated measurements \hat{z}_{GNSS} is obtained as:

$$\begin{aligned} \delta z_{GNSS} &= z_{GNSS} - \hat{z}_{GNSS} \\ &= z_{GNSS} - H_{GNSS} x \end{aligned} \quad (6-17)$$

The measured heading by the magnetometer can be written as:

$$\tilde{\psi}_{mag} = \psi_{mag} + e_{\psi_{mag}} \quad (6-18)$$

Where $e_{\psi_{mag}}$ is the magnetometer heading measurement error. The estimated Direction Cosine Matrix (DCM) \hat{C}_b^l which is derived from the mechanization process during the EKF prediction stage, is utilized to compute the heading angle $\hat{\psi}$.

The perturbation of this attitude DCM is expressed as:

$$\hat{C}_b^l = (I_{3 \times 3} - E^{ned})C_b^l \quad (6-19)$$

The misalignment between the vehicle body frame and the sensor frame (magnetometer) is calculated as follows:

$$\hat{C}_s^l = (C_b^s)^T \hat{C}_b^l \quad (6-20)$$

Where C_b^s is the rotation matrix between the body and sensor frame and \hat{C}_s^l is the rotation matrix between the sensor and local level frame. From Equation 6-19 and 6-20, the derived heading angle $\hat{\psi}$ can be obtained from this rotation matrix (\hat{C}_s^l) as:

$$\hat{\psi} = \tan^{-1} \left(\frac{\hat{C}_s^l(1,1)\epsilon_d + \hat{C}_s^l(2,1) - \hat{C}_s^l(3,1)\epsilon_n}{\hat{C}_s^l(1,1) - \hat{C}_s^l(2,1)\epsilon_d + \hat{C}_s^l(3,1)\epsilon_e} \right) \quad (6-21)$$

Where C_{ij} are the elements of the rotation matrix \hat{C}_s^l . The heading measurement used for updating the EKF, is the difference between the estimated heading from Equation 6-21 and the measured heading Equation 6-19 as:

$$z_{mag} = \hat{\psi} - \tilde{\psi}_{mag} \quad (6-22)$$

The error equation can be obtained by perturbing Equation 6-22 as:

$$\delta\psi = \frac{\partial \hat{\psi}}{\partial \epsilon_n} \epsilon_n + \frac{\partial \hat{\psi}}{\partial \epsilon_e} \epsilon_e + \frac{\partial \hat{\psi}}{\partial \epsilon_d} \epsilon_d \quad (6-23)$$

Hence, the design matrix can be expressed as:

$$H_{mag} = \left[0_{1 \times 6} : \frac{\partial \hat{\psi}}{\partial \epsilon_n} : \frac{\partial \hat{\psi}}{\partial \epsilon_e} : \frac{\partial \hat{\psi}}{\partial \epsilon_d} : 0_{1 \times 12} \right] \quad (6-24)$$

The innovation sequence between the measurements update z_{mag} and the estimated measurements \hat{z}_{mag} is obtained as:

$$\begin{aligned} \delta z_{mag} &= z_{mag} - \hat{z}_{mag} \\ &= z_{mag} - H_{mag} x \end{aligned} \quad (6-25)$$

The barometer is utilized to measure the height of the vehicle h_{baro} as:

$$\tilde{h}_{baro} = h_{baro} + e_{h_{baro}} \quad (6-26)$$

Where $e_{h_{baro}}$ is the barometer height measurement error. The offset between the earth surface and the mean sea level is then added to the barometer measured height as follows:

$$\tilde{h}_{MSL,baro} = \tilde{h}_{baro} + \text{offset} \quad (6-27)$$

The design matrix can be expressed as:

$$H_{baro} = \left[0_{1 \times 2} : 1 : 0_{1 \times 3} : C_b^l l_{GNSS}^b : 0_{1 \times 12} \right] \quad (6-28)$$

The innovation sequence between the measurements update z_{baro} and the estimated measurements \hat{z}_{baro} is obtained as:

$$\begin{aligned} \delta z_{baro} &= z_{baro} - \hat{z}_{baro} \\ &= z_{baro} - H_{baro} x \end{aligned} \quad (6-29)$$

The estimated velocity in the flight path direction, which is obtained from the RO can be written as:

$$\tilde{V}_{RO}^s = V_{RO}^s + e_v \quad (6-30)$$

Where V_{RO}^s is the velocity acquired from the RO represented in the sensor frame and e_v is the velocity measurement noise. The difference between the predicted forward velocity from the INS in the body frame and the extracted forward velocity from the RO is utilized as measurements update during the GNSS signal outage. Therefore, it is important to compensate for lever arm effect. Moreover, it is necessary to consider any misalignment between the vehicle body frame and the radar frame (sensor frame). The attitude errors and the angular rate errors must be incorporated to the derived velocity from the mechanization process. Hence, the relationship between the predicted velocity from the mechanization process \hat{V}_{IMU}^{ned} and the computed RO forward velocity \hat{V}_{RO}^s is:

$$\begin{aligned} \hat{V}_{RO}^s &= C_b^s \hat{C}_l^b \hat{V}_{IMU}^{ned} + C_b^s (\hat{\omega}_{nb}^b \times) l_{RO}^b \\ &\approx C_b^s C_l^b [I + (\phi \times)] (V_{IMU}^{ned} + \delta V_{IMU}^{ned}) + C_b^s (\omega_{nb}^b \times) l_{RO}^b + C_b^s (\delta \omega_{ib}^b \times) l_{RO}^b \\ &\approx V_{RO}^s + C_b^s C_l^b \delta V_{IMU}^{ned} - C_b^s C_l^b (V_{IMU}^{ned} \times) \phi - C_b^s (l_{RO}^b \times) \delta \omega_{ib}^b \end{aligned} \quad (6-31)$$

Where \hat{V}_{IMU}^{ned} is the velocity of the vehicle at the center of the IMU represented in the navigation frame, $\hat{\omega}_{nb}^b$ is the angular rate of the body frame, in which the velocity is measured by the RO, with respect to the navigation frame, l_{RO}^b is the lever arm between the RO and the IMU represented in the body frame, \hat{C}_l^b is the rotation matrix between the navigation and body frame. δV_{IMU}^{ned} is the

velocity error of the vehicle at the center of the IMU and $\delta\omega_{ib}^b$ is the angular rate measurement error. The EKF measurement updates can be expressed as:

$$\begin{aligned} z_{V_{RO}} &= \hat{V}_{RO}^s - \tilde{V}_{RO}^s \\ &= C_b^s C_l^b \delta V_{IMU}^{ned} - C_b^s C_l^b (V_{IMU}^{ned} \times) \phi - C_b^s (l_{RO}^b \times) \delta\omega_{ib}^b - e_V \end{aligned} \quad (6-32)$$

From Equation 6-31 the design matrix can be expressed as:

$$H_{RO} = [0_{3 \times 3} : C_l^s : -C_l^s V_{IMU}^{ned} : 0_{3 \times 3} : -C_b^s l_{RO}^b : 0_{3 \times 12}] \quad (6-33)$$

The innovation sequence between the measurement updates $z_{V_{RO}}$ and the estimated measurements $\hat{z}_{V_{RO}}$ is obtained as:

$$\begin{aligned} \delta z_{V_{RO}} &= z_{V_{RO}} - \hat{z}_{V_{RO}} \\ &= z_{V_{RO}} - H_{RO} x \end{aligned} \quad (6-34)$$

After the innovation sequence δz_k and design matrix H_k computation for each sensor, the Kalman gain K_k , the updated states \hat{x}_k^+ , and its updated covariance matrix P_k^+ can be obtained as:

$$K_k = P_k^- H_k^T (H_k P_k^- H_k^T + R_k)^{-1} \quad (6-35)$$

$$\hat{x}_k^+ = \hat{x}_k^- + K_k \delta z_k \quad (6-36)$$

$$P_k^+ = (I - K_k H_k) P_k^- \quad (6-37)$$

6.2 Experimental Results

The results presented in the upcoming subsections are obtained from two experimental flights with 3DR Solo quadcopter equipped with micro-FMCW radar.

6.2.1 Hardware setup

A 24-GHz micro-FMCW radar by RFbeam is utilized during the flights. The radar is composed of one transmitter and three receiver micro-strip patch antennas, with resolution 0.1 degree and ± 10 degree in Elevation-plane and ± 15 degree in Azimuth-plane. The radar can measure distances up to 300m for cars and 100m for persons with 1m resolution. Figure 6-7 illustrates the utilized radar.

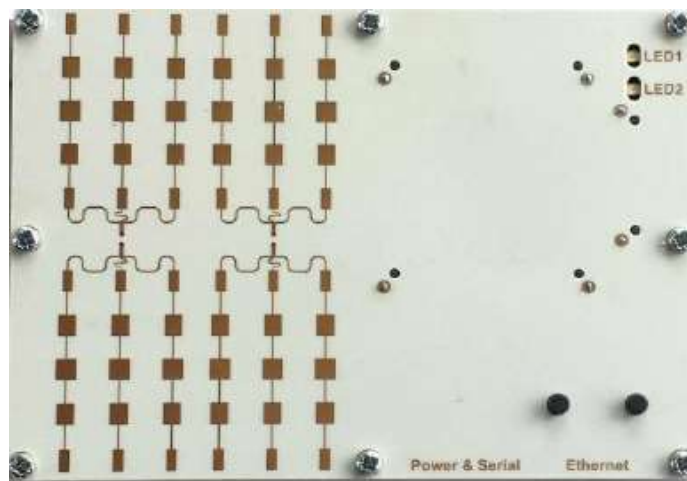


Figure 6-7: Utilized FMCW radar (RF-beam).

The 3DR Solo Quadcopter is equipped with Pixhawk-2 autopilot with InvenSense MPU-6000 Micro-Electro-Mechanical Systems (MEMS)-based IMU, MS5611 barometer and single point U-blox GPS. The maximum useful payload is 420g. During the flights, the payload for the experiments comprises the radar system at the UAV belly connected through an Ethernet to BULLET-M, 2.4 GHz 28dBm transmitter with omni direction antenna (BM2HP by Ubiquity) with the ability to transmit 100+ Mbps. Figure 6-8 illustrates the utilized BULLET-M module for data transfer.



Figure 6-8: Utilized BULLET-M module (Ubiquiti).

The transmitter and the radar are connected to 3S Lipo battery different from the quadcopter battery. On the other side a Nano Station-M (receiver with directive panel antenna and dual-polarity) is connected to the ground station to collect the data from the radar as shown in Figure 6-9.



Figure 6-9: Hardware setup configuration.

6.2.2 Results

The experiments were conducted on two different days, with two different trajectories, and the radar was pitched by 60 degrees from the quadcopter body as shown in Figure 6-10.

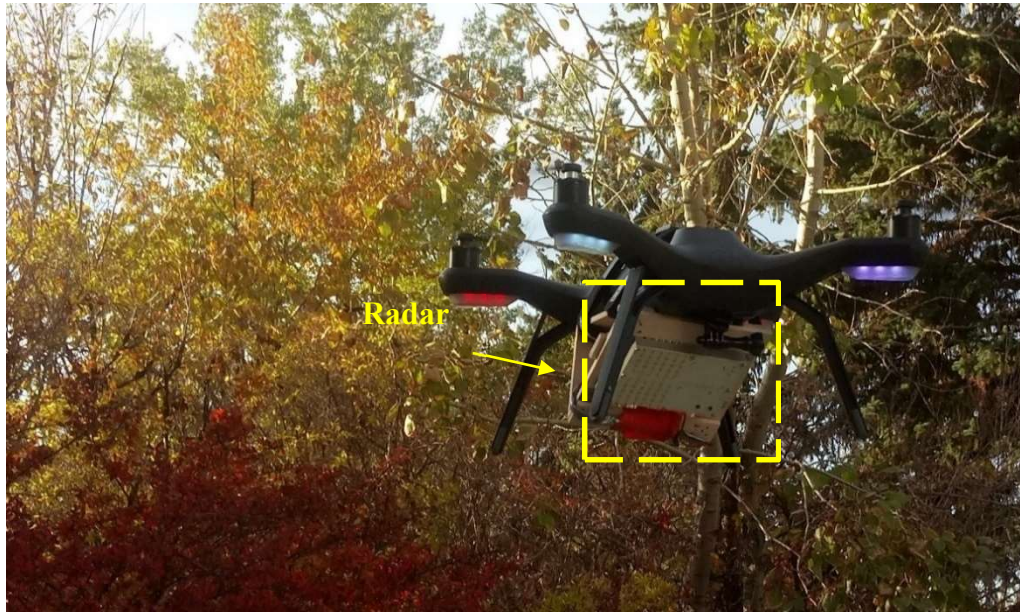


Figure 6-10: Attached radar to the SOLO quadcopter.

6.2.2.1 First Experiment

The first flight composed of 2-laps, 10 waypoints of total flight time 155sec, with maximum speed of 5m/s as shown in Figure 6-11.

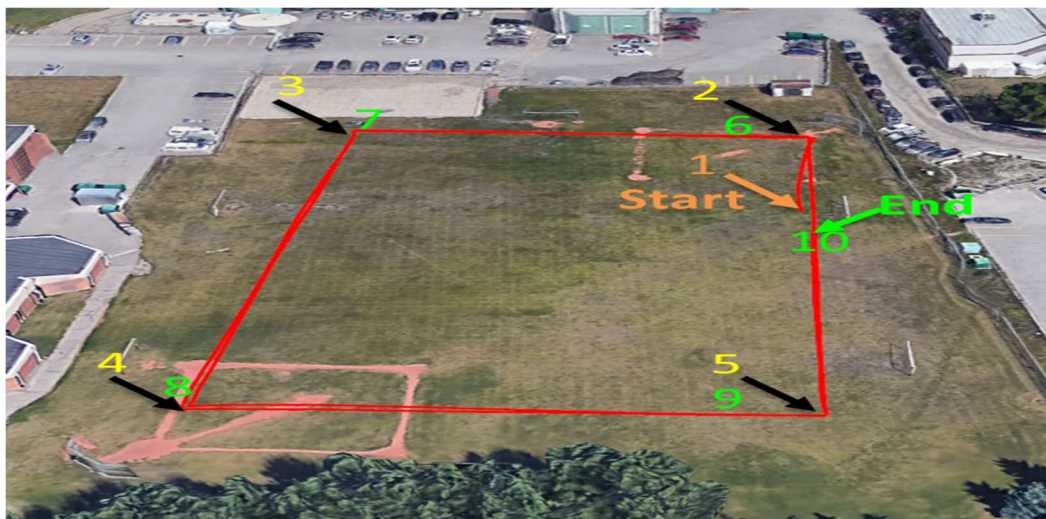


Figure 6-11: First flight trajectory.

In Figure 6-12, the UAV velocity of the body in forward-direction is compared to the estimated velocity from radar using the proposed approach.

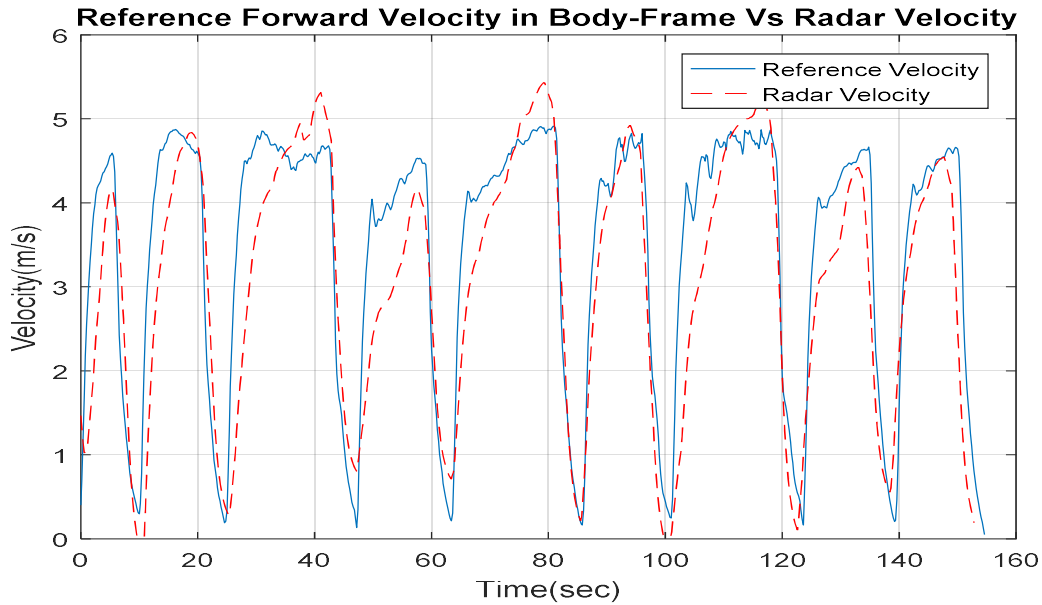


Figure 6-12: Comparison between forward ground truth velocity in the body frame, which obtained from (GNSS/INS) integration, and estimated velocity from the RO.

As seen in previous figures the proposed RO system can estimate the vehicle forward velocity with RMS error value of 1.2 m/s. The standard deviation of the estimated forward velocity from the RO is 0.07 m/s while the barometer and the magnetometer standard divisions are 0.5 m and 5 degrees respectively. Five outage scenarios were carried, with different outage periods, ranging from 45sec to 135sec. The first outage period is performed for 45 sec. Figure 6-13 shows a comparison between the estimated 2D flight trajectory outage segments from the GNSS/INS integration (ground truth segment), and RO aided navigation during the first flight for 45 secs of GNSS signal outage. Figure 6-14 shows a comparison between the estimated 2D flight trajectory outage segments from the GNSS/INS integration (ground truth segment), and RO aided navigation during the first flight for 135 secs of GNSS signal outage.

Figure 6-15 illustrates the ability of the proposed RO to mitigate the INS drift at the period of the unavailability of GNSS signals, and enhance the navigation solution to reach maximum error of 8 m in 135 secs with 3D RMSE of 5.8 m.

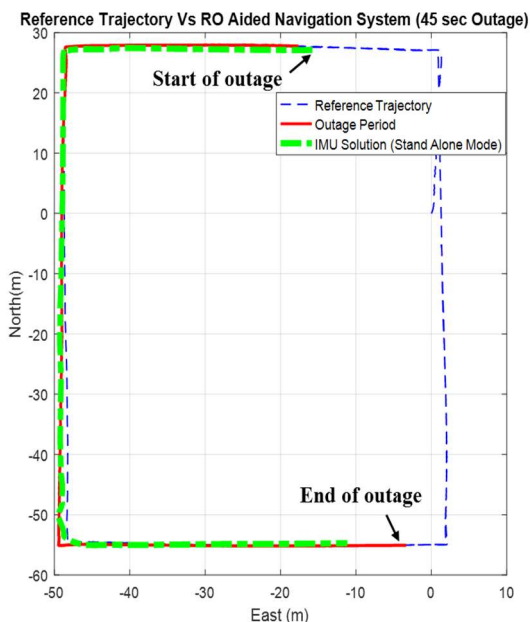


Figure 6-13: A comparison between the estimated 2D flight trajectory outage segments from the GNSS/INS integration (ground truth segment), and RO aided navigation system.

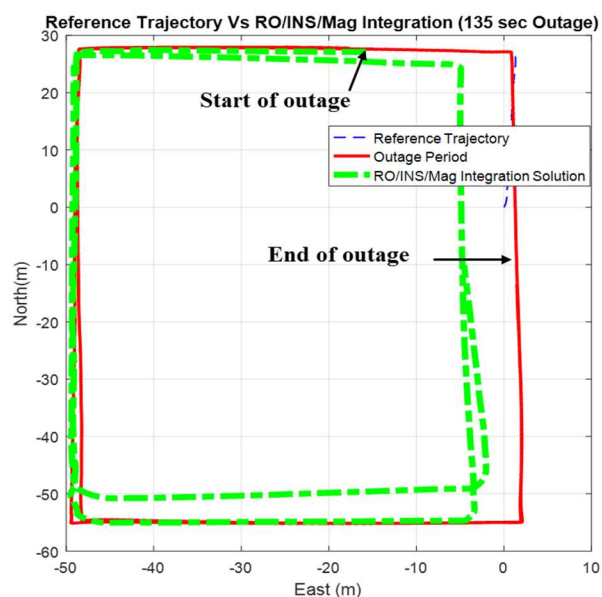


Figure 6-14: A comparison between the estimated 2D flight trajectory outage segments from the GNSS/INS integration (ground truth segment), and RO aided navigation system.

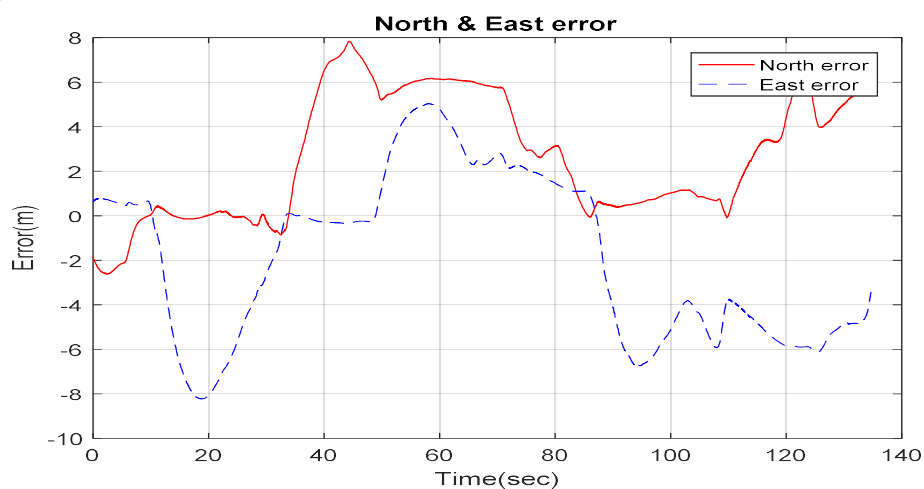


Figure 6-15: The north and east errors, which obtained from the RO aided navigation system during the GNSS outage period.

Figure 6-16 shows a comparison between the estimated 2D flight trajectory outage segments from the GNSS/INS integration (ground truth segment), and INS in standalone mode during the first flight for 135 secs of GNSS signal outage. Figures 6-17 illustrates the navigation errors in INS stand-alone mode in the North and East directions during 135 secs of GNSS signal outage.

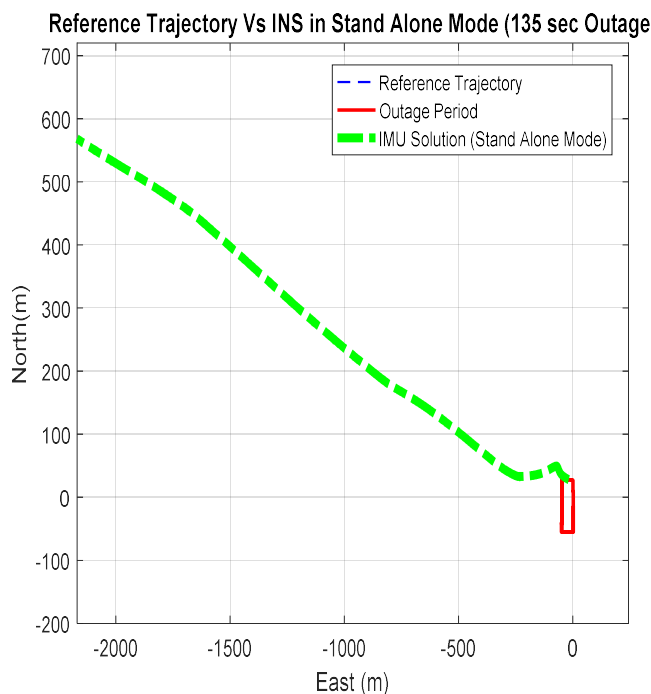


Figure 6-16: A comparison between the estimated 2D flight trajectory outage segments from the GNSS/INS integration (ground truth segment), and INS/Mag/Baro in standalone mode during 135 sec of GNSS signal outage.

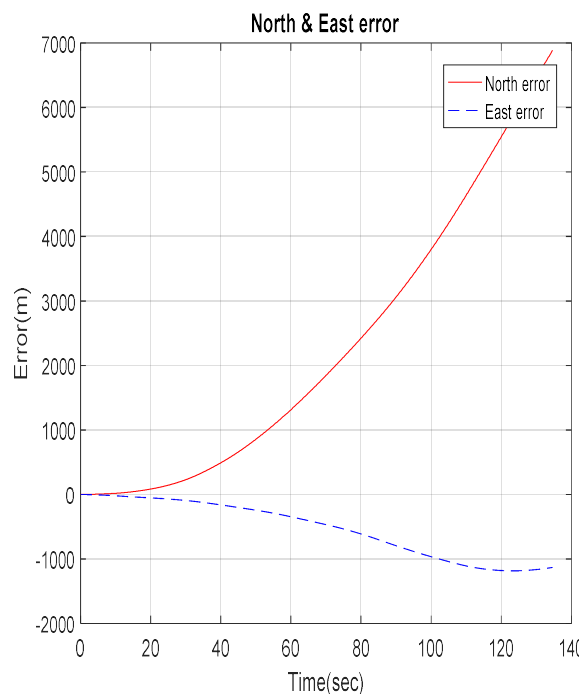


Figure 6-17: The North and East errors which obtained from INS/Mag/Baro in standalone mode during the GNSS outage period.

The following table provides a comparison of the RMS errors values for the position states obtained from INS in standalone mode, and RO aided navigation system during the GNSS outage periods. The proposed RO aided navigation technique reduced the 3D positioning errors to 1.19% during 45 secs, and 0.15% during 135 secs of the INS drift errors in standalone mode during the GNSS signal outage.

Table 6-1: Comparison between (RMS errors) values for the position states obtained from (INS), and (RO) aided navigation system with respect to the ground truth values.

	Symbol	First Flight	
		(45 sec)	(135 sec)
		Outage	Outage
North Error (m)	INS	142.96	2890
	RO aided navigation	1.65	3.60
East Error (m)	INS	140.54	1750
	RO aided navigation	2.18	3.89
Height Error (m)	INS	220.74	2090
	RO aided navigation	2.26	2.36
3D Position Error (m)	INS	298.18	3970
	RO aided navigation	3.56	5.81
Enhancement Percentage From INS%	RO aided navigation	98.81	99.85

Figure 6-18 shows a comparison between the RMS of the 3D positioning errors for RO aided navigation system during five GNSS outage periods ranged from 45 secs to 135 secs.

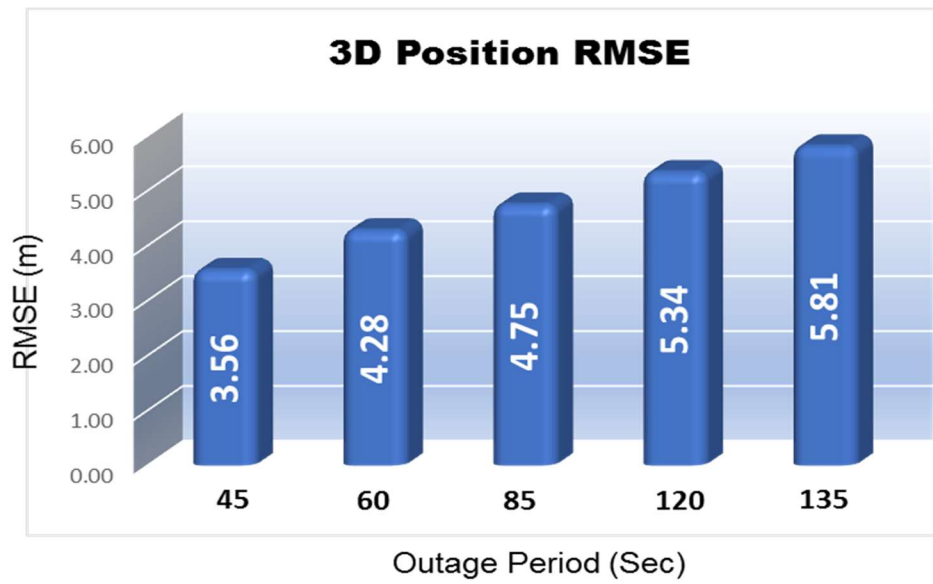


Figure 6-18: RMS 3D positioning errors for RO aided navigation system during different outage periods.

6.2.2.2 Second Experiment

The second flight is a diamond shape trajectory of 13 waypoints, with total flight time of 155 sec as shown in Figure 6-19.

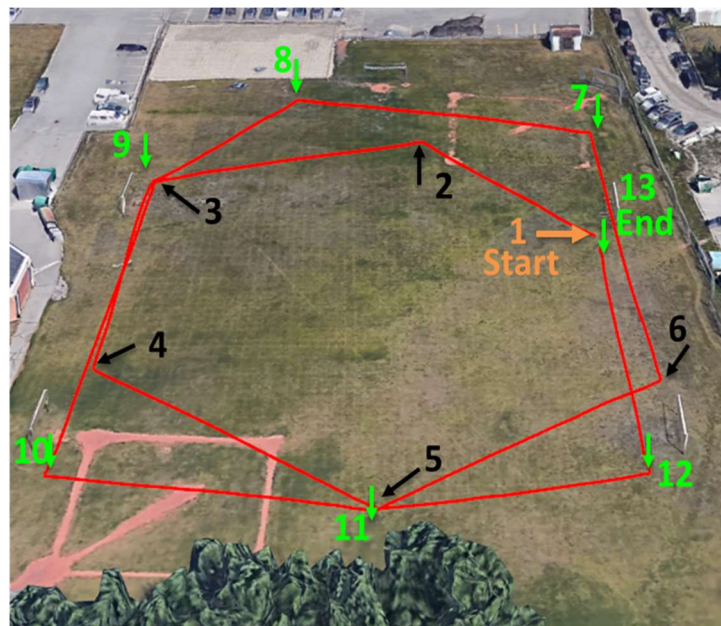


Figure 6-19: Second flight trajectory.

The reference forward velocity was compared with the RO estimated velocity as shown in Figure 6-20.

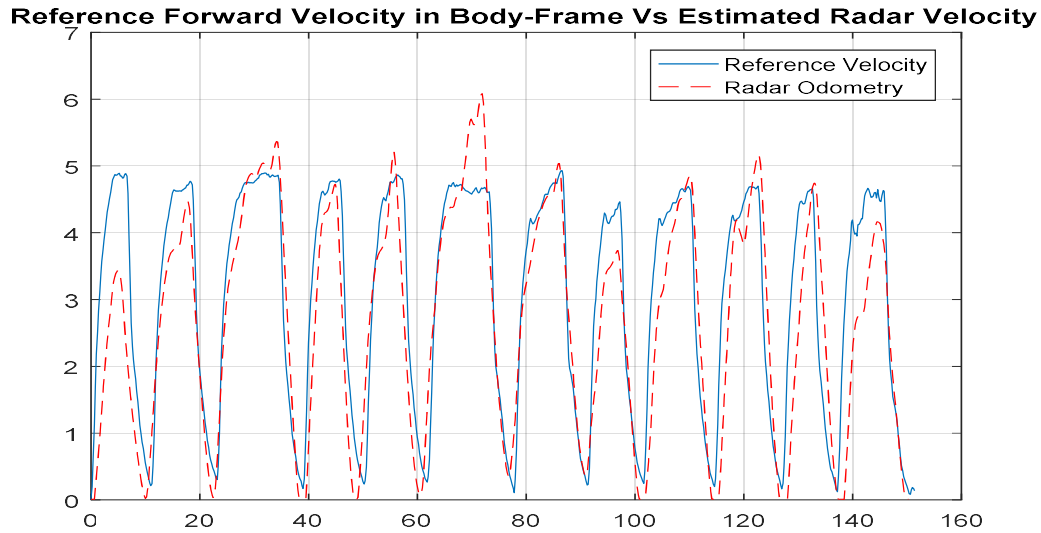


Figure 6-20: Comparison between forward ground truth velocity in the body frame, which Obtained from (GNSS/INS) integration, and estimated velocity from the RO.

Also, during the second experiment, the proposed RO demonstrated its ability to estimate the vehicle's forward velocity with an RMS error value of 2.1 m/s. The standard deviation of the estimated forward velocity from the RO is 0.07 m/s while the barometer and the magnetometer standard divisions are 0.5 m and 5 degrees respectively and are obtained by the similar manner. Five outage scenarios were carried out, with different outage periods, ranging from 45 secs to 120 secs. Figure 6-21 shows a comparison between the estimated 2D flight trajectory outage segments from the GNSS/INS integration (ground truth segment), and RO aided navigation during the second flight for 45 secs of GNSS signal outage. Figure 6-22 shows a comparison between the estimated 2D flight trajectory outage segments from the GNSS/INS integration (ground truth segment), and RO aided navigation during the second flight for 120 secs of GNSS signal outage.

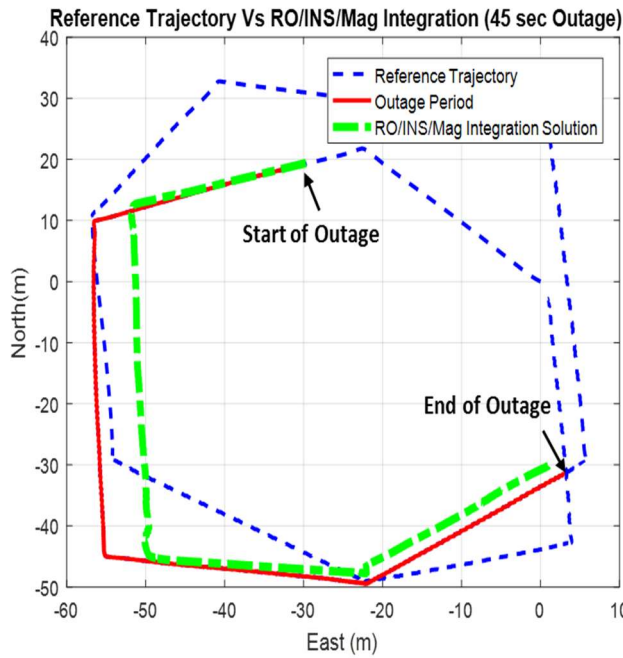


Figure 6-21: A comparison between the estimated 2D flight trajectory outage segments from the GNSS/INS integration (ground truth segment), and RO aided navigation system.

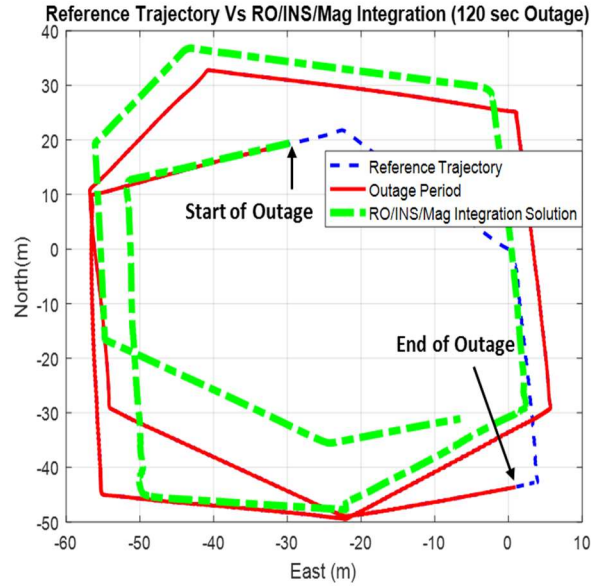


Figure 6-22: A comparison between the estimated 2D flight trajectory outage segments from the GNSS/INS integration (ground truth segment), and RO aided navigation system.

Figure 6-23 illustrates the effectiveness of the proposed RO in compensating for the absence of GNSS system during outage periods, and enhance the navigation solution, with a 3D RMSE 8.1 m in 120 secs.

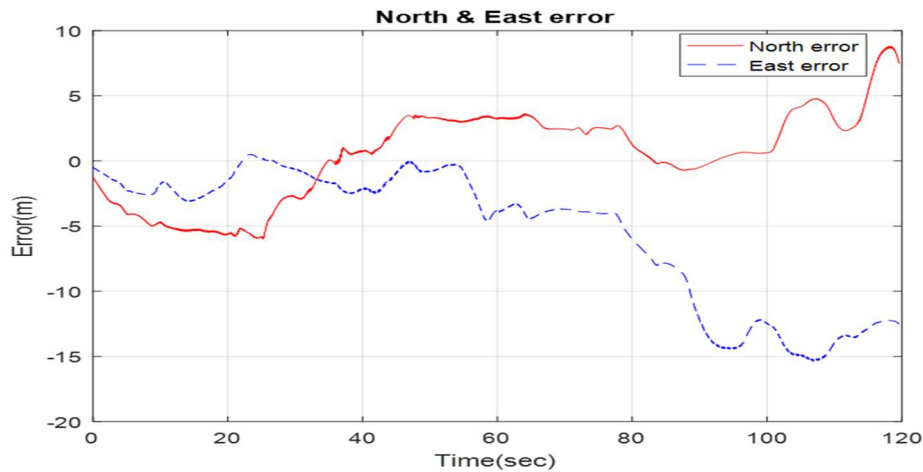


Figure 6-23: The North and East errors, which obtained from the RO aided navigation system during the GNSS outage period.

Figure 6-24 illustrates a comparison between the estimated 2D flight trajectory outage segments from the GNSS/INS integration (ground truth segment), and INS in standalone mode during the second flight for 120 secs of GNSS signal outage. Figure 6-25 illustrates the INS errors in the North and East directions during 120 secs of GNSS signal outage.

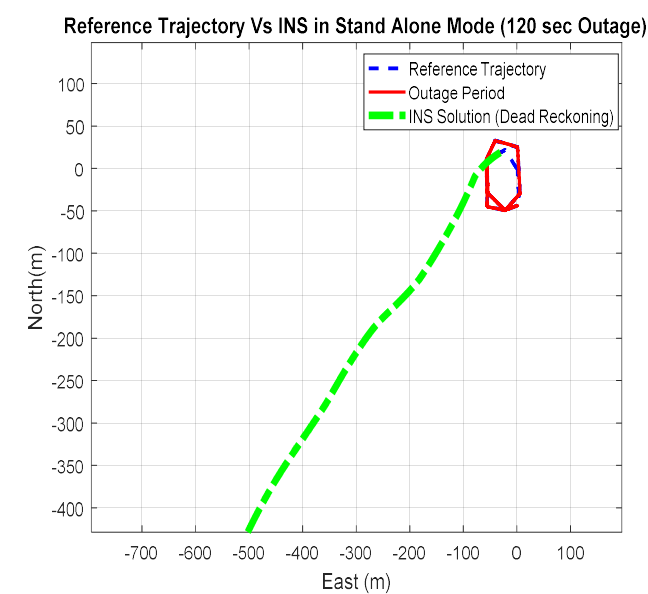


Figure 6-24: A comparison between the estimated 2D flight trajectory outage segments from the GNSS/INS integration (ground truth segment), and INS/Mag/Baro in standalone mode during 120 sec of GNSS signal outage.

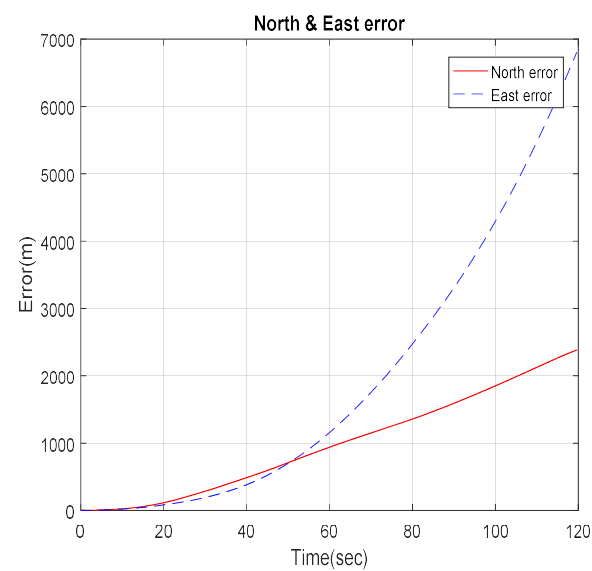


Figure 6-25: The North and East errors which obtained from INS/Mag/Baro in standalone mode during the GNSS outage period.

The following table demonstrates a comparison of the RMS errors values for the position states obtained from INS in standalone mode, and RO aided navigation system during the GNSS outages periods. The proposed approach successfully reduced the 3D positioning errors to 1.81% during 45 secs, and 0.24% during 120 secs of the INS drift errors in standalone mode during the GNSS signal outage.

Table 6-2: Comparison between (RMS errors) values for the position states obtained from (INS), and (RO) aided navigation system with respect to the ground truth values.

	Symbol	Second Flight	
		(45 sec)	(120 sec)
		Outage	Outage
North Error (m)	INS	159.13	1090
	RO aided navigation	2.58	3.15
East Error (m)	INS	126.68	2460
	RO aided navigation	3.26	6.82
Height Error (m)	INS	201.88	2090
	RO aided navigation	3.09	3.12
3D Position Error (m)	INS	286.57	3400
	RO aided navigation	5.19	8.14
Enhancement Percentage From INS%	RO aided navigation	98.19	99.76

Figure 6-26 shows comparison between the RMS values of the 3D positioning errors for RO aided navigation system during five GNSS outage periods ranged from 45 secs to 120 secs.

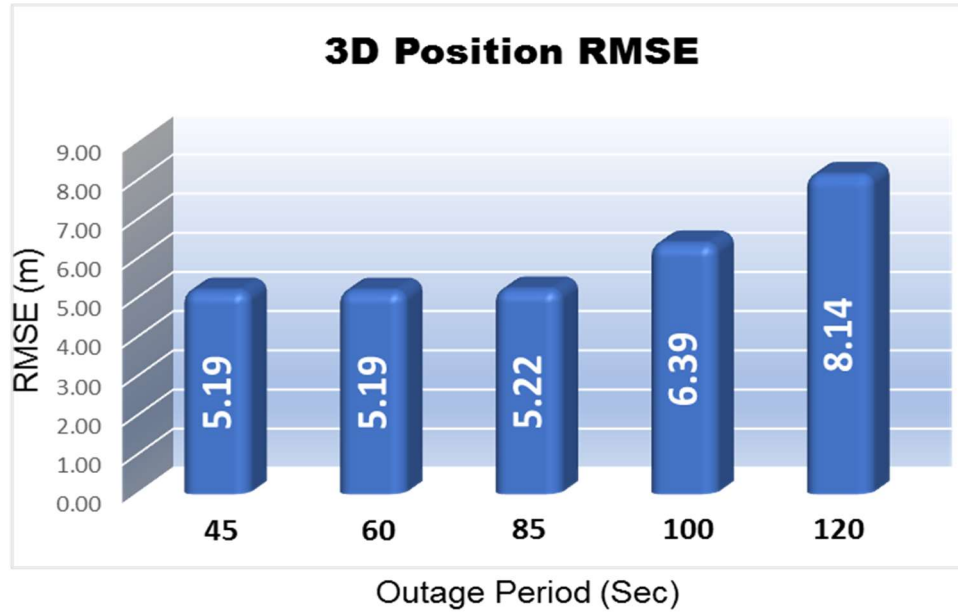


Figure 6-26: RMS 3D positioning errors for RO aided navigation system during different outage periods.

6.3 Summary

A novel RO aided navigation approach is proposed to enhance the positioning accuracy and reliability of the navigation solution during the GNSS outage periods for UAVs. A lightweight FMCW radar has been attached to the UAV to provide a range Doppler map of the received signals from the ground objects. The range Doppler map is processed to robustly estimate the radial velocity of the ground scatterers. The proposed system is divided into three main steps, which are, data acquisition, target detection and velocity extraction, and data fusion. The proposed target detection technique relies on new adaptive thresholding approach, image binarization, and connected components algorithms. Thanks to the employed target detection approach which contributes toward obtaining a more accurate and reliable navigation solution during the GNSS signal outage.

The resultant forward velocity from RO, magnetometer, and barometer measurements are then fused with the INS in an EKF during the GNSS signal outage. This RO aided navigation system can operate in real-time since the target detection processing time is around 1 ms.

In addition, the proposed system does not require artificial reflectors for target detection process. Instead, this system benefits from the typical ground objects as natural scatterers and depends on the proposed detection step to accommodate the expected variation of ground objects' reflectance. The proposed system is evaluated through two-real flights' data with different maneuvers. To assess the proposed system's performance, five outages were performed in each flight. The results clearly indicate that the RO aided navigation system can aid the INS during GNSS signal outage. It also demonstrates its capability of enhancing the average 3D positioning accuracy by 99.78% for the first flight, and 99.67% for the second flight.

Chapter Seven: UAVs Navigation in Denied GNSS Environments using an Integrated Radar and Visual Odometry

This chapter presents an integrated navigation system for UAVs in GNSS denied environments based on FMCW RO and enhanced monocular VO. The incorporation of the RO and VO into one integrated system help toward handling the limitations of each one of them. The RO is immune against the environmental conditions such as rain, fog, and dust. Unlike the camera, it is not affected by the change of the illumination or featureless area. On the other hand, the RO measurements are affected while flying over multiple objects with different altitudes, ranges, and angles. The utilized radar doesn't provide azimuth and elevation measurements for the observed objects which have different angles values inside the radar beam and the radar tilting angle (60 degree) is the only utilized angle to estimate the vehicle forward velocity. Hence, the accuracy of the estimated forward velocity from the RO is downgraded while flying over non-flat terrain. Therefore, the incorporation of the camera in such challenging scenarios can help to enhance the navigation solution. By merging both RO and VO into a one integrated system, the scale ambiguity of the monocular VO can be resolved by the estimated height from the RO. In addition, this system can provide a more accurate navigation solution than the low cost invenSense MPU 6000 IMU in standalone mode and the enhanced monocular VO/mag/barometer/ INS integrated system.

7.1 Overview of the Integrated Navigational System

This integrated system is mainly proposed to significantly improve the 3D positioning accuracy for the IMU during the GNSS signals outages and to resolve the proposed monocular VO scale ambiguity based on the radar height measurements. This system is consisting of a GoPro HERO4 Black camera and a micro FMCW radar which have been mounted on the SOLO quadcopter.

The enhanced monocular VO is proposed based on the optical flow and regression trees. The optical flow is utilized to estimate the vehicle forward velocity while the regression trees is employed for the estimated velocity drift compensation purpose. On the other hand, the Gaussian kernel, and local maxima-based approaches are employed for the RO target detection. This system fuses the estimated forward velocities in the body frame, which are obtained from the RO, and the enhanced monocular VO with the IMU, barometer, and magnetometer measurements via an EKF. This system is implemented based on 3 major steps which are RO, enhanced monocular VO, and the data fusion.

7.1.1 FMCW RO

The proposed RO estimates the vehicle forward velocity and the height above the ground from its RDM. This RO is consisting of two main steps which are, data accusation, and, target detection and data extraction.

7.1.1.1 Data Accusation

This RO acquires the ranges and velocities measurements for the reflected ground scatterer based on its internal radar signal processing for the received signals. On the beginning, the original transmitted signals are mixed with the received signals in a low pass filter to estimate the video signal. This raw video signals are then sampled with 264 ns sampling rate and a two-dimensional FFT is then applied on the spectrum of the sampled signal [82] to form the radar RDM for each one of the three receiving antenna. A mean RDM is generated buy by averaging the RDM from all antennas. Figure 7-1 illustrates an RDM image where the X-axis represents the velocity measurements while the Y-axis provides the range measurements. The 32-Bit amplitude value at each pixel represents the received echo signals strength from different ground scatters.

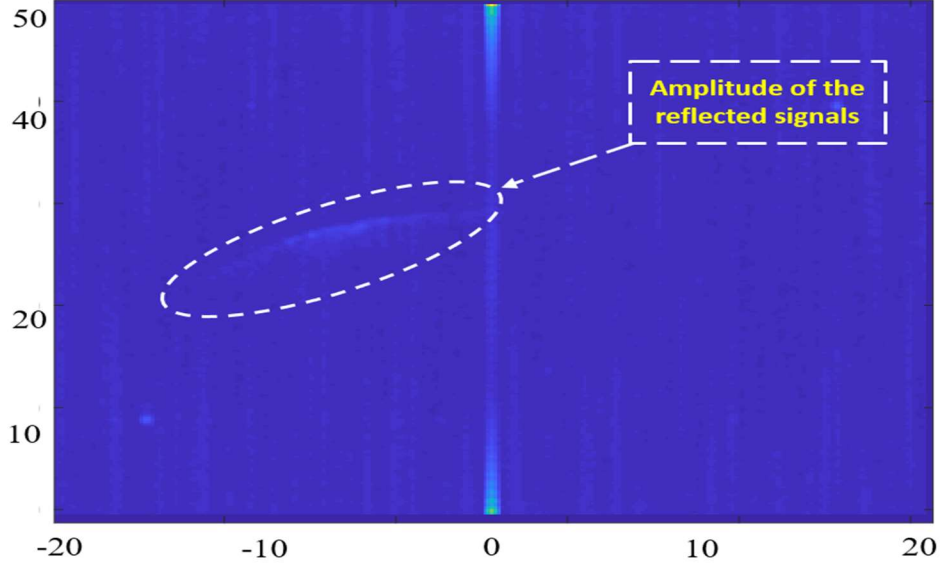


Figure 7-1: Reflected ground signals in the RDM image.

This RDM is acquired from the micro radar through an ethernet cable after performing the radar signal processing inside the radar. This generated map is then utilized for the target detection, velocity, and height extraction purpose.

7.1.1.2 Targets Detection and Data Extraction

An efficient target detection technique is proposed based on the Gaussian kernel and local maxima. This Gaussian kernel is convolved with the RDM for candidates targets extraction since this kernel is maximizing the strong scatterers from the ground objects and depressed the weak signals. A local maxima-based approach is applied for these candidates and the most five strongest candidates are considered to be the detected targets as shown in Figure 7-2. The target detection process takes approximately 1.3ms which make it more convenient for real time applications.

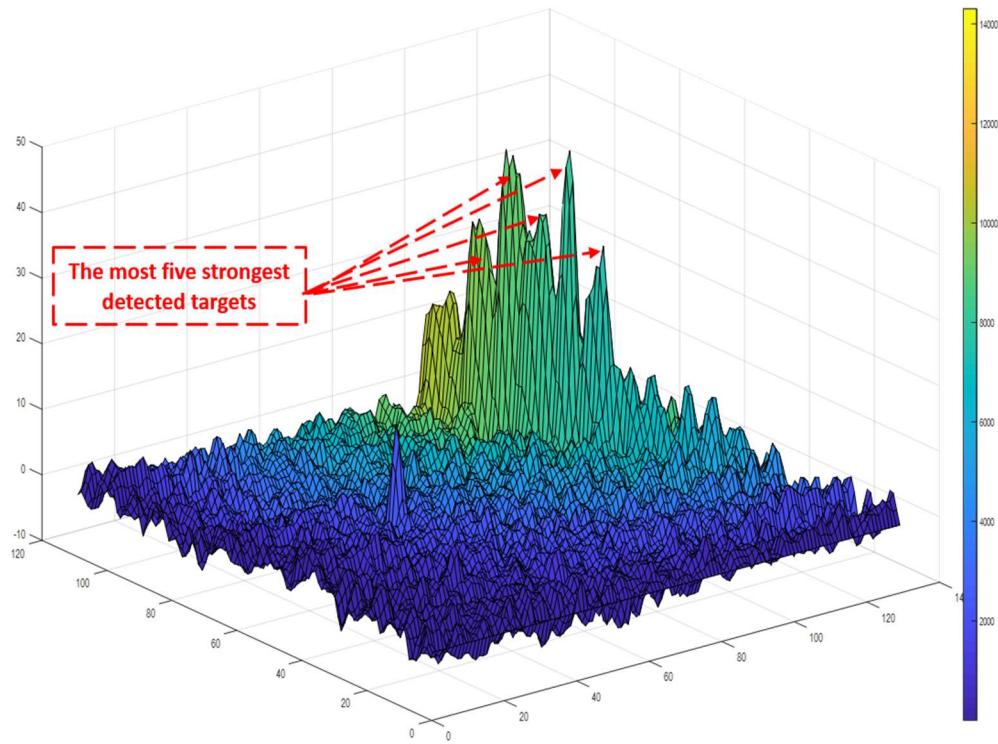


Figure 7-2: Radar detected targets.

The radial velocity and the range for each detected target are then acquired directly from the X and Y axis of this image respectively. These radial velocities are projected by the radar tilting angle which is 60 degrees toward the flight path direction and the vehicle pitch angel is then compensated from these projected velocities. These projected components are then averaged to obtain resultant forward velocity of the vehicle in the body frame. On the other hand, the ranges are projected and compensated by the same angels toward the vertical direction and then averaged to obtain the height above the ground level for the vehicle.

7.1.2 Enhanced Monocular VO

A GoPro HERO4 Black camera is attached to the quadcopter with a resolution of 1080x1920, and 30 frames per second video measurements rate. This camera is mounted on the UAV to have a downward facing orientation. The proposed VO consists of two main steps which are, monocular

VO based on the optical flow, and regression trees-based approach for the velocity drift errors compensation respectively.

7.1.2.1 Monocular VO

The proposed VO extracts the optical flow vectors in the X and Y directions by detecting the features of interest from the video frames using SURF detector [50]. These detected features are then matched between successive frames. The main reason for utilizing the SURF algorithm that it has a low computational load which make it more convenient for real-time operation. An MSAC algorithm is employed for outliers (incorrect matches) rejection purpose between the matched points. Suppose a point $P = [X, Y, Z]$ in the space is projected by a pinhole camera model to the image plane at point $p = [x_{pix}, y_{pix}, f_{cam}]$ as

$$p = \frac{f_{cam}}{Z} P \quad (7-1)$$

Where f_{cam} is the the camera's focal length. Since the camera is mounted perpendicularly to a vehicle body, the coordinate Z is equal to the distance between ground and camera's projection origin. This ground distance is obtained from the estimated radar height as shown in Figure 7-3. By having this ground distance, the displacement in the image plane $(\Delta u, \Delta v)$ can be converted to a real word displacement $(\Delta X, \Delta Y)$ as

$$\Delta X = -\frac{1}{f_{cam}} \Delta u \cdot Z, \Delta Y = -\frac{1}{f_{cam}} \Delta v \cdot Z \quad (7-2)$$

The displacement in the image plane is obtained after removing the outliers from the matched points between two successive frames. As the computed displacement $(\Delta u, \Delta v)$ is usually in pixels,

it is required to convert it into real-world units (e.g. meters). Therefore, Equation 7-2 then changes to

$$\Delta X = -\frac{s}{f_{cam}} \Delta u \cdot Z, \Delta Y = -\frac{s}{f_{cam}} \Delta v \cdot Z \quad (7-3)$$

Where s is the pixel size. The optical vectors (u, v) are obtained by multiplying these image displacements by the camera measurements rate. The gyro's measurements ω_x, ω_y are then utilized to compensate the vehicle rotational motion effect from the estimated optical flow vectors in the X and Y directions. These compensated vectors are then utilized to estimate the vehicle forward velocity as

$$V_{VO} = -\left[\frac{s}{f_{cam}} u - f \tan(\omega_y \Delta t)\right] \cdot Z \quad (7-4)$$

Where Δt is the time between two consecutive frames.

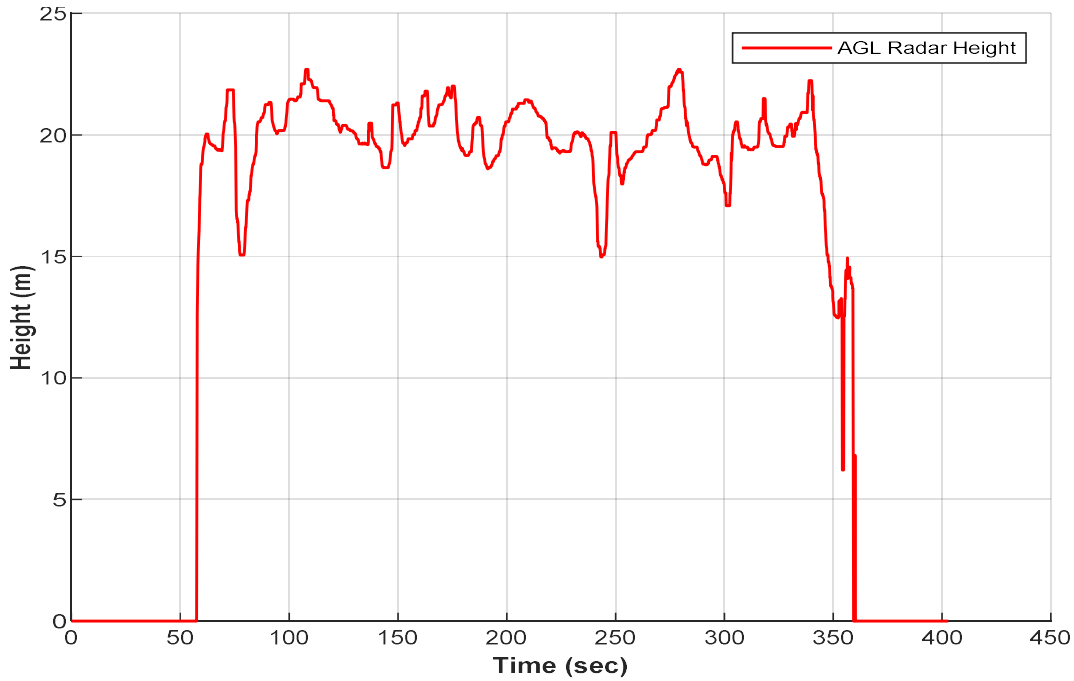


Figure 7-3: RO estimated height.

7.1.2.2 Velocity Compensation

During this phase of process, a learnt regression trees-based approach is employed to enhance the accuracy of the estimated vehicle velocity from the monocular VO. This training process is achieved during the availability of the GNSS signals. The GNSS signals are assumed to be available during the first 50 and 140 sec of the first and second flights respectively. The training process has taken place during the first 40 sec for the first flight while the whole collected data during the first flight and the first 125sec of the second flight are utilized for the training purpose for the second flight. The video frames are divided into 3×3 cells and the optical flow vectors in the X and Y directions are then averaged inside each cell to offer a fixed number of vectors to the regression trees during this stage as shown in Figure 7-4. These averaged optical flow vectors along each cell, the estimated forward velocity from the monocular VO, roll, pitch, and RO height are then utilized as inputs for the regression trees during the training session while the ground truth forward velocity which is obtained from the GNSS/INS/mag/barometer integration is utilized as an output during this training phase. Figure 7-5 illustrates the proposed system architecture during the training session.

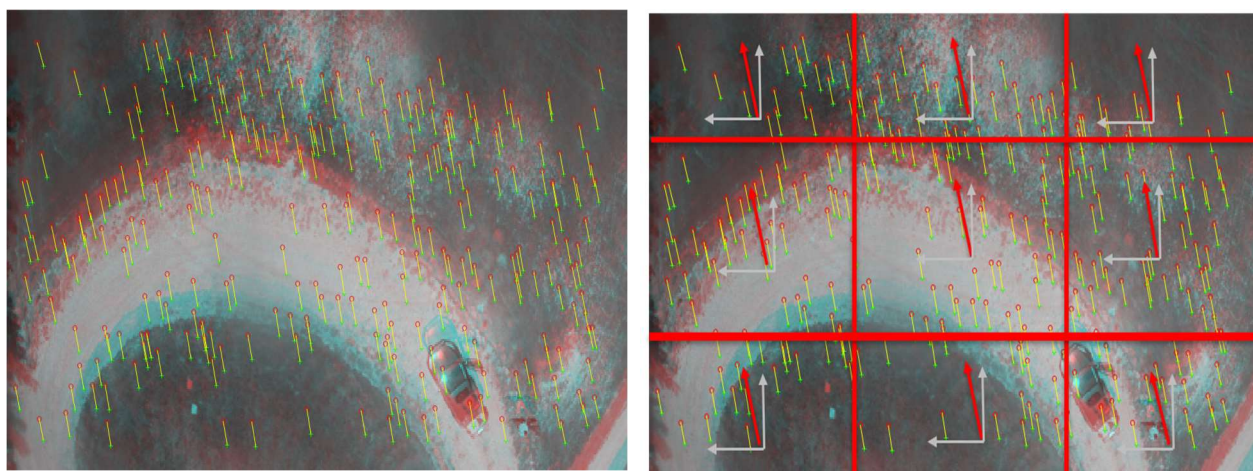


Figure 7-4: The optical flow vectors and the averaging process among 3×3 image cells.

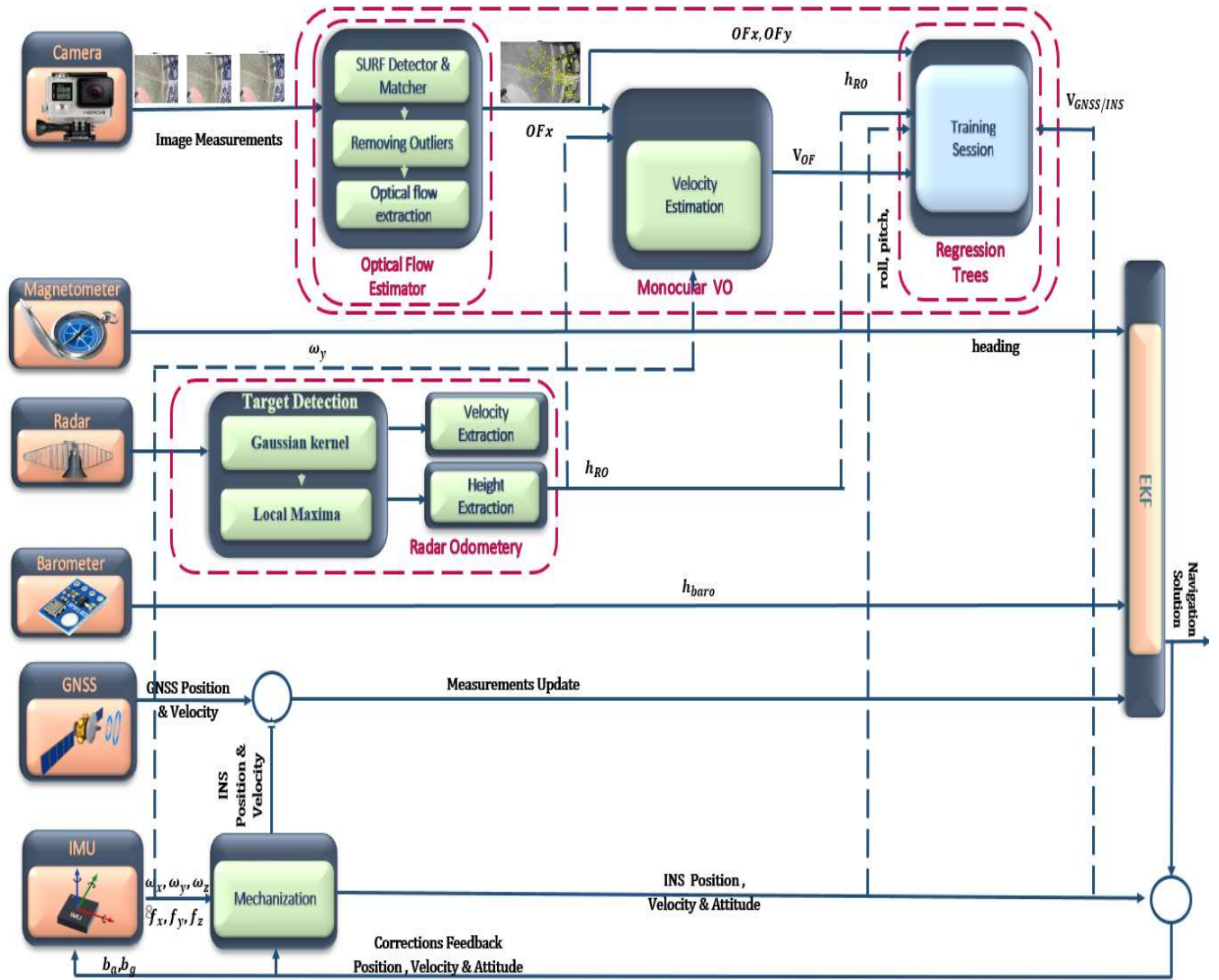


Figure 7-5: Illustrates the proposed system architecture during the training session.

When the GNSS signals get lost, the trained regression trees start to estimate the vehicle forward velocity in an attempt to compensate the monocular VO drift errors. A weighted average between the predicted velocity from the regression trees and the estimated velocity from the monocular VO is utilized as measurements update for the EKF. This weighted average process is performed because the accuracy of the estimated regression trees can not be granted all the time and the trees don't provide any precession measurements for its predictions. These weights are obtained by

computing the RMS errors for the predicted velocity from the regression trees and the estimated velocity from the monocular VO with respect to the reference forward velocity from 40 to 50 sec for the first flight and from 125 to 140 sec for the second flight. The estimated forward velocity from the RO is also utilized as measurements update during this GNSS outage period. Figure 7-6 illustrates the proposed system architecture during the prediction session.

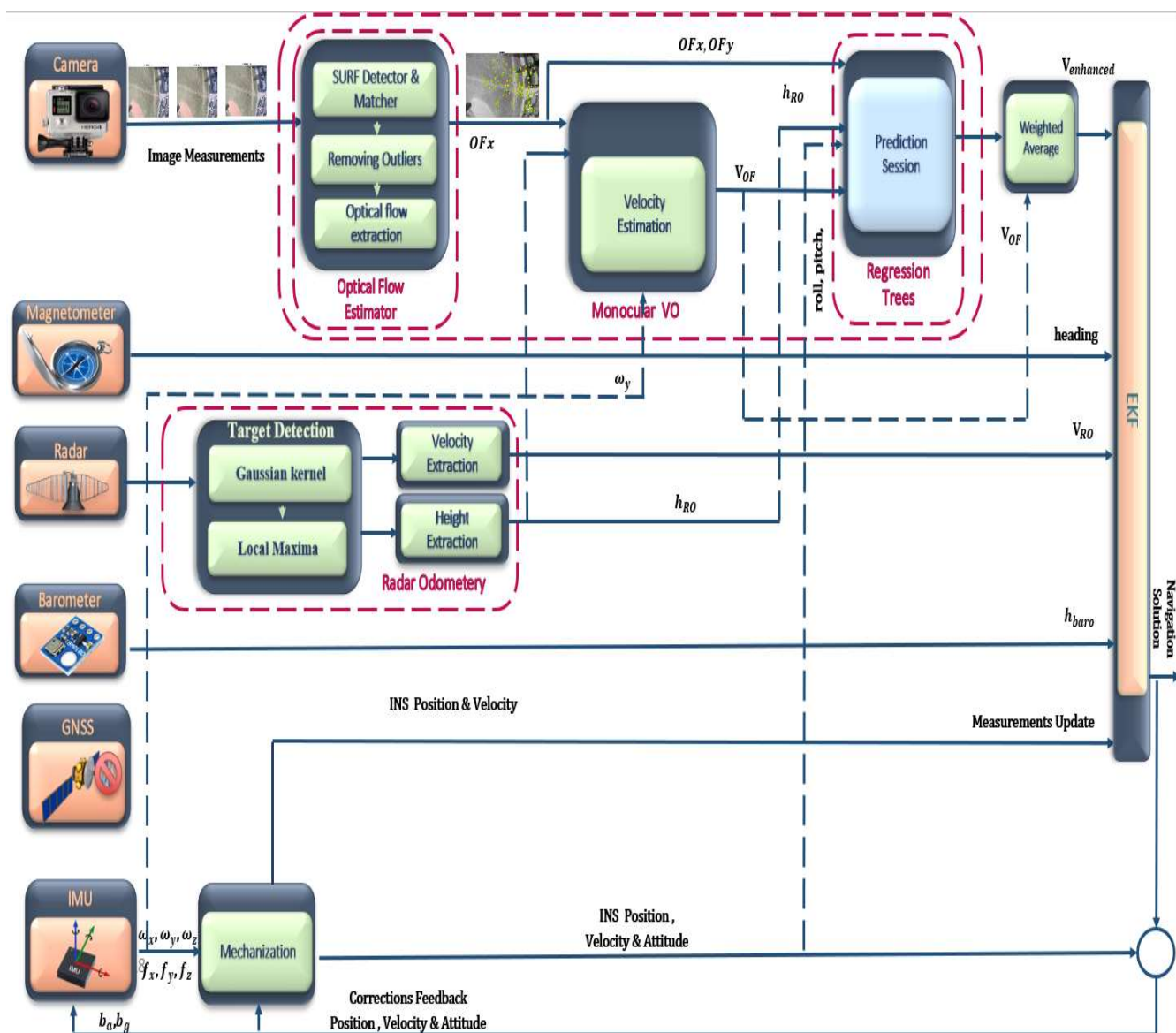


Figure 7-6: Illustrates the proposed system architecture during the prediction session.

As mentioned in the previous chapters, the regression trees-based approach has been employed since it can handle the situation of a missing inputs (optical flow vectors) in some image parts due to the lack of the observed features or inconsistent matches caused by repeated patterns.

7.1.3 Data Fusion

The data fusion is performed between the INS, magnetometer, barometer, enhanced monocular VO, and RO measurements in an EKF. The navigation states include the position, velocity, and attitudes in the navigation frame (n-frame) which are derived from the IMU raw measurements through a mechanization process. The EKF error states vector are 21 states which are the position errors, velocity errors, attitudes errors, accelerometers bias, gyros drift, and the accelerometers and gyros scale factors. The measurements model is performed based on the same equations as in chapter five for the enhanced monocular VO velocity update and as in chapter six for the RO velocity, magnetometer heading, and barometer height updates.

7.2 Hardware setup

A GoPro Hero4 black camera with a fish eye lens is attached to the UAV to get an HD video measurement with 30 frames per second measurements rate. Two real flights are performed in different places. During the first flight the camera field of view is adjusted to be wide angel with a resolution of 1080x1920 while the field of view is adjusted to be medium angel with the same resolution during the second flight. A micro FMCW radar is attached to the quadcopter belly through a wooden frame. This radar has a 24-GHz transmitted frequency with a one transmitter and three receiver antennas. The radar range measurements up to 300 meters with a 1-meter range resolution and velocity measurements up to 40 m/second with a 0.6 m/second resolution accuracy. This radar is attached to a UDOO X86 single board computer for the data accusation purpose. This computer is based on Quad Core 64-bit new-generation x86 processors made by Intel® which is

designed for the PC domain. Figure 7-7 illustrates the utilized UDOO X86 single board computer. A 3DR Solo Quadcopter is utilized during the flights mission. This UAV has a Pixhawk-2 autopilot with InvenSense MPU-6000 MEMS IMU, MS5611 barometer, and U-blox GPS.



Figure 7-7: Utilized UDOO X86 single board computer.

The UDOO X86 and the radar are connected to 3S Lipo battery which is different from the quadcopter battery. The attached camera and radar to the SOLO quadcopter are shown in Figure 7-8.



Figure 7-8: Attached camera and radar to the SOLO quadcopter.

7.3 Results

The experiments were conducted at two different places, with different trajectories, and the radar was pitched by 60 degrees from the quadcopter body. The first flight is performed over a football playground while the second flight is performed over multiple objects with different altitudes such as houses, trees, grass, cars, and hangars. Figure 7-9 shows an aerial image for the first flight while Figure 7-10 shows an aerial image for the second flight.



Figure 7-9: Aerial image for the first flight with a wide field of view.

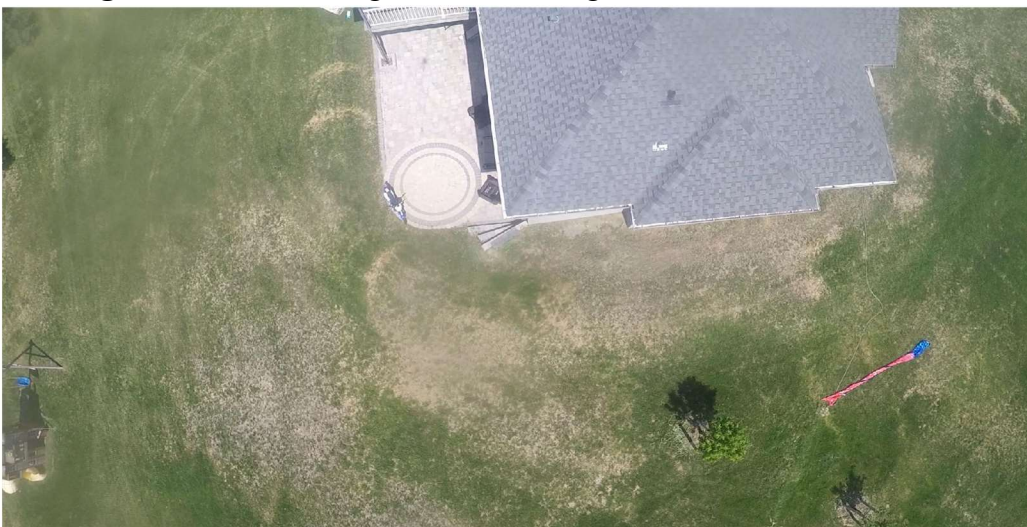


Figure 7-10: Aerial image for the second flight with a medium field of view.

7.3.1 First Experiment

The first flight composed of 10 waypoints of total flight time 393 sec, with maximum speed of 5m/s as shown in Figure 7-11.



Figure 7-11: First flight trajectory.

In Figure 7-12, the estimated velocity from the typical closed form monocular VO, the enhanced monocular VO, and the RO are compared to the UAV reference forward velocity in the body frame with RMS error values of 1.29, 1.02, and 0.49 m/s respectively. The standard division of the estimated forward velocity from the enhanced VO and the RO are 0.075 and 0.07 m/s respectively while the barometer and the magnetometer standard divisions are 0.5 m and 5 degrees respectively.

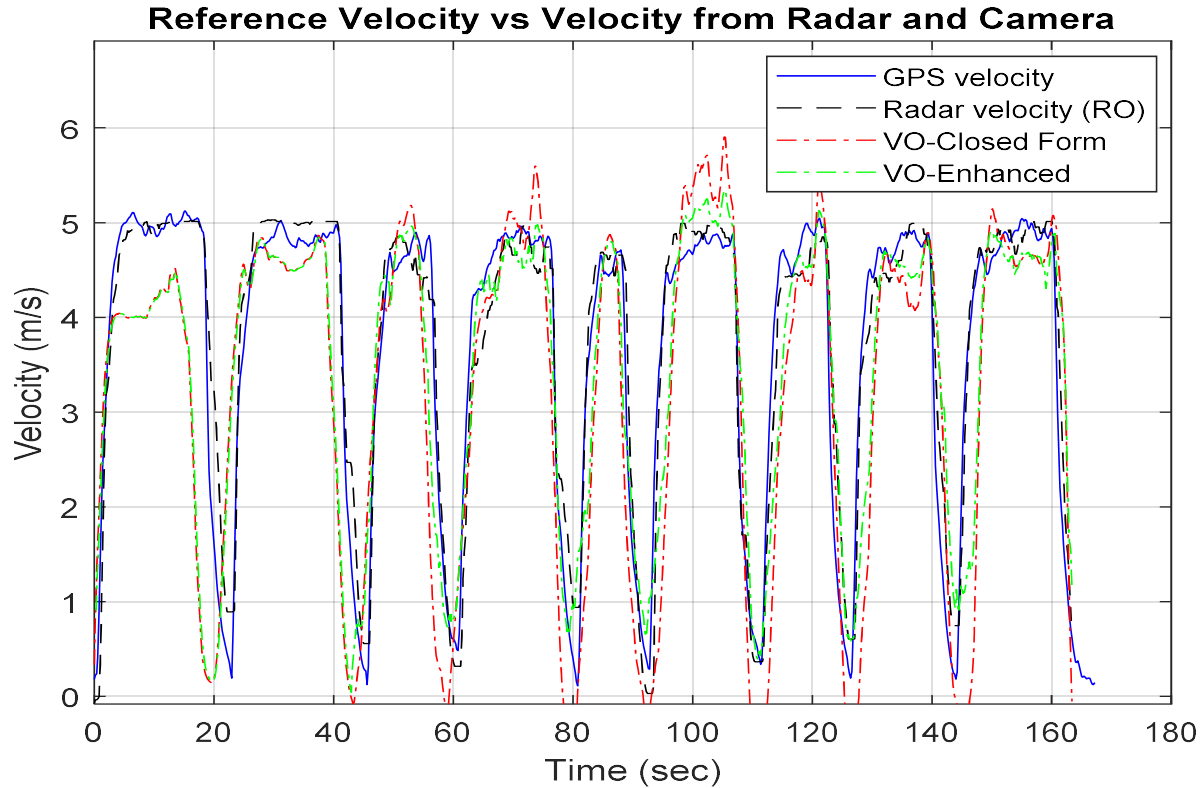


Figure 7-12: Comparison between forward ground truth velocity in the body frame, which is obtained from (GNSS/INS) integration, estimated velocity from the RO, the typical VO, and the enhanced VO.

Three GNSS signal outage scenarios were carried, with different outage periods, ranging from 30sec to 113sec. The first outage period is performed for 30 sec. Figures 7-13 and 7-14 show a comparison between the estimated 2D flight trajectory outage segments from the GNSS/INS integration (ground truth segment), and enhanced monocular VO aided navigation during the first flight for 30 and 113 secs of GNSS signal outage respectively. Figures 7-15 and 7-16 show a comparison between the estimated 2D flight trajectory outage segments from the GNSS/INS integration (ground truth segment), and the proposed integrated system aided navigation during the first flight for 30 and 113 secs of GNSS signal outage respectively.

Figure 7-17 demonstrates the ability of the proposed system (RO/enhanced monocular VO/mag/barometer) to mitigate the INS drift errors when the GNSS signals get lost, and to enhance the 3D RMSE positioning accuracy to be 3.2 m in 113 secs.

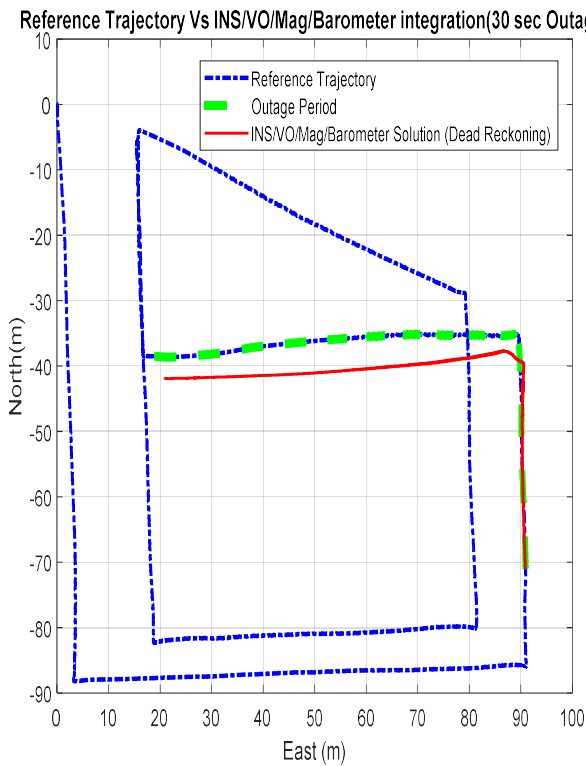


Figure 7-13: A comparison between the estimated 2D flight trajectory outage segments from the GNSS/INS integration (ground truth segment), and the enhanced monocular VO aided navigation system for 30 sec.

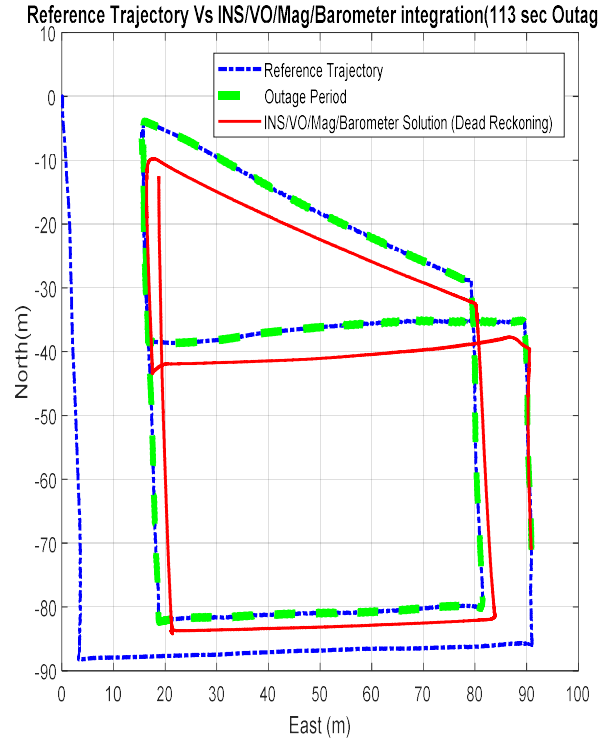


Figure 7-14: A comparison between the estimated 2D flight trajectory outage segments from the GNSS/INS integration (ground truth segment), and the enhanced monocular VO aided navigation system for 113 sec.

Reference Trajectory Vs INS/VO/RO/Mag/Barometer integration(30 sec Outage

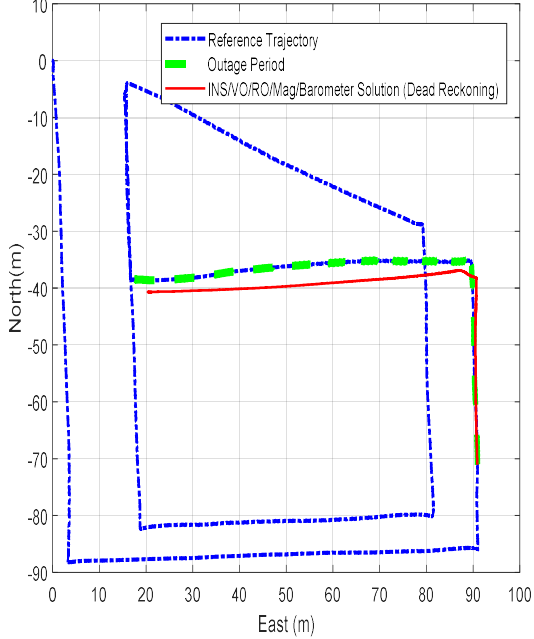


Figure 7-15: A comparison between the estimated 2D flight trajectory outage segments from the GNSS/INS integration (ground truth segment), and the proposed integrated system aided navigation system for 30 sec.

Reference Trajectory Vs INS/VO/RO/Mag/Barometer integration(113 sec Outage

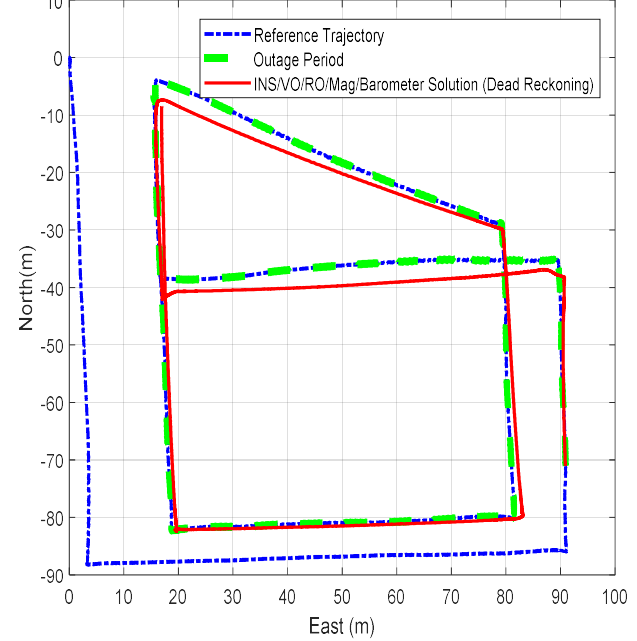


Figure 7-16: A comparison between the estimated 2D flight trajectory outage segments from the GNSS/INS integration (ground truth segment), and the proposed integrated system aided navigation system for 113 sec.

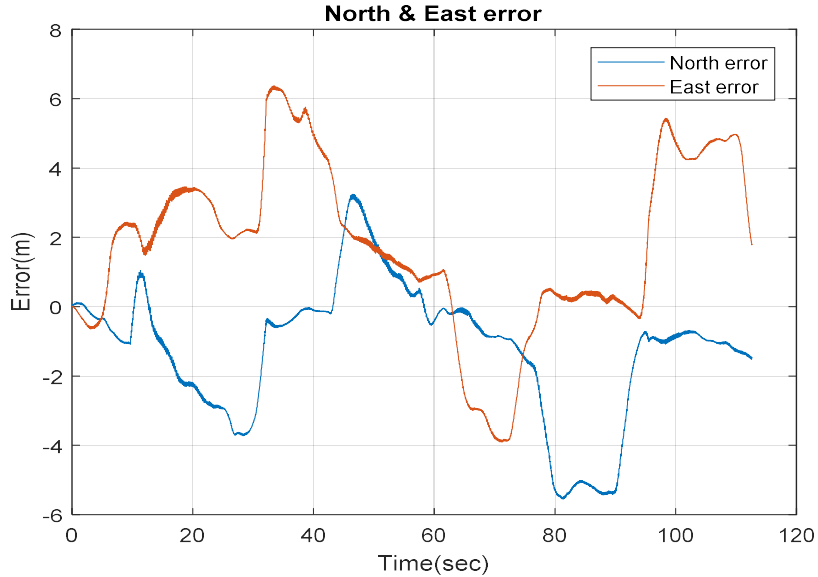


Figure 7-17: The North and East errors, which are obtained from the proposed integrated system aided navigation system during the GNSS outage period.

Figure 7-18 shows a comparison between the estimated 2D flight trajectory outage segments from the GNSS/INS integration (ground truth segment), and INS in standalone mode during the first flight for 30 secs of GNSS signal outage. Figure 7-19 illustrates the navigation errors for the INS in stand-alone mode in the North and East directions during 30 secs of GNSS signal outage.

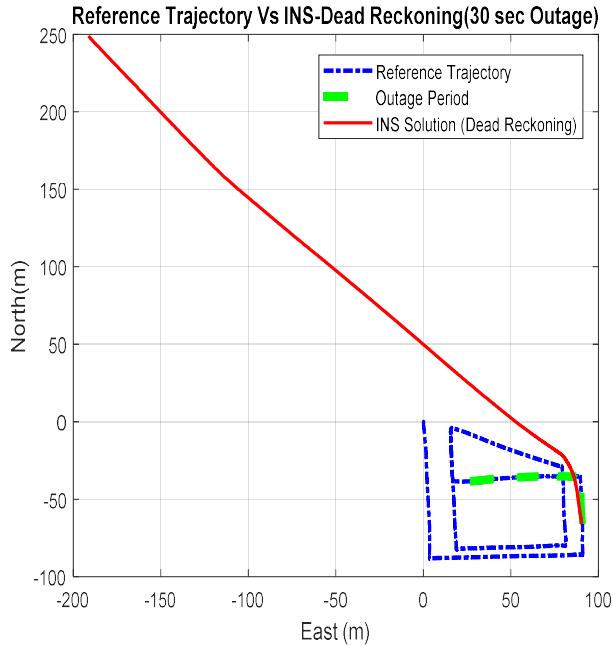


Figure 7-18: A comparison between the estimated 2D flight trajectory outage segments from the GNSS/INS integration (ground truth segment), and INS in standalone mode during 30 sec of GNSS signal outage.

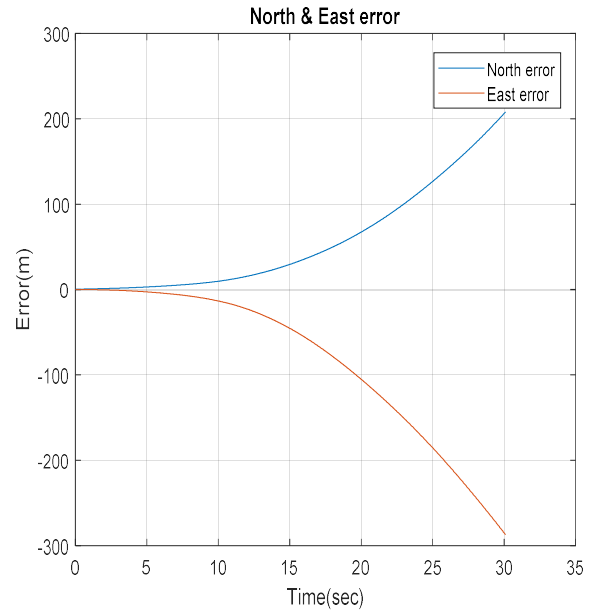


Figure 7-19: The North and East errors which are obtained from the INS/Mag/Baro in standalone mode during the GNSS outage period.

The following table provides a comparison of the RMS errors values for the position states which are obtained from the INS in standalone mode, and enhanced monocular VO, and the proposed integrated system aided navigation during the GNSS outages periods. The results demonstrate the ability of the proposed integrated system to reduce the 3D positioning errors to 2.06% during 30 secs, and 0.13% during 113 secs of the INS drift errors in standalone mode during the GNSS signals outages period.

Table 7-1: Comparison between (RMS errors) values for the position states obtained from (INS), enhanced monocular VO aided navigation, and the integrated system aided navigation with respect to the ground truth values.

		First Flight	
		(30 sec)	(113 sec)
		Outage	Outage
North Error (m)	INS	38.06	2002
	Enhanced monocular VO aided navigation	1.52	2.64
	Integrated system aided navigation	0.85	1.87
East Error (m)	INS	54.59	1436
	Enhanced monocular VO aided navigation	0.85	4.02
	Integrated system aided navigation	0.98	2.47
Height Error (m)	INS	5.08	221
	Enhanced monocular VO aided navigation	0.25	0.61
	Integrated system aided navigation	0.45	0.74
3D Position Error (m)	INS	66.74	2473
	Enhanced monocular VO aided navigation	1.75	4.84
	Integrated system aided navigation	1.37	3.18
Enhancement Percentage	Enhanced monocular VO aided navigation	97.36	99.80
from the INS%	Integrated system aided navigation	97.94	99.87

Figure 7-20 shows a comparison between the RMS of the 3D positioning errors for the proposed integrated system aided navigation during three GNSS outage periods ranged from 30 secs to 113 secs.

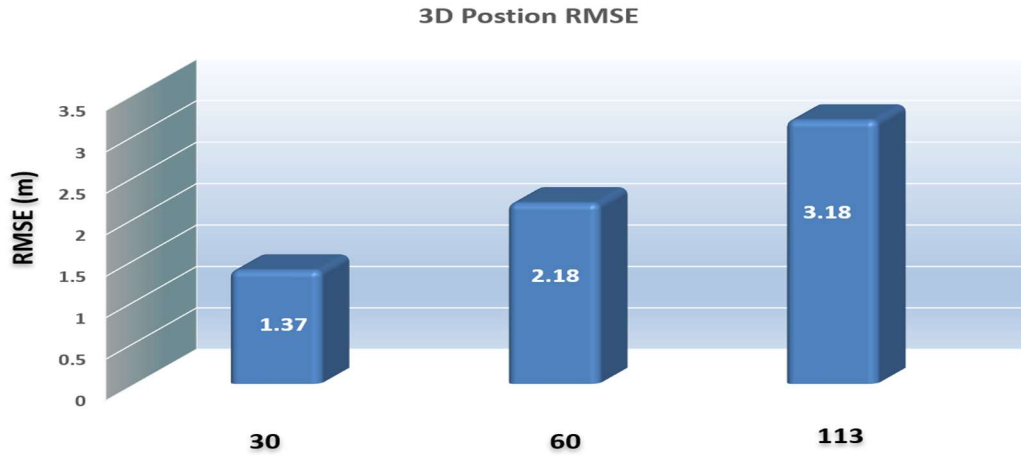


Figure7-20: RMS 3D positioning errors for the proposed integrated system aided navigation system during different outage periods.

The results also demonstrate the proposed integrated system aided navigation capability in reducing the 3D RMS positioning errors to 78.04%,71.65%, and 65.71% of the enhanced monocular VO and to 2.06%,0.43%, and 0.13% of the INS in standalone mode during 30,60, and 113 sec of GNSS signals outages respectively.

7.3.2 Second Experiment

The second flight composed of 18 waypoints of total flight time 393sec, with maximum speed of 5m/s as shown in Figure 7-21. In Figure 7-22, the estimated velocity from the typical closed form monocular VO, the enhanced monocular VO, and the RO are compared to the UAV reference forward velocity in the body frame with RMS error values of 0.61, 0.53, and 0.75 m/s respectively. The accuracy for the estimated velocity from the RO is slightly less than the monocular VO, and the enhanced monocular VO because the flight is performed over multiple objects with different altitudes, ranges, and angels inside the radar beam. The utilized radar doesn't provide azimuth and elevation measurements for the observed objects which have different angles values inside the radar beam and the radar tilting angel (60 degree) is the only angle that utilized to estimate the

vehicle forward velocity from each detected object. Therefore, the accuracy of the estimated forward velocity from the RO is downgraded while flying over non-flat terrain.

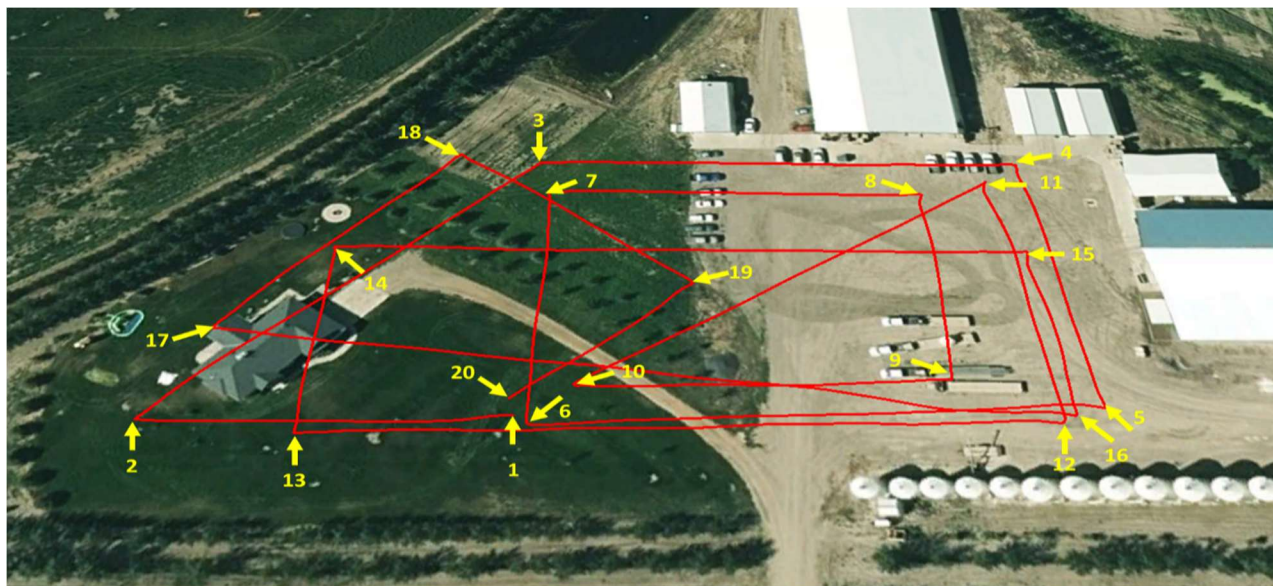


Figure 7-21: Second flight trajectory.

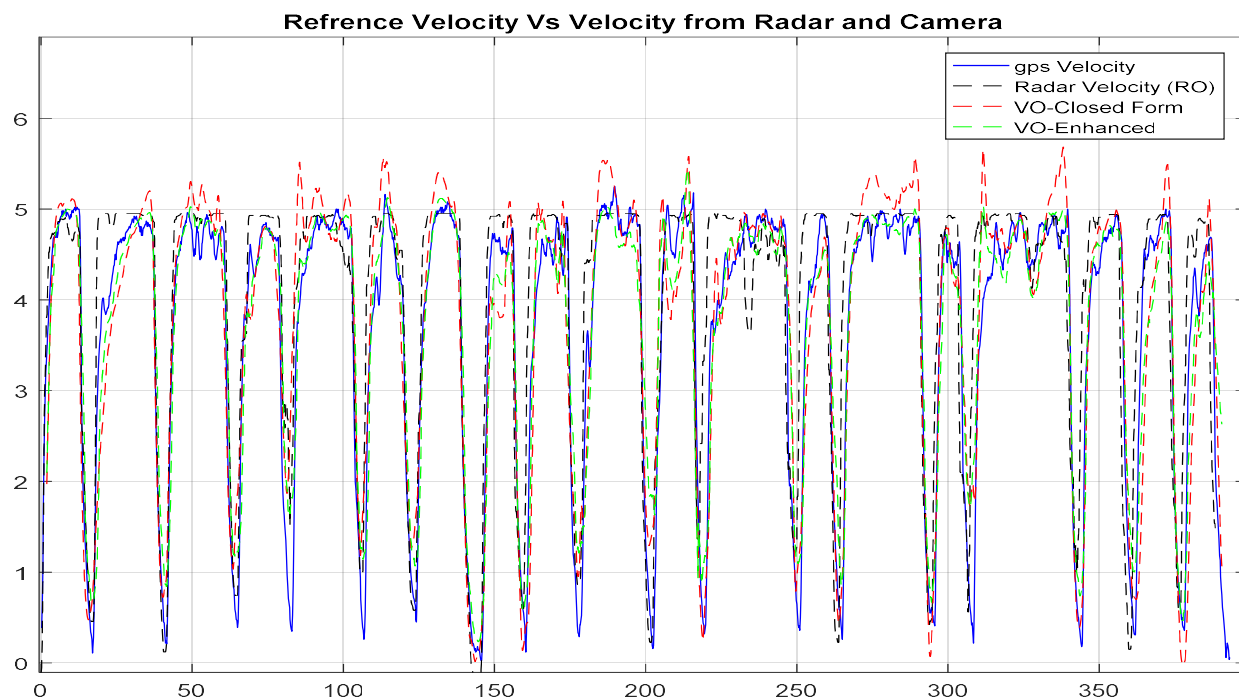


Figure 7-22: Comparison between forward ground truth velocity in the body frame, which is obtained from (GNSS/INS) integration, estimated velocity from the RO, the typical VO, and the enhanced VO.

The standard division of the estimated forward velocity from the enhanced VO and the RO are 0.073 and 0.075 m/s respectively while the barometer and the magnetometer standard divisions are 0.5 m and 5 degrees respectively. Four GNSS signal outage scenarios were carried, with different outage periods, ranging from 60sec to 240 sec. outage scenarios were carried, with different outage periods, ranging from 60sec to 240 sec.

The first outage period is performed for 60 sec. Figures 7-23 and 7-24 show a comparison between the estimated 2D flight trajectory outage segments from the GNSS/INS integration (ground truth segment), and enhanced monocular VO aided navigation during the second flight for 60 and 240 secs of GNSS signal outage respectively. Figures 7-25 and 7-26 show a comparison between the estimated 2D flight trajectory outage segments from the GNSS/INS integration (ground truth segment), and the proposed integrated system aided navigation during the second flight for 60 and 240 secs of GNSS signal outage respectively. Figure 7-27 demonstrates the ability of the proposed system (RO/enhanced monocular VO/mag/barometer) to mitigate the INS drift errors when the GNSS signals get lost, and to enhance the 3D RMSE positioning accuracy to be 5.38m in 240 secs.

Reference Trajectory Vs INS/VO(Enhanced)/Mag/Barometer integration(60 sec Out

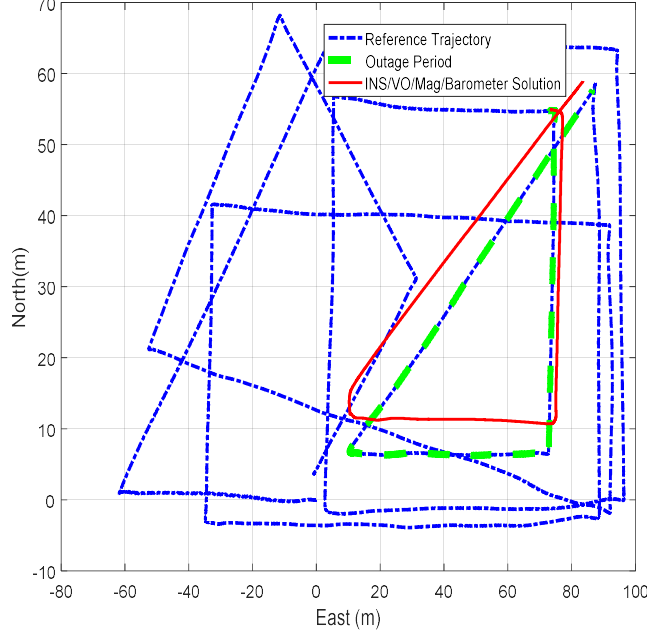


Figure 7-23: A comparison between the estimated 2D flight trajectory outage segments from the GNSS/INS integration (ground truth segment), and the enhanced monocular VO aided navigation system for 60 sec.

Reference Trajectory Vs INS/VO(Enhanced)/Mag/Barometer integration(240 sec Outage)

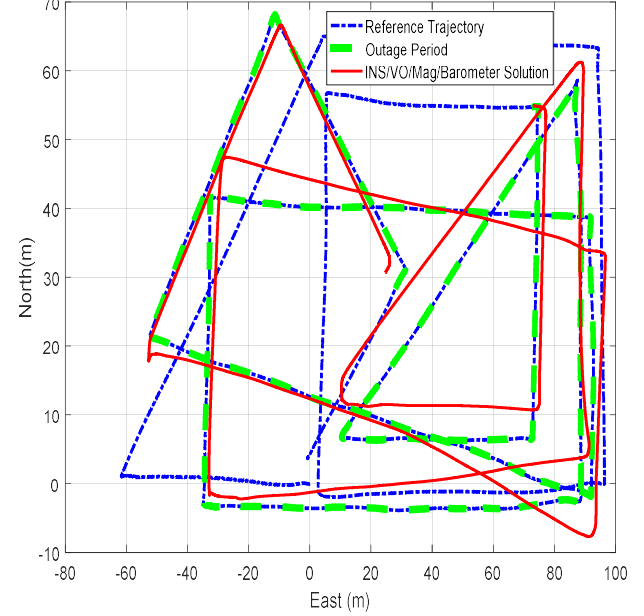


Figure 7-24: A comparison between the estimated 2D flight trajectory outage segments from the GNSS/INS integration (ground truth segment), and the enhanced monocular VO aided navigation system for 240 sec.

Reference Trajectory Vs INS/VO/RO/Mag/Barometer integration(60 sec Outag

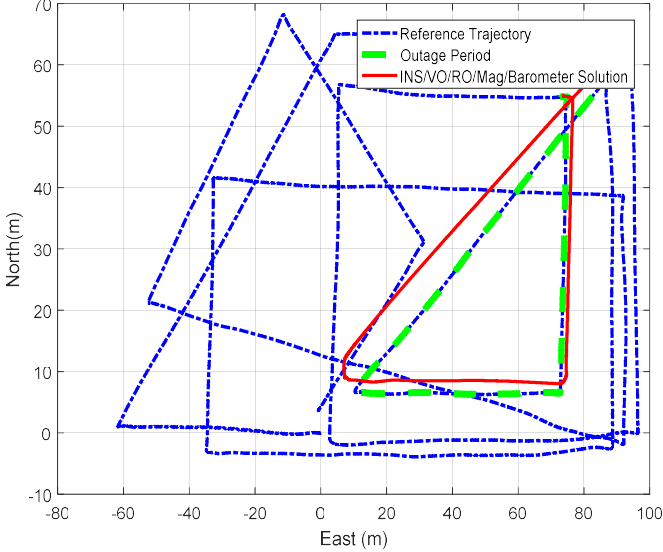


Figure 7-25: A comparison between the estimated 2D flight trajectory outage segments from the GNSS/INS integration (ground truth segment), and the proposed integrated system aided navigation system for 60 sec.

Reference Trajectory Vs INS/VO/RO/Mag/Barometer integration(240 sec Outage)

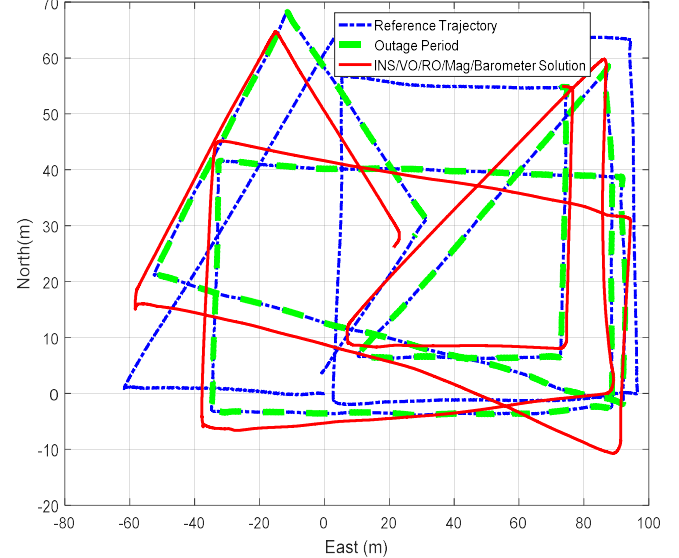


Figure 7-26: A comparison between the estimated 2D flight trajectory outage segments from the GNSS/INS integration (ground truth segment), and the proposed integrated system aided navigation system for 240 sec.

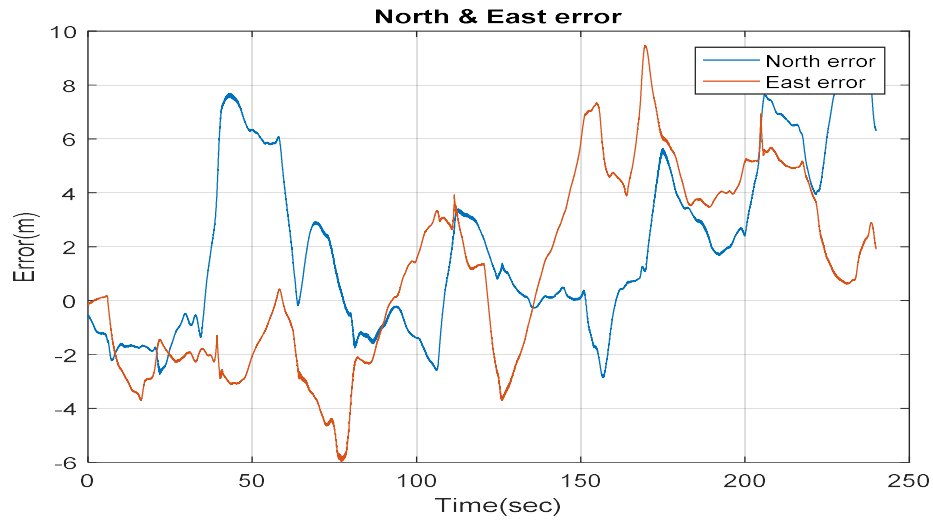


Figure 7-27: The North and East errors, which is obtained from the proposed integrated system aided navigation system during the GNSS outage period.

Figure 7-28 shows a comparison between the estimated 2D flight trajectory outage segments from the GNSS/INS integration (ground truth segment), and INS in standalone mode during the second flight for 60 secs of GNSS signal outage. Figure 7-29 illustrates the navigation errors for the INS in stand-alone mode in the North and East directions during 60 secs of GNSS signal outage.

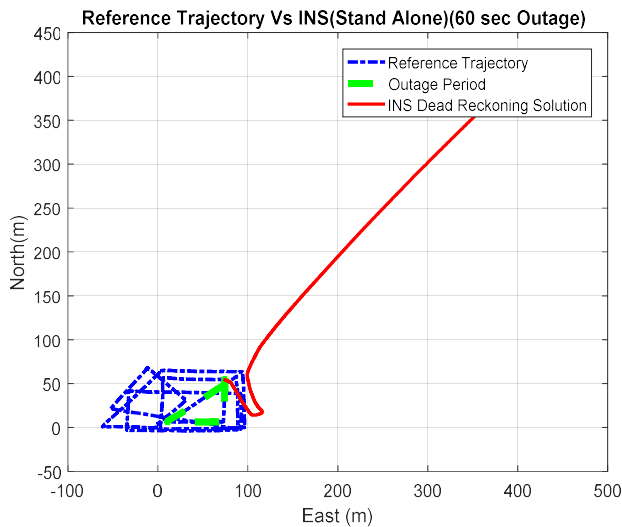


Figure 7-28: A comparison between the estimated 2D flight trajectory outage segments from the GNSS/INS integration (ground truth segment), and INS in standalone mode during 60 sec of GNSS signal outage.

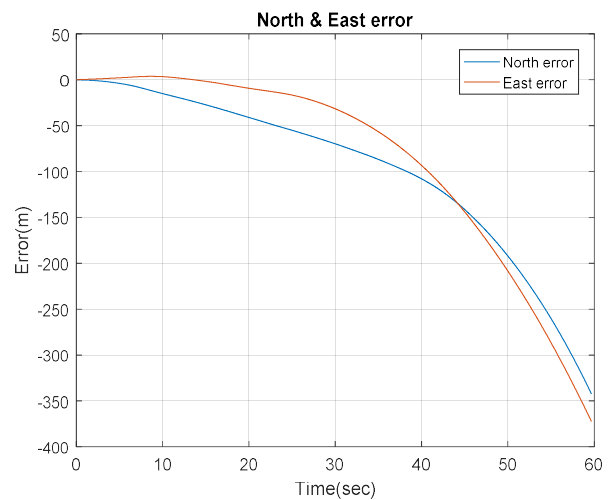


Figure 7-29: The North and East errors which are obtained from the INS/Mag/Baro in standalone mode during the GNSS outage period.

The following table provides a comparison of the RMS errors values for the position states which are obtained from the INS in standalone mode, and enhanced monocular VO, and the proposed integrated system aided navigation during the GNSS outages periods. The results demonstrate the ability of the proposed integrated system to reduce the 3D positioning errors to 3.09 % during 60 secs, and 0.1% during 240 secs of the INS drift errors in standalone mode during the GNSS signals outages period.

Table 7-2: Comparison between (RMS errors) values for the position states obtained from (INS), enhanced monocular VO aided navigation, and the integrated system aided navigation with respect to the ground truth values.

		Second Flight	
		(60 sec)	(240 sec)
		Outage	Outage
North Error (m)	INS	50.95	1233
	Enhanced monocular VO aided navigation	1.29	2.63
	Integrated system aided navigation	1.57	2.75
East Error (m)	INS	52.76	5680
	Enhanced monocular VO aided navigation	1.63	2.85
	Integrated system aided navigation	0.85	2.81
Height Error (m)	INS	12.45	878
	Enhanced monocular VO aided navigation	1.35	3.53
	Integrated system aided navigation	1.44	3.68
3D Position Error (m)	INS	74.39	5878
	Enhanced monocular VO aided navigation	2.47	5.24
	Integrated system aided navigation	2.29	5.38
Enhancement Percentage from the INS%	Enhanced monocular VO aided navigation	96.66	99.91
	Integrated system aided navigation	96.91	99.90

Figure 7-31 shows a comparison between the RMS of the 3D positioning errors for the proposed integrated system aided navigation during four GNSS outage periods ranged from 60 secs to 240 secs.

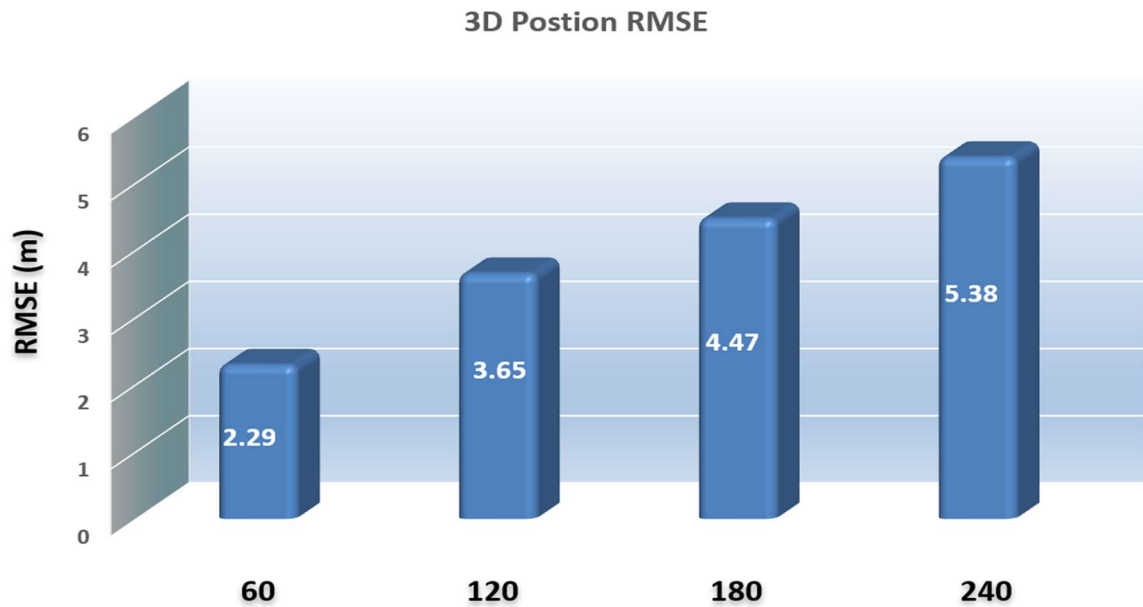


Figure 7-31: RMS 3D positioning errors for the proposed integrated system aided navigation system during different outage periods.

The results demonstrate the proposed integrated system aided navigation capability in reducing the 3D RMS positioning errors to 92.53 %, 99.41%, and 92.38% of the enhanced monocular VO during 60, 120, and 180 sec of GNSS signals outages respectively, while it has approximately the same accuracy as the enhanced monocular VO during 240sec. The results also show the proposed system ability of reducing the 3D RMS positioning errors to 3.09%, 0.48%, 0.17 %, and 0.1% of the INS in standalone mode during 60, 120, 180, and 240 secs of GNSS signals outages respectively.

7.4 Summary

A novel integrated navigation system-based approach is proposed to enhance the positioning accuracy and reliability of the navigation solution during GNSS outage periods for UAVs. A GoPro HERO4 Black camera and a micro FMCW radar have been mounted on the SOLO quadcopter. The FMCW radar provides the range Doppler map measurements of the received signals from the ground objects. This range Doppler map is then utilized to estimate the vehicle height and forward velocity from the detected targets. An efficient target detection is proposed based on a Gaussian kernel and locale maxima. The Gaussian kernel is convolved with the RDM to obtain the candidate targets while the local maxima is then applied to select the strongest candidates. An optical flow-based approach is utilized to implement the monocular VO. The vehicle rotational motion effect is compensated from the optical flow vectors. The VO scale ambiguity is resolved by utilizing the estimated radar height. This monocular VO is then enhanced with a learnt regression trees to compensate its estimated forward velocity drift errors. This regression trees algorithm is trained upon the availability of the GNSS signals. The estimated velocities from the regression trees and the monocular VO are weighted averaged to enhance the accuracy of the estimated velocity.

The estimated forward velocity from RO, enhanced VO, magnetometer, and barometer measurements are then fused with the INS in an EKF during the GNSS signal outage.

The proposed system is evaluated through two-real flights data with different maneuvers. To assess the proposed system's performance, three outages are performed in the first flight while four outages are carried out during the second flight. The results clearly indicate that the proposed integrated system aided navigation can aid the INS during GNSS signal outage. It also

demonstrates its capability of enhancing the average 3D positioning accuracy by 98.65% for the first flight, and 99.04% for the second flight with respect to the INS in standalone mode. In addition, it improves the average 3D positioning accuracy by 28.21% for the first flight, and 4.72% for the second flight with respect to the enhanced monocular VO.

Chapter Eight: **Conclusions, Contributions, and Future Work**

8.1 Research Contributions

The aim of our research is to develop a multi-sensor navigation system for navigation of small and micro UAVs in GNSS denied environments with the overall objectives (a) to mitigate the accumulated inertial sensor drift errors during the GNSS signals outages and (b) to provide a more robust navigation solution. A variety of aiding sensors and algorithms have been explored to implement a reliable navigation system for UAVs in GNSS denied environment. Such integrated system is capable of handling different environmental challenges such as rain, fog, dust, illumination, and featureless area.

The main contributions of this research are:

1. Design, development, and evaluation of a monocular VO algorithm which can reduce the accumulation of INS drift errors during GNSS signals outages. Moreover, this system can resolve the monocular VO scale ambiguity based on a learnt regression trees model. Since the UAVs may performing many missions during the day (e.g. for firefighting and rescue), the camera and system calibration parameters can change from one flight to another or even during the same flight. Therefore, the training process is performed in an online fashion during the flight to implicitly capture the most recent changes on those calibration parameters and to eliminating the need for a calibration phase. The employed regression trees can deal with the missing optical flow vectors in some image parts due to texture problems such as lack of features or rejected inconsistent matches caused by repeated patterns.
2. Design, development, and evaluation of GPR based approach for enhancing the INS positioning accuracy and reliability during GNSS signals outages. In this approach, an EKF

is enhanced with a GPR algorithm to model the INS drift errors upon the availability of the GNSS signals and to correct them when the GNSS signal is lost.

3. In order to meet the needs of UAVs applications, an accurate and reliable navigation solution is required. Although different aiding sensors such as camera have been previously proposed in an attempt to reduce the effect of the INS drift errors, the 3D positioning accuracy by using these techniques is still affected by some factors such as the lack of the observed features, incorrect matches, and the accumulated positioning drift errors. In this thesis, a novel smart hybrid vision aided INS is proposed to reduce the effect of such challenges by predicting both monocular VO drift and INS drift based on trained GPR against GNSS reference data. The proposed approach has a real-time training performance since the monocular VO, GPR for INS and, GPR for monocular VO training times are 0.027, 0.018, and, 0.012 s respectively for a one minute of collected data. Such computational performance allows a real-time and incremental training of the employed GPRs whenever the GNSS is available as reference to enhance the learnt GPR and capture the recent and new drift behaviors over time. In contrary to many other machine learning drift prediction approaches, the employed GPR can provide both predictions and their associated uncertainties to be utilized to assess the quality of the GPRs predicted states and to decide when these corrections are applied to the monocular VO and INS outputs and when are discarded. Unlike many other approaches that depend on a priori collected data for the training purpose, the proposed training process can take place during the flight upon availability of reference GNSS data. This feature enables the system to capture the effect of sensor parameter changes from flight to another as it allows using the most recent data for training.

4. Design, development, and evaluation of light weight RO aided navigation system for UAVs that has the ability to accurately detect the forward vehicle speed based on adaptive thresholding target detection technique to identify the main ground target and avoid the clutters. In addition, the proposed algorithm has a real-time performance since the target detection processing time is around 1 ms. Unlike other radar aided navigation systems that rely on artificial reflectors even for detecting or tracking the targets, the proposed RO benefits from ground scatterers such as grass, trees or any other objects in the surrounding environment, to aid the navigation during the GNSS signal outage. Unlike visual sensors which are affected by the environmental changes and featureless areas, these radars are immune to environmental changes such as illumination, rain, fog and dust and they are not affected by the featureless areas. Finally, the results in this chapter demonstrate the system's ability to mitigating the MMES IMU drift errors in a real flight data.
5. Design, development, and evaluation of a novel integrated navigation system based on a micro FMCW radar and a GoPro HERO4 Black camera for enhancing the 3D positioning accuracy of UAVs in GNSS denied environments. integrated GNSS denied environment navigation system for UAVs is proposed based on micro FMCW radar and a single camera. The vehicle forward velocity is estimated from both RO and the enhanced VO to enhance the INS navigation accuracy during GNSS signals outages. In addition, the estimated height from the RO is utilized to resolve the monocular VO scale ambiguity. An efficient target detection approach is proposed to detect the ground objects based on a Gaussian kernel and local maxima algorithms. These detected targets are then utilized to estimate the forward velocity and the height above ground level for the vehicle. An optical flow and regression trees-based approaches are utilized to implement the enhanced monocular VO. The optical flow is

employed for the forward velocity estimation purpose while its associated drift errors are compensated based on a trained regression trees model. These estimated forward velocities from the RO and enhanced VO are then fused with the IMU, barometer, and magnetometer measurements via an EKF. The experimental results demonstrate the proposed system's ability to enhance the average 3D positioning errors for the first flight to 98.65%, and for the second flight to 99.04% of the INS drift errors in a standalone mode during the GNSS signal outage. In addition, it improves the average 3D positioning accuracy by 28.21% for the first flight, and 4.72% for the second flight with respect to the enhanced monocular VO. Unlike other proposed RO works which utilized a large unmanned aircraft or large radar or even simulating the flight missions, the proposed system utilizes a small SOLO quadcopter and a light weight micro radar during a real flight. Such small quadcopters are typically utilized in many missions such as search, rescue, and disaster management. The proposed algorithm has been evaluated in a generic and typical maneuvering scenario. It also avoids the various assumptions imposed by many other researches such as straight flight, constant velocity, leveled flight, and flying over flat terrain. The incorporation of the RO and VO into one integrated system help toward handling the limitations of each one of them. The proposed RO provides a more accurate forward velocity estimation than the enhanced monocular VO while flying over flat terrain but slightly worse otherwise. On the other hand, the radar is immune against the environmental changes and can operate in featureless areas.

8.2 Conclusions

There have been extensive market demands over the past 10 years for deploying small autonomous UAVs in enormous civil and military applications such as search and rescue, disaster management, firefighting, reconnaissance and border mentoring. While UAVs are performing their missions in such cluttered environments, they are typically relying on the onboard GNSS/INS integrated measurements for the positioning and localization purpose. During such challenging missions, the GNSS signals could be blocked or suffer from attenuation, multipath effect, jamming and spoofing. In such complicated scenarios, the navigation solution is acquired by the INS in standalone mode prior to the GNSS signals recovery. Consequently, the navigation solution will deteriorate rapidly because of the drift exhibited by the low-cost INS during this outage period. Therefore, employment of another aiding sensor has a vital role in mitigating the accumulated drift errors associated with INS measurements while losing the GNSS signals.

Cameras have small size, light weight, low power consumption and ability to provide useful measurements in term of color and texture that can be used to enhance the navigation solution during the GNSS outages periods, their imagery measurements are affected by brightness, lighting conditions and featureless areas. Due to low cost and small size of monocular VO, it has been widely utilized in many navigation and mobile mapping applications. Despite these advantages for the monocular VO, it still suffers from scale ambiguity, which can force the navigation solution to drift rapidly with time.

Radars have the capability of avoiding cameras limitation factors since they are not affected by environmental changes. Although theses radars have such great benefit, the noisy and cluttered measurements affect their performance.

Therefore, this research work proposed a multi-sensor navigation system in GNSS denied environment which is capable of handling such challenges and reducing their effects. Furthermore, the proposed system enhances the 3D positioning accuracy during GNSS signal outages.

In Chapter 3, the proposed monocular VO system was introduced with the main aim to reduce the INS drift errors during GNSS signal outages. Furthermore, the calibration phase has been eliminated since the proposed system inherently models the interior camera parameters, its lever arm and boresight parameters during the training session. The implemented algorithm has the ability of resolving the scale ambiguity problem. Regression trees is utilized to generate the underlying function that maps the optical flow parameters to the desired output (velocity increment). The employment of such algorithm contributes in predicting the vehicle velocity even with the partial availability of optical flow vectors. This feature is of great help to handle the situations where the optical flow vectors are missing in some image parts due to texture problems such as lack of features or rejected inconsistent matches caused by repeated patterns. The proposed system performance is evaluated through two outage periods. The results show that the proposed algorithm enhanced the 3D position errors to 47% of the INS drift errors in standalone mode during the GNSS signal outage period.

In Chapter 4, a GPR-based approach was introduced to model the INS main trend drift errors (due to biases errors) when the GNSS signal is available and to predict and compensate the mechanization output states (velocity and orientation) during GNSS signal outages. Three artificial outages are carried out to evaluate the performance of the proposed algorithm. The results indicate the effectiveness of the proposed algorithm in enhancing the average INS 3D positioning errors to

46.7% of the average INS drift errors in standalone mode during the GNSS signal outage even with a short training period.

In Chapter 5, a novel smart hybrid vision aided INS is proposed based on the main idea of optical flow-based for vision-aided INS using regression trees (chapter 3). The proposed algorithms in chapter 3 and 4 are merged and developed to form the proposed smart hybrid system in this chapter. The 3D positioning accuracy of the proposed monocular VO in chapter 3 is still affected by some factors such as the lack of the observed features, incorrect matches and the accumulated positioning drift errors. Therefore, the smart hybrid algorithm is developed to reduce the effect of such limitations and to provide a more accurate and reliable navigation solution during GNSS signal outages. An airborne dataset is used to assess the proposed system performance. The experiments results demonstrated the ability of smart hybrid VAINS for enhancing the 3D RMS positioning errors to 61.5%, and 32.4% of monocular VO/INS integration, and monocular VO/INS integration enhanced with the INS drift predictor during GNSS signal outages even with a short learning period, respectively.

In Chapter 6, a fusion between RO/Magnetometer/Barometer is proposed to aid the INS during GNSS signal outages was introduced. The main contributions of the proposed framework are its ability to accurately detect the forward vehicle speed based on a new adaptive thresholding target detection technique, which participates in providing a more accurate and reliable navigation solution during GNSS signal outages. While many of the proposed RO solutions assume different assumptions about the vehicle navigation states, the proposed solution does not make such assumptions and provides a generic enhancement to the navigation solution under the typical maneuvering scenarios. In addition, the proposed algorithm has a real-time performance since the

target detection processing time is around 1 ms. Unlike other radar aided navigation systems that rely on artificial reflectors even for detecting or tracking the targets, the proposed RO benefits from ground scatterers such as grass, trees or any other objects in the surrounding environment, to aid the navigation during the GNSS signal outage. Finally, the experimental results demonstrate the proposed system's ability to enhance the average 3D positioning errors for the first flight to 99.78%, and for the second flight to 99.67% of the INS drift errors in a standalone mode during the GNSS signal outage.

In Chapter 7, An integrated GNSS denied environment navigation system for UAVs is proposed based on a micro FMCW radar and a GoPro HERO4 Black camera. The vehicle forward velocity is estimated from both RO and the enhanced VO to enhance the INS navigation accuracy during GNSS signals outages. In addition, the estimated height from the RO is utilized to resolve the monocular VO scale ambiguity. An efficient target detection approach is proposed to detect the ground objects based on a Gaussian kernel and local maxima algorithms. These detected targets are then utilized to estimate the forward velocity and the height above ground level for the vehicle. An optical flow and regression trees-based approaches are utilized to implement the enhanced monocular VO. The optical flow is employed for the forward velocity estimation purpose while its associated drift errors are compensated based on a learnt regression trees model. These estimated forward velocities from the RO and enhanced VO are then fused with the IMU, barometer, and magnetometer measurements via an EKF. Finally, the experimental results demonstrate the proposed system's ability to enhance the average 3D positioning errors for the first flight to 98.65%, and for the second flight to 99.04% of the INS drift errors in a standalone mode during the GNSS signal outage. In addition, it improves the average 3D positioning errors by 28.21% for the first flight, and 4.72% for the second flight with respect to the enhanced

monocular VO. The incorporation between the radar and the camera help toward handle the limitations of each one of them individually since the radar is immune against the environmental and illuminations changes, and the camera can assist the radar while flying over non-flat terrain. The results also demonstrate the proposed system ability to enhance the 3D RMSE positioning accuracy of the low cost MPU 6000 IMU (less than 10\$) to be 5.38m during a long GNSS signals outage period (240 secs). The performance of the proposed integrated system is expected to be enhanced while mount it on a fixed wing UAV, since it is typically flying on a higher altitudes than the utilized quadcopter which allows for observing more features with the camera and minimizing the effect of non flat-terrain on the utilized radar measurements.

8.3 Future Work

The proposed works in this thesis can be extended and developed based in the following suggestions:

1. Extended the proposed VO to estimate the vehicle attitudes.
2. Extended the proposed RO to detect, track, and localize ground objects when the GNSS signal is available and utilize them to re-localize the vehicle position during the GNSS signal outage.
3. Exploits the radar ground scatterers geometry (arc) to estimate the roll and pitch which can contribute in enhancing the attitude accuracy. In addition, this geometry can be utilized to obtain the forward velocity from the terrain and to exclude any other objects.
4. Calibrate the camera with radar field of view to estimate accurately the depth of each pixel on the observed image from the radar measurements. This system configuration can be useful for accurate mobile mapping and navigation applications.

The proposed integrated system on chapter 7 could be utilized for many applications such as search, rescue, and surveillance since it is capable of providing a 5 m 3D positioning accuracy as same as the single point GNSS for long period of GNSS signals outages (4 min). Such performance is sufficient to be used for these applications. This integrated navigation system could also be mounted on a fixed wing UAVs. These UAVs can fly at higher altitudes which could be utilized for mapping purposes. On the near future, autonomous flying cars could be utilized as a transportation means. The necessity for accurate and reliable navigation system against different environmental conditions for such cars is essential. Therefore, the utilization of the proposed integrated system could be helpful on such applications.

References

- R. N. White, "Airborne Doppler Radar Navigation of Jet Transport Aircraft," IRE Trans. Aerosp. Navig. Electron., vol. ANE-9, no. 1, pp. 11–20, Mar. 1962.
- [2] E. B. Quist and R. W. Beard, "Radar odometry on fixed-wing small unmanned aircraft," IEEE Trans. Aerosp. Electron. Syst., vol. 52, no. 1, pp. 396–410, Feb. 2016.
- [3] J. J. Leonard and H. F. Durrant-Whyte, "Mobile robot localization by tracking geometric beacons," IEEE Trans. Robot. Autom., vol. 7, no. 3, pp. 376–382, Jun. 1991.
- [4] D. Kurth, G. Kantor, and S. Singh, "Experimental results in range-only localization with radio," in Proceedings 2003 IEEE/RSJ International Conference on Intelligent Robots and Systems (IROS 2003) (Cat. No.03CH37453), 2003, vol. 1, pp. 974–979 vol.1.
- [5] M. U. de Haag, A. Vadlamani, J. L. Campbell, and J. Dickman, "Application of laser range scanner based terrain referenced navigation systems for aircraft guidance," in Third IEEE International Workshop on Electronic Design, Test and Applications (DELTA'06), 2006, p. 6 pp.-274.
- [6] El-Sheimy, N. (2012). "Inertial techniques and INS/DGPS Integration." Lecture Notes ENGO 623. Department of Geomatics Engineering, the University of Calgary, Canada.
- [7] Barbour, N. M. (2004). "Inertial navigation sensors." NATO RTO Lecture Series 232(5): 5.2.
- [6] A. Waxman, J. LeMoigne, L. Davis, B. Srinivasan, T. Kushner, E. Liang, and T. Siddalingaiah "A visual navigation system for autonomous land vehicles," IEEE J. Robot. Autom., vol. 3, no. 2, pp. 124–141, Apr. 1987.
- [7] E. Feuerstein, H. Safran, and P. N. James, "Inaccuracies in Doppler Radar Navigation Systems Due to Terrain Directivity Effects, Nonzero Beamwidths and Eclipsing," IEEE Trans. Aerosp. Navig. Electron., vol. ANE-11, no. 2, pp. 101–111, Jun. 1964.
- [8] A. K. Vadlamani and M. U. de Haag, "Improved downward-looking terrain database integrity monitor and terrain navigation," in 2004 IEEE Aerospace Conference Proceedings (IEEE Cat. No.04TH8720), 2004, vol. 3, p. 1607 Vol.3.
- [9] A. K. Vadlamani and M. U. de Haag, "Flight test results of loose integration of dual airborne laser scanners (DALs)/INS" IEEE Conference Publication [Online]. Available: [Accessed: 01-Nov-2017].

- [10] A. Alcocer, P. Oliveira, A. Pascoal, and J. Xavier, Estimation of Attitude and Position from Range-Only Measurements using Geometric Descent Optimization on the Special Euclidean Group. In: Information Fusion, 2006 9th International Conference on. IEEE, 2006. p. 1-8.
- [11] Hall, D. Timothy, C. Counselman III, and N. Misra. "Radiolocation Using AM Broadcast Signals: Positioning Performance,," [Online]. Available: <https://www.ion.org/publications/abstract.cfm?articleID=2097>. [Accessed: 09-Mar-2017].
- [12] D. I. Vilaseca and J. I. Giribet, "Indoor navigation using WiFi signals," in 2013 Fourth Argentine Symposium and Conference on Embedded Systems (SASE/CASE), 2013, pp. 1–6.
- [13] Rabinowitz, M., Spilker, J.J., "The Rosum Television Positioning Technology," Proceedings of the 59th Annual Meeting of The Institute of Navigation and CIGTF 22nd Guidance Test Symposium (2003), Albuquerque, NM, June 2003, pp. 528-541.
- [14] Eggert, Ryan J., Raquet, John F., "Evaluating the Navigation Potential of the NTSC Analog Television Broadcast Signal," Proceedings of the 17th International Technical Meeting of the Satellite Division of The Institute of Navigation (ION GNSS 2004), Long Beach, CA, September 2004, pp. 2436-2446.
- [15] T. Layh, J. Larson, D. Gebre-Egziabher, B. Taylor, J. Jackson, and Y. Agamawi, "GPS-Denied Navigator for Small UAVs," 2014.
- [16] Raquet, John F., Miller, Mikel M., Nguyen, Thao Q., "Issues and Approaches for Navigation Using Signals of Opportunity," Proceedings of the 2007 National Technical Meeting of The Institute of Navigation, San Diego, CA, January 2007, pp. 1073-1080.
- [17] K. Kauffman, J. Raquet, Y. Morton, and D. Garmatyuk, "Real-Time UWB-OFDM Radar-Based Navigation in Unknown Terrain," IEEE Trans. Aerosp. Electron. Syst., vol. 49, no. 3, pp. 1453–1466, Jul. 2013.
- [18] "ARTECH HOUSE USA : Design and Analysis of Modern Tracking Systems." [Online]. Available: <http://us.artechhouse.com/Design-and-Analysis-of-Modern-Tracking-Systems-P170.aspx>. [Accessed: 01-Nov-2017].
- [19] E. B. Quist and R. W. Beard, "Radar odometry on fixed-wing small unmanned aircraft," IEEE Trans. Aerosp. Electron. Syst., vol. 52, no. 1, pp. 396–410, Feb. 2016.
- [20] R. O. Duda and P. E. Hart, "Use of the Hough transformation to detect lines and curves in

- pictures,” *Commun. ACM*, vol. 15, no. 1, pp. 11–15, 1972.
- [21] E. B. Quist, P. C. Niedfeldt, and R. W. Beard, “Radar odometry with recursive-RANSAC,” *IEEE Trans. Aerosp. Electron. Syst.*, vol. 52, no. 4, pp. 1618–1630, Aug. 2016.
 - [22] E. B. Quist and R. Beard, “Radar Odometry on Small Unmanned Aircraft,” 2013.
 - [23] A. F. Scannapieco, A. Renga, G. Fasano, and A. Moccia, “Ultralight radar sensor for autonomous operations by micro-UAS,” in *2016 International Conference on Unmanned Aircraft Systems (ICUAS)*, 2016, pp. 727–735.
 - [24] H. Rohling, “Radar CFAR Thresholding in Clutter and Multiple Target Situations,” *Aerosp. Electron. Syst. IEEE Trans. On*, vol. 19, pp. 608–621, Aug. 1983.
 - [25] S. Banerjee and A. Roy, *Linear algebra and matrix analysis for statistics*. CRC Press, 2014.
 - [26] K. Konolige and M. Agrawal, “FrameSLAM: From Bundle Adjustment to Real-Time Visual Mapping,” *IEEE Trans. Robot.*, vol. 24, no. 5, pp. 1066–1077, Oct. 2008.
 - [27] K. Konolige, M. Agrawal, and J. Solà, “Large Scale Visual Odometry for Rough Terrain,” 2007.
 - [28] K. Konolige, J. Bowman, J. D. Chen, P. Mihelich, M. Calonder, V. Lepetit, and P. Fua, “View-based Maps,” *Int J Rob Res*, vol. 29, no. 8, pp. 941–957, Jul. 2010.
 - [29] M. Achtelik, M. Achtelik, S. Weiss, and R. Siegwart, “Onboard IMU and monocular vision based control for MAVs in unknown in- and outdoor environments,” in *2011 IEEE International Conference on Robotics and Automation*, 2011, pp. 3056–3063.
 - [30] M. Blösch, S. Weiss, D. Scaramuzza, and R. Siegwart, “Vision based MAV navigation in unknown and unstructured environments,” in *2010 IEEE International Conference on Robotics and Automation*, 2010, pp. 21–28.
 - [31] M. Bryson, M. Johnson-Roberson, and S. Sukkarieh, “Airborne smoothing and mapping using vision and inertial sensors,” in *2009 IEEE International Conference on Robotics and Automation*, 2009, pp. 2037–2042.
 - [32] T. B. Karamat, R. G. Lins, S. N. Givigi, and A. Noureldin (2018). Novel EKF-Based Vision/Inertial System Integration for Improved Navigation. *IEEE Transactions on Instrumentation and Measurement*, 67, no. 1 (2018): 116-125.

- [33] J. Artieda et al., “Visual 3-D SLAM from UAVs,” *J Intell Robot. Syst*, vol. 55, no. 4–5, pp. 299–321, Aug. 2009.
- [34] A. Cherian, J. Andersh, V. Morellas, N. Papanikolopoulos, and B. Mettler, “Autonomous altitude estimation of a UAV using a single onboard camera,” in *2009 IEEE/RSJ International Conference on Intelligent Robots and Systems*, 2009, pp. 3900–3905.
- [35] J. Kelly and G. S. Sukhatme, “An experimental study of aerial stereo visual odometry,” *IFAC Proc. Vol.*, vol. 40, no. 15, pp. 197–202, Jan. 2007.
- [36] J. Civera, A. J. Davison, and J. M. Montiel, “Dimensionless Monocular SLAM,” in *Proceedings of the 3rd Iberian Conference on Pattern Recognition and Image Analysis, Part II*, Berlin, Heidelberg, 2007, pp. 412–419.
- [37] A. J. Davison, I. D. Reid, N. D. Molton, and O. Stasse, “MonoSLAM: Real-Time Single Camera SLAM,” *IEEE Trans. Pattern Anal. Mach. Intell.*, vol. 29, no. 6, pp. 1052–1067, Jun. 2007.
- [38] K.-C. Huang, S.-H. Tseng, W.-H. Mou, and L.-C. Fu, “Simultaneous localization and scene reconstruction with monocular camera,” in *2012 IEEE International Conference on Robotics and Automation*, 2012, pp. 2102–2107.
- [39] G. Klein and D. Murray, “Parallel Tracking and Mapping for Small AR Workspaces,” in *2007 6th IEEE and ACM International Symposium on Mixed and Enhanced Reality*, 2007, pp. 225–234.
- [40] D. Scaramuzza, F. Fraundorfer, and R. Siegwart, “Real-time monocular visual odometry for on-road vehicles with 1-point RANSAC,” in *2009 IEEE International Conference on Robotics and Automation*, 2009, pp. 4293–4299.
- [41] H. Strasdat, J. M. M. Montiel, and A. J. Davison, “Real-time monocular SLAM: Why filter?,” in *2010 IEEE International Conference on Robotics and Automation*, 2010, pp. 2657–2664.
- [42] S. Weiss, D. Scaramuzza, and R. Siegwart, “Monocular-SLAM-Based Navigation for Autonomous Micro Helicopters in GPS-denied Environments,” *J Field Robot*, vol. 28, no. 6, pp. 854–874, Nov. 2011.
- [43] G. Klein and D. Murray, “Parallel Tracking and Mapping for Small AR Workspaces,” in *2007 6th IEEE and ACM International Symposium on Mixed and Enhanced Reality*, 2007,

pp. 225–234.

- [44] D. Nistér, O. Naroditsky, and J. Bergen, “Visual odometry for ground vehicle applications,” *J. Field Robot.*, vol. 23, no. 1, pp. 3–20, Jan. 2006.
- [45] M. Pollefeys, D. Nistér, J. M. Frahm, A. Akbarzadeh, P. Mordohai, B. Clipp, and C. Salmi, “Detailed Real-Time Urban 3D Reconstruction from Video,” *Int J Comput Vis.*, vol. 78, no. 2–3, pp. 143–167, Jul. 2008.
- [46] O. Pizarro, R. Eustice, and H. Singh, “Large area 3D reconstructions from underwater surveys,” in *OCEANS ’04. MTS/IEEE TECHNO-OCEAN ’04*, 2004, vol. 2, p. 678–687 Vol.2.
- [47] M. Shahbazi, S. Gunho, T. Jérôme, and M. Patrick. “Robust structure-from-motion computation: Application to open-pit mine surveying from unmanned aerial images.” *Journal of Unmanned Vehicle Systems* 5, no. 4 (2017): 126-145.
- [48] D. Eynard, P. Vasseur, C. Demonceaux, and V. Frémont, “UAV altitude estimation by mixed stereoscopic vision,” in *2010 IEEE/RSJ International Conference on Intelligent Robots and Systems*, 2010, pp. 646–651.
- [49] H. Lategahn and C. Stiller, “City GPS using stereo vision,” in *2012 IEEE International Conference on Vehicular Electronics and Safety (ICVES 2012)*, 2012, pp. 1–6.
- [50] J. Rehder, K. Gupta, S. Nuske, and S. Singh, “Global pose estimation with limited GPS and long range visual odometry,” in *2012 IEEE International Conference on Robotics and Automation*, 2012, pp. 627–633.
- [51] Hu, J.S., Chang, Y.J., Hsu, Y.L, “Calibration and online data selection of multiple optical flow sensors for odometry applications”. *Sensors Actuators A Phys.* 149(1), 74–80 (2009)
- [52] Ross, R., Devlin, J., Wang, S, “Toward refocused optical mouse sensors for outdoor optical flow odometry”. *IEEE Sensors J.* 12(6), 1925–1932 (2012)
- [53] Barrows, G., Neely, C., Miller, K. “Fixed and flapping wing aerodynamics for micro air vehicle application”, vol.23, chap. OpticFlowSensorsforMAVNavigation, pp. 557–573. AIAA (2001)
- [54] Zufferey, J.C., Floreano, D, “Toward 30-gram autonomous indoor aircraft: vision-based obstacle avoidance and altitude control”, In: *Proceedings of the IEEE International Conference on Robotics and Automation*, pp. 2594–2599. Barcelona, Spain (2005)

- [55] Herisse, B., Hamel, T., Mahony, R., Russotto, F.X., “Landing a VTOL unmanned aerial vehicle on a moving platform using optical flow”. IEEE Trans. Robot. 28(1), 77–89 (2012)
- [56] Lucas, B.D., Kanade, T., “An iterative image registration technique with an application to stereo vision”, In: Proceedings of the 1981 DARPA Image Understanding Workshop (1981)
- [57] Horn, B.,Schunck, B, “Determining optical flow”, Artif. Intell.17, 185–203 (1981).
- [58] H. Bay, A. Ess, T. Tuytelaars, and L. Van Gool, “Speeded-Up Robust Features (SURF),” Comput. Vis. Image Underst., vol. 110, no. 3, pp. 346–359, Jun. 2008.
- [59] G. Conte P. Doherty, “An integrated UAV navigation system based on aerial image matching”, IEEE Aerospace Conf., Big Sky, March 2008.
- [60] S. Saripalli, J.F. Montgomery, G. Sukhatme, “Visually guided landing of an unmanned aerial vehicle”, IEEE T-RA, 19(3):371-380, 2003.
- [61] G. Anitha, R.N. Gireesh Kumar, “Vision based autonomous landing of an unmanned aerial vehicle”, Procedia Engineering, vol 38, 2012.
- [62] M. Csorba. Simultaneous Localisation and Map Building. PhD thesis, August 1997. 1, 9
- [63] R. C. Smith, M. Self, and P. Cheeseman. Estimating Uncertain Spatial Relationships in Robotics. In Autonomous robot vehicles, pages 167–193. 1990. 9
- [64] M. Montemerlo, S. Thrun, D. Koller, and B. Wegbreit. FastSLAM: A Factored Solution to the Simultaneous Localization and Mapping Problem. In Proceedings of the National conference on Artificial Intelligence, pages 593–598. Menlo Park, CA; Cambridge, MA; London; AAAI Press; MIT Press; 1999, 2002. 9
- [65] S. Thrun, Y. Liu, D. Koller, A. Y. Ng, Z. Ghahramani, and H. F. Durrant-Whyte. Simultaneous Localization and Mapping with Sparse Extended Information Filters. The International Journal of Robotics Research, 23(7-8):693–716, August 2004. 9
- [66] Guizilini, Vitor, and Fabio Ramos. "Visual odometry learning for unmanned aerial vehicles." Robotics and Automation (ICRA), 2011 IEEE International Conference on. IEEE, 2011.
- [67] T. A. Ciarfuglia, G. Costante, P. Valigi, and E. Ricci, “Evaluation of non-geometric methods

- for visual odometry,” *Robotics and Autonomous Systems*, vol. 62, no. 12, pp. 1717–1730, 2014.
- [68] K. Konda and R. Memisevic, “Learning visual odometry with a convolutional network,” in *Proceedings of International Conference on Computer Vision Theory and Applications*, 2015.
 - [69] A. Kendall, M. Grimes, and R. Cipolla, “Convolutional networks for real-time 6-DoF camera relocalization,” in *Proceedings of International Conference on Computer Vision (ICCV)*, 2015.
 - [70] G. Costante, M. Mancini, P. Valigi, and T. A. Ciarfuglia, “Exploring representation learning with CNNs for frame-to-frame ego-motion estimation,” *IEEE Robotics and Automation Letters*, vol. 1, no. 1, pp. 18–25, 2016.
 - [71] Clark, Ronald, S. Wang, H.Wen, A.Markham, and N. Trigoni. "VINet: Visual-Inertial Odometry as a Sequence-to-Sequence Learning Problem." *AAAI*. 2017.
 - [72] M. Warren, D. McKinnon, H. Hu, A. Glover, M. Shiel, B. Upcroft, "Large Scale Monocular Vision-only Mapping from a Fixed-Wing sUAS", in *International Conference on Field and Service Robotics*, Matsushima, Japan, 2012.
 - [73] C.Shen, Z.Bai , H.Cao , K.Xu, C.Wang, H.Zhang ,J.Liu. "Optical flow sensor/INS/magnetometer integrated navigation system for MAV in GPS-denied environment". *Journal of Sensors*. 2016.
 - [74] Shan, Mo, et al. "Google map aided visual navigation for UAVs in GPS-denied environment." 2015 *IEEE International Conference on Robotics and Biomimetics (ROBIO)*. IEEE, 2015
 - [75] Abdel-Hamid, Walid, Aboelmagd Noureldin, and Naser El-Sheimy. "Adaptive fuzzy prediction of low-cost inertial-based positioning errors." *IEEE Transactions on Fuzzy Systems* 15.3 (2007): 519-529.
 - [76] Noureldin, A., A. El-Shafie, and N. El-Sheimy. "Adaptive neuro-fuzzy module for inertial navigation system/global positioning system integration utilising position and velocity updates with real-time cross-validation." *IET Radar, Sonar & Navigation* 1.5 (2007): 388-396.
 - [77] Bhatt, Deepak, et al. "An enhanced mems error modeling approach based on nu-support vector regression." *Sensors* 12.7 (2012): 9448-9466.

- [78] Noureldin, Aboelmagd, Ahmed El-Shafie, and Mohamed Bayoumi. "GPS/INS integration utilizing dynamic neural networks for vehicular navigation." *Information Fusion* 12.1 (2011): 48-57.
- [79] Rasmussen, C.E., and Williams, C.: ‘Gaussian processes for machine learning’ (MIT Press, 2006).
- [80] Duvallet, F., and Tews, A.D.: ‘WiFi position estimation in industrial environments using Gaussian processes’. *IEEE/RSJ Int. Conf. on Intelligent Robots and Systems*, Nice, France, September 2008.
- [81] Atia, M. M., A. Noureldin, and M. Korenberg. "Gaussian process regression approach for bridging GPS outages in integrated navigation systems." *Electronics letters* 47.1 (2011): 52-53. Smith, J., 1987b. Economic printing of color orthophotos. Report KRL-01234, Kennedy Research Laboratories, Arlington, VA, USA.
- [82] Choi, Sunglok, Taemin Kim, and Wonpil Yu. "Performance evaluation of RANSAC family." *Journal of Computer Vision* 24.3 (1997): 271-300.
- [83] M. Mostafa, A. Moussa, N. El-Sheimy, A. Abu Sesay (2017), 30. Optical Flow Based Approach for Vision Aided Inertial Navigation Using Regression Trees, in *Proceedings of the 2017 International Technical Meeting of The Institute of Navigation*, 2017, pp. 856 - 865.
- [84] M. Mostafa, A. Moussa, N. El-Sheimy, A. Abu Sesay, May 2017. “31. Prediction of Inertial Positioning Errors Based On Gaussian Process For UAVS In GNSS Denied Environment,” *Proceedings Of The 10th International Conference On Mobile Mapping Technology (MMT)*, Cairo, Egypt.
- [85] Breiman, L., J. Friedman, R. Olshen, and C. Stone. *Classification and Regression Trees*. Boca Raton, FL: CRC Press, 1984.
- [86] A. Wojtkiewicz, J. Misiurewicz, M. Nalecz, K. Jedrzejewski, and K. Kulpa, “Two-dimensional signal processing in FMCW radars,” *Proc XX KKTOiUE*, pp. 475–480, 1997.
- [87] M. I. Skolnik, *Introduction to radar systems*, 2d ed. New York: McGraw-Hill, 1980.